

ABSTRACT

Title of Document: AN OPTICAL MICROSENSOR UTILIZING
GENETICALLY PROGRAMMED
BIORECEPTOR LAYERS FOR SELECTIVE
SENSING

Xiao Zhu Fan, Doctor of Philosophy, 2014

Directed By: Professor Reza Ghodssi, Electrical and
Computer Engineering

Protein engineering is a rich technology that holds the potential to revolutionize sensors through the creation of highly selective peptides that encode unique recognition affinities. Their robust integration with sensor platforms is very challenging. The goal of this research project is to combine expertise in micro-electro-mechanical systems (MEMS) and biological/protein engineering to develop a selective sensor platform. The key enabling technology in this work is the use of biological molecules, the *Tobacco mosaic virus* (TMV) and its derivative, *Virus-Like-Particle* (VLP), as nanoreceptor layers, in conjunction with a highly sensitive microfabricated optical disk resonator. This work will present a novel method for the integration of biological molecules assembly on MEMS devices for chemical and biological sensing applications.

Particularly in this research, TMV1Cys-TNT and TMV1Cys-VLP-FLAG bioreceptor layers have been genetically engineered to bind to an ultra-low vapor

pressure explosive, Trinitrotoluene (TNT), and to a widely used FLAG antibody, respectively. TNT vapor was introduced to TMV1Cys-TNT coated resonator and induced a 12 Hz resonant frequency shift, corresponding to a mass increase of 76.9 ng, a 300% larger shift compared to resonators without receptor layer coating. Subsequently, a microfabricated optical disk resonator decorated with TMV1Cys-VLP-FLAG was used to conduct enzyme-linked immunosorbent assay and label-free immunoassays on-a-chip and demonstrated a resonant wavelength shift of 5.95 nm and 0.79 nm, respectively. The significance of these developments lies in demonstrating the capability to use genetically programmable viruses and VLPs as platforms for the display and integration of receptor peptides within microsystems.

The work outlined here constitutes an interdisciplinary investigation on the integration capabilities of the bio-nanostructure materials with traditional microfabrication architectures. While previous works have focused on individual components of the system, this work addresses multi-component integration, including biological molecule surface assembly and fabrication utilizing both top-down and bottom-up approaches. Integrating biologically programmable material into traditional MEMS transducers enhances selectivity, sensitivity, and simplifies fabrication and testing methodologies. This research provides a new avenue for enhancing sensor platforms through the integration of biological species as the key to remedying challenges faced by conventional systems that utilize a wide range of polymers or metals for nonspecific bindings.

AN OPTICAL MICROSENSOR UTILIZING GENETICALLY PROGRAMMED
BIORECEPTOR LAYERS FOR SELECTIVE SENSING

By

Xiao Zhu Fan

Dissertation submitted to the Faculty of the Graduate School of the
University of Maryland, College Park, in partial fulfillment
of the requirements for the degree of
Doctor of Philosophy
2014

Advisory Committee:
Professor Reza Ghodssi, Chair
Professor Pamela Abshire
Professor Christopher Davis
Professor Yu Chen
Professor James Culver

© Copyright by

Xiao Zhu Fan

2014

Dedication

To my dad for his love and support throughout the years, my mom for watching over me from above, and my amazing friends for being there like family.

Acknowledgements

I would like to thank Professor Reza Ghodssi for his guidance and support throughout the course of this work and the members of the Ph.D. Dissertation committee, Professor Pamela Abshire, Professor Christopher Davis, Professor Yu Chen, and Professor James Culver for their helpful suggestions and discussions leading to the completion of this work.

A huge acknowledgement is dedicated to all my collaborators through my graduate career. Particularly, the professional and technical guidance from Professor James Culver, Dr. Nathan Siwak, Dr. Konstantinos Gerasopoulos, Mr. Adam Brown, Ms. Lindsay Naves, Mr. Faheng Zang, and Dr. Vladimir Aksyuk have been invaluable. I would like to also acknowledge the assistance I received in the fabrication and characterization from the Maryland Nanocenter personnel (Dr. Jim O'Connor, Dr. Wen-An Chou, Dr. Li-Chung Lai, Mr. Tom Loughran, Mr. John Abrahams, and Mr. Jonathan Hummel).

Last but not least, I would like to thank all the members of the MEMS Sensors and Actuators Laboratory for their indispensable discussions, suggestions, support, and camaraderie, particularly Konstantinos Gerasopoulos and Nathan Siwak for all of their advice, personal and professional.

Table of Contents

Table of Contents	iv
List of Tables	vii
List of Figures	viii
Chapter 1. Introduction	1
1.1 Motivation and Background	1
1.2 Research Accomplishments	5
1.2.1 Design and Fabrication of Whispering Gallery Mode Optical Resonators	5
1.2.2 Development of Nanostructured Bioreceptor Layers	5
1.2.3 Integration of Optical Resonator with Bioreceptor Layers	6
1.2.4 Selective Detection Utilizing a Novel Sensor Platform.....	6
1.3 Literature Review.....	7
1.3.1 Sensing Platforms	7
1.3.2 Nanostructured Receptor Layers.....	16
1.3.3 Microsensors	23
1.4 Structure of Dissertation	27
Chapter 2. Theory and Design of Whispering Gallery Mode Resonator	29
2.1 Ring Resonator Theory	29
2.1.1 Principle of Operation.....	29
2.1.2 Coupling Coefficient.....	32
2.1.3 Optical Losses.....	34
2.1.4 Bending Loss	34
2.1.5 Scattering Loss.....	36

2.2	Design and Simulation.....	37
Chapter 3.	Fabrication and Testing of Optical Resonators	47
3.1	Fabrication	47
3.1.1	Layer Structure.....	49
3.1.2	Electron Beam Lithography	50
3.1.3	Dielectric Waveguide Patterning	64
3.1.4	Chip Preparation	71
3.2	Characterization of the Optical Resonator	72
3.2.1	Testing Setup	72
3.2.2	Optical Characterization	75
Chapter 4.	Nanostructured Bioreceptor Layer	81
4.1	Tobacco mosaic virus	82
4.1.2	Synthesis of TMV-n1Cys and TMV1Cys-TNT	86
4.1.3	Purification of TMV	90
4.1.4	Analysis of TMV	91
4.1.5	Discussion	94
4.2	Virus-like-Particles	96
4.2.1	Bacterial Culture and Synthesis of TMV1Cys-VLP-FLAG	98
4.2.2	Extraction and Purification of TMV1Cys-VLP-FLAG	100
4.2.3	Discussion	103
Chapter 5.	Integration of Bioreceptors with Microfabricated Structures...	105
5.1	Self-Assembly of Bio-Nanostructures	106
5.2	Patterning of Bio-nanostructures	112
Chapter 6.	Selective Detection of Analyte	122

6.1	TNT Sensing	122
6.1.1	Experimental Setup	123
6.1.2	Results	127
6.1.3	Discussion	130
6.2	Selective Antibody Detection	132
6.2.1	Experimental Setup	133
6.2.2	Results	139
6.2.3	Discussion	147
Chapter 7.	Summary and Future Work	150
7.1	Summary of Work	150
7.2	Summary of Accomplishments	153
7.3	Future Outlook	154
7.3.1	Optimization of the Optical Resonator	155
7.3.2	Sensor Array for Multiple Analyte Detection	155
7.3.3	Lab-on-a-Chip Applications with the Integration of Microfluidics 157	
Appendix A:	Microfabrication Mask Designs	161
Appendix B:	Microfabrication Recipes	163
Appendix C:	Molecular Biology Engineering Protocols	167
Bibliography	172

List of Tables

Table 1-1. Properties of WGM Resonators (Adapted from [39]).....	14
Table 1-2. Literature Summary of WGM Resonator Sensors.....	15
Table 1-3 List of work on TNT microsensors	24
Table 2-1 Electric field integral for single vertically slotted waveguide designs.....	44
Table 2-2 Electric field integral for double vertically slotted waveguide designs	44
Table 2-3 Electric field integral for three horizontally layered waveguide design.....	44
Table 2-4 Optical resonator design parameters	45

List of Figures

Figure 1-1 Schematic diagram of a microsensor consisting of a transducer and a receptor layer.	2
Figure 1-2 Schematic of a microsensor system consisting of a microdisk resonator covered with a bio-nanostructured receptor layer for	4
Figure 1-3 Photograph of an array electrochemical platform with gold counter and working electrodes and a platinum reference electrode [61].	9
Figure 1-4 Cantilever sensor detection of (left) single E. Coli cell (600 fg) and (right) chemisorptions of thiols on gold (0.39 ag) [9].	11
Figure 1-5 A schematic showing the principle of operation of a surface plasmon resonator. By tracing the shift of the resonant frequency at the surface, sensor surface modifications can be monitored [69].	12
Figure 1-6 Diagram of a microring resonator array system showing (a) a microring resonator device, (b) beam splitter, and (c) grating coupler [71].	13
Figure 1-7 (a) AFM image of selective DNA metallization through the use of the blocking RecA protein [22], (b) TEM image of cobalt oxide M-13 bacteriophage nanowire [67].	18
Figure 1-8 Diagram showing the selective identification of peptides as the receptors for TNT and DNT molecules [121].	20
Figure 1-9 TEM images of nickel (a) and cobalt (b) coated TMV particles [45] and illustration of a digital memory device using the Pt-coated TMV and conductance switching between electrodes (c) [47].	21
Figure 1-10 (a) Defined patterns of folded DNA using hybridization techniques [53], and (b) Patterning of TMV arrays using micro-contact printing with a PDMS stamp [54].	22
Figure 2-1 Schematic of ring resonator operation showing two waveguide buses and a resonator cavity. Arrows demonstrates the direction of light propagation.	30
Figure 2-2. Spectral response of an optical channel dropping filter with a lossless ring. $L = 2\pi \times 9.55 \mu\text{m}$, $n_{\text{eff}} = 3.15$, $\tau_1 = A\tau_2 = 0.9$. On resonance, all the power is transferred to the drop port.	32

Figure 2-3. Diagram showing the coupling of two slab waveguides. The horizontal lines represent the interfaces between the core and cladding. The direction of propagation is left-to-right (or vice versa) [141].	33
Figure 2-4 Schematic of wave propagation in (a) straight waveguide and (b) bent waveguide [140].	35
Figure 2-5 Diagram showing the cross section of a silicon nitride waveguide on a silicon substrate.	39
Figure 2-6 Simulation showing the primary optical mode profile in a square (side = 1.0 μm) silicon nitride waveguide sitting on a 0.5 μm thick silicon oxide cladding.	41
Figure 2-7 Intensity of evanescent profile 100 nm outside of the dielectric waveguide for different waveguide thicknesses.	41
Figure 2-8 Simulation profile of optical modes (both TE and TM) in different waveguide geometries.	43
Figure 3-1 Diagram showing the abridged fabrication process for of an optical ring resonator.	49
Figure 3-2 Diagram showing the material layer stack	49
Figure 3-3 Monte Carlo simulation of electron scattering in a 400 nm thick PMMA resist of two different beam energies. (a) The 10kV beam showed electron scattering mostly in the PMMA layer and (b) the 20kV beam showed electron scattering mostly residing in the Si substrate beneath the PMMA layer [147].	57
Figure 3-4 PMMA A2 dose grid characterization of ring, disk, and track resonator designs (unresolved gaps were given a -100% dimension error)	58
Figure 3-5 SEM image showing a 116 nm coupling gap resolved in PMMA A2 resist using E-beam lithography	59
Figure 3-6 Diagram showing the possibility of back and secondary electron scattering in resist	60
Figure 3-7 Diagram showing the result of proximity effect. If the exposure time and energy of the beam is constant, smaller features (i.e. Coupling Gap) receive lower dosage compared to larger and nested features (i.e. Waveguide Definition)	61

Figure 3-8 Diagram showing the regions exposed to Waveguide Definition dosage (light green) and Coupling Gap Compensation dosage (dark green) for a ring resonator design	62
Figure 3-9 SEM showing physical delamination of PMMA resist due to the resist development stage.....	64
Figure 3-10 Cross sectional diagrams showing the single layer hardmask (left) and double layer hardmask (right) layer stack.....	65
Figure 3-11 SEM image showing nano-pillars in the etched trenches due to micromasking from metal nanoparticles.....	68
Figure 3-12 SEM image showing the successful pattern transfer, resolving the coupling gap and no signs of nano-pillars	69
Figure 3-13 SEM image showing a completely fabricated track-ring resonator in Si ₃ N ₄ waveguide layer	70
Figure 3-14 Block diagram showing the optical testing setup.....	73
Figure 3-15 Picture showing the testing setup on an optical table	73
Figure 3-16 A picture showing optical coupling on to and off of chip via lensed fiber secured on xyz stages.....	74
Figure 3-17 Graph showing the optical spectrum of a disk resonator at different input optical power intensities	80
Figure 4-1 (Left) Diagram showing the structural composition of a TMV and one of its coat proteins. The top and side perspective of the virus model show a helical tube viral structure. (Right) A TEM image showing TMV rods.....	83
Figure 4-2 Model diagram showing the location of the.....	84
Figure 4-3 Block diagram showing the process flow of TMV synthesis and purification	86
Figure 4-4 Picture of <i>Benthamiana</i> ready for inoculation	88
Figure 4-5 Model diagrams of (right) TMV fully expressing conjugations on each of its coat proteins and (left) TMV modulated expression of conjugations on its coat proteins due to the insertion of amber stop codon	89
Figure 4-6 TEM image of purified TMV	92

Figure 4-7 Image of gel electrophoresis showing the presence of <i>n</i> TNTbp conjugation with and without leaky stop codon	93
Figure 4-8. Image courtesy of Dr. Culver showing a Western blot of TMV1Cys-TNT with and without leaky stop codon in reference to unmodified coat proteins	94
Figure 4-9 Diagram showing the process flow of the synthesis and purification of TMV1Cys-VLP-FLAG.....	98
Figure 4-10 A TEM image, courtesy of Dr. Culver, showing the formation of VLP nanorods in bacterial cells.....	99
Figure 4-11 A TEM image, courtesy of Dr. Culver, showing VLPs after purification process.....	102
Figure 4-12 Pictures of gel electrophoresis and Western Blot results showing the successful purification of VLP- <i>n</i> 1Cys and TMV1Cys-VLP-FLAG	103
Figure 5-1 SEM images showing TMV- <i>n</i> 1Cys self-assembled on a wide range of materials and microfabricated structures	107
Figure 5-2 Diagram showing the self-assembly and metallization of TMV in three sequential steps. (Step 1) Self-assembly of TMV on substrate, (Step 2) Palladium nucleation on assembled TMV, and (Step 3) electroplating of Ni to conformally coat TMV rods.....	108
Figure 5-3 SEM images showing TMV assembly on microfabricated optical devices. TMV can be seen in sub-micron wide trenches.....	109
Figure 5-4 (Left) An AFM image showing a densely covered TMV- <i>n</i> 1Cys assembly after dehydration. (Right) A SEM image showing metallized TMV- <i>n</i> 1Cys assembled on a Au coated substrate.	110
Figure 5-5 AFM images showing the assembly of (left) TMV1Cys-TNT and (right) TMV1Cys-VLP-FLAG on Au coated substrates.....	111
Figure 5-6 SEM images showing the assembly of TMV1Cys-VLP-FLAG on an optical waveguide and a microdisk resonator.....	111
Figure 5-7 Process flow of two lift-off processes to pattern self-assembled TMV ..	113
Figure 5-8 AFM images showing the surface morphology of patterned TMV using (left) diluted developer and (right) acetone	116

Figure 5-9 AFM images showing the boundary of the patterned TMV. (a, b) shows the amplitude and phase of the boundary patterned by diluted developer showing no obvious structure instability. (c, d) shows the amplitude and phase of the boundary patterned by acetone showing some possible denaturation	118
Figure 5-10 SEM images showing the boundary of TMV patterned using (a, b) diluted developer and (c, d) acetone. The TMV- <i>n</i> 1Cys were metallized post patterning, demonstrating its engineered functionality is conserved through the patterning process.	119
Figure 5-11 SEM image showing the patterning of TMV- <i>n</i> 1Cys on microfabricated Si waveguide	120
Figure 6-1 (a) A picture showing an example of a QCM used. (b) A Diagram showing the shear wave induced in a QCM generated by an external AC signal	123
Figure 6-2 . AFM images showing the surface morphology of (a) uncoated, (b) <i>I</i> _{cys} -TMV, and (c) <i>TNT</i> -TMV coated QCM surfaces.	128
Figure 6-3 Graph showing the mass shift due to TMV virus assembly (blue) and TNT exposure (red) of uncoated, TMV- <i>n</i> 1Cys, and TMV1Cys-TNT coating of QCM surfaces	129
Figure 6-4 Graph showing the resonant frequency shift due to TNT vapor introduction of three QCMs with uncoated (blue), TMV- <i>n</i> 1Cys (Orange), and TMV1Cys-TNT (grey) coating of QCM surfaces	130
Figure 6-5 CAD diagram showing the molecular structure of (a) a TMV1Cys-VLP-FLAG showing both the cysteine and FLAG antigen on the outer surface of the VLP nanorod and (b) an representative antibody with two antigen binding sites.....	132
Figure 6-6 Process flow showing the standard procedure of a sandwich ELISA protocol	136
Figure 6-7 Diagram showing the principle of ELISA-on-a-chip using self-assembly TMV1Cys-VLP-FLAG.....	137
Figure 6-8 SEM images showing the assembly of TMV1Cys-VLP-FLAG on a fully microfabricated disk resonator.....	140
Figure 6-9 Optical frequency spectra showing the shift in resonant frequency due to the assembly of TMV1Cys-VLP-FLAG.....	141

Figure 6-10 Resonant frequency shift due to the assembly of VLPs, followed by conducting ELISA-on-a-Chip	142
Figure 6-11 Resonant frequency shift induced by the binding of the primary and secondary antibodies	144
Figure 6-12 (a) Picture showing the color intensity of ELISA conducted on gold coated chips under all wet conditions versus rinsed and dried conditions. (b) Color intensity analysis of the two set of ELISA chips showing an overall less dense color intensity for the rinsed and dried samples	146
Figure 7-1 A CAD drawing showing an array of three sensors that can be monitored simultaneously for the selective detection of different analytes. Optoelectronics permitting, interrogation instruments can be integrated on-chip for remote sensing applications.	156
Figure 7-2 Diagrams showing (left) top view and (right) cross-section of an optical resonator array platform integrated with a microfluidic channel system	157

Chapter 1. Introduction

1.1 Motivation and Background

Identification of the presence or the concentration of an analyte is important for a wide variety of sensing applications. The primary goals and challenges shared by all sensor systems are to achieve high sensitivity and selectivity. Recently, considerable research efforts have been focused toward developing novel sensor technologies to replace a number of traditional sensor techniques such as X-ray, γ -ray, gas chromatography, Raman spectroscopy, and nuclear quadrupole resonance. A drawback to these expensive instruments is their difficulty to be miniaturized. There is a strong motivation and incentive to develop small, low-powered, easy to use microsystems that are highly sensitive and selective to replace these conventional macro-scale sensors for the identification of chemical or biological compounds.

A number of miniaturized sensors, such as surface acoustic wave sensors [1], surface plasmon resonance [2-4], quartz crystal microbalances [5], and a variety of microelectro-mechanical systems (MEMS) sensors [6-10], have been developed. They provide high reliability and sensitivity in addition to the distinct advantages of small size, low power, and easy integration with control electronics [11-14]. The primary drawback of these devices is their lack of selectivity -- the ability to recognize a specific target -- because of nonspecific sorption or binding. The selectivity can be improved

by addition of a receptor layer that has a high affinity towards a specific analyte. The integration of a receptor layer is often not straightforward due to the compatibility needed between the transduction device and the receptor layer on multiple levels of integration and functionality (Figure 1-1). This includes the compatibility of the deposition process of the receptor layer, the operation of the transducer with a supplementary coating, and the long term stability and reliability of the system.

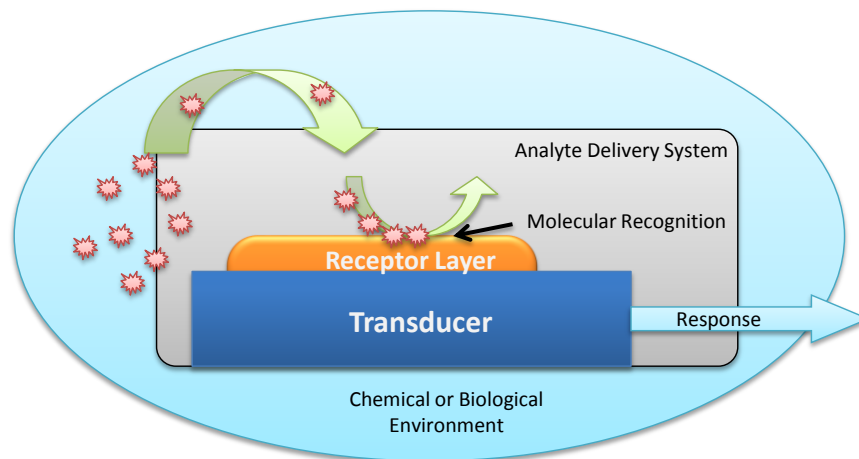


Figure 1-1 Schematic diagram of a microsensor consisting of a transducer and a receptor layer.

The objective of this work is to develop a sensor platform system that would overcome these limitations by taking advantage of the high sensitivity demonstrated in optical sensors and the high selectivity that biological species can provide.

MEMS technology is ideal in terms of realizing a highly sensitive microtransducer. MEMS is a multi-disciplinary and diverse field that not only focuses on device development but also systems engineering and integration, relying particularly on microfabrication and the integration of nano-and micro- technologies. This makes MEMS technology an excellent choice for the development of these future sensor systems, as the importance of portability and mass production become paramount. Optoelectronics, which takes advantage of MEMS technology, deal with light generation, manipulation, and detection using microstructures, can provide high sensitivity due to the properties of wave propagation coupled with the high resolution instrumentation provided by the mature field of optical communications [4, 15, 16]. As a result, an optical microresonator was selected as the transduction mechanism for this sensor system.

Due to the inherent properties of biological molecules (e.g. nanostructured template, self-assembly, genetic programmability and spatial patterning) they represent a very versatile approach for the realization of selective receptor layers for microsensor systems. Through biological evolution and/or genetic engineering, biological species have produced highly selective receptors to target chemical and biological compounds with proven high binding recognition capabilities [17-21]. Already sensor systems that have taken advantage of biologically active components, such as enzymes, antibodies, and nucleic acids, have help transform bio-detection, genome/proteome analysis, and

drug discovery [22]. *It is only logical to take advantage of these structures by incorporating these biomolecules in microsensor systems to enhance the selectivity of existing receptor layers and take advantages of their programmability to realize a versatile platform for a multi-analyte sensor.* We have selected a versatile bio-nanostructured receptor layer, capable of expressing a high density of peptide binding probes, to be integrated with the optical microsensor for the selective detection of various analytes, see Figure 1-2.

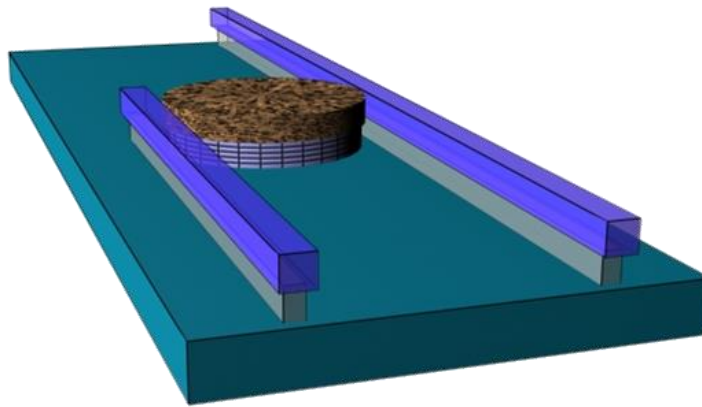


Figure 1-2 Schematic of a microsensor system consisting of a microdisk resonator covered with a bio-nanostructured receptor layer for

1.2 Research Accomplishments

1.2.1 *Design and Fabrication of Whispering Gallery Mode Optical Resonators*

A silicon-based microdisk resonator was developed as a refractive index (RI) sensor platform due to its high sensitivity to changes in surface properties. The microdisk resonator was first designed and modeled using MATLAB and COMSOL software packages. Next, a fabrication process flow was developed, characterized, and implemented. Lastly, the optical properties of the resonators were measured and analyzed. Although the microdisk resonator is a mature technology, microfabrication with such a high resolution and low fabrication tolerance can be difficult to achieve in an academic setting. Unit processes have been developed that enable fabrication of disk resonators with small widths, high aspect ratios, low losses and high quality factors.

1.2.2 *Development of Nanostructured Bioreceptor Layers*

Bioreceptor layers based on viruses were developed to express high chemical affinity for target molecules on the outer surface of their nanostructures. Two bio-nanostructures were developed that were based on: (1) *Tobacco mosaic virus* (TMV), and (2) *Virus-like-particles* (VLP), formed by self-assembly of TMV coat proteins in bacterial cells. The programmable expression of functionality was realized by

genetically mutating their coat proteins with a high affinity peptide displayed on their outer surface. Their synthesis and purification protocols were developed and executed.

1.2.3 Integration of Optical Resonator with Bioreceptor Layers

The challenge of benefitting from the advantages offered by biological components and microfabricated sensing platforms is the compatibility across disciplines. In order to successfully integrate the two technology platform, three key areas of interest were investigated: (1) virus affinity for material surfaces, (2) virus compatibility with selected MEMS fabrication processes, and (3) the induced change in refractive index due to virus assembly. Resulting from these investigations, TMV assembly and patterning processes were developed.

1.2.4 Selective Detection Utilizing a Novel Sensor Platform

The completion of the previous aspects of the research led to the selective detection of targeted analytes, an explosive vapor and an antibody. Genetically engineered TMVs and VLPs were utilized as selective receptors for chemical and biological species. Trinitrotoluene (TNT) vapor sensing was conducted using TMV-*n*1Cys-*c*TNT on quartz crystal microbalances and showed an increase of 300% in mass compared to the uncoated control. Antibody FLAG detection was conducted using TMV1Cys-VLP-FLAG assembled on the microfabricated optical microdisk resonators showing sensitivity low enough to detect antibody label-free. The functional

demonstration and the versatility of these genetically engineered bioreceptor layers were the primary focus of the system's development.

1.3 Literature Review

1.3.1 Sensing Platforms

Existing macro-scale sensors may use capacitive [23], resistive [24], bulk resonance [25], or optical methods [9] to transduce a chemical or biological phenomenon into a useable signal [25]. The performance of these sensors is often limited by large device sizes, high power consumption, slow response time, or bulk supporting equipment which can prevent large-scale integration and portability. Capacitive, resistive, and bulk resonator sensors experience significant drawbacks when considering crosstalk in large scale arrays. Many examples of macro-scale optical sensors require large external equipment such as lasers, spectrum analyzers, and photodetectors [26-30] which can limit sensor functionality and deployment options.

In contrast to traditional sensor platforms, MEMS sensors overcome many of those challenges due to their small size, high sensitivity, and low cost in mass production. MEMS resonator sensors were first developed in the 1960's by Nathanson [31] and Howe [32], who demonstrated vapor sensing using resonant gate transistors. Since then, electrical sensors (FET [33], capacitive [23], impedance, electrochemical [34-36]), mechanical resonators sensors (cantilevers [7-9, 12], doubly-clammed beams

[37-40], membranes[41-43]), and optical sensors (optical resonators [4, 16, 44-50], waveguides [51-53], fluorescents [54-57] have all been studied, each with their respective advantages and disadvantages.

Electrical sensors range from simple passive devices to more complicated active components. Typical two terminal passive components monitor the change in conductance, dielectric constant, and/or displacement caused by the addition or subtraction of target molecules by measuring a change in resistance [24], capacitance [23], or inductance [58]. Three terminal active devices include gate-controlled field effect transistors [33, 59, 60] and electrochemical cells [34-36]. Both of these platforms take advantage of the change in mobility of ions in a medium based on the addition/subtraction of molecules at the interface with the air. Electrical sensors are generally highly sensitive and CMOS compatible, often arrayed and integrated into various system architectures. Figure 1-3 is a photograph of a 3 x 3 array electrochemical sensor used for DNA hybridization sensing [61]. However, electrical sensors are susceptible to cross-talk and parasitic effects, which decreases the signal to noise ratio (SNR) and decreases the sensor's sensitivity. Additionally, aqueous solutions may be incompatible with some designs due to the conductivity of the medium.

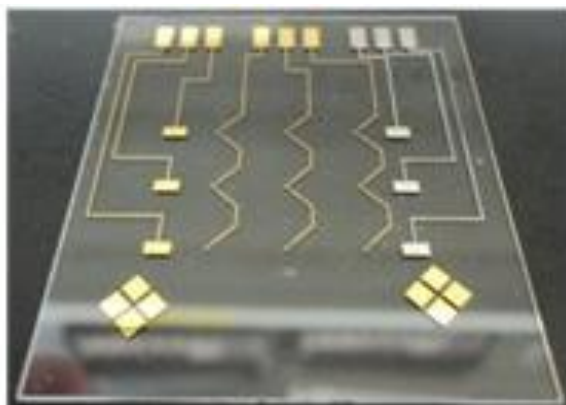


Figure 1-3 Photograph of an array electrochemical platform with gold counter and working electrodes and a platinum reference electrode [61].

MEMS mechanical microresonators provide promising sensor solutions that are scalable, low power, and portable. The ability to mass produce and to accurately control and tailor device mechanical properties of such sensors provides a distinct advantage over some non-mechanical approaches. Various analytes can be measured with identical mechanical devices, reducing complexity of device design. Additionally, many have the advantage of performing detection with label-free methods [9, 11] and can be microfabricated into arrays to perform multiple sensing operations simultaneously.

Mechanical resonators include cantilevers (Figure 1-4), doubly clamped beams, and membranes. These resonator sensors generally operate in two modes, statically and dynamically [9]. The static operating method measures the induced stress/strain of the

mechanical platform caused by the attachment of analyte. The stress/strain is measured primarily by platform displacement [10], voltage potential shift [62], or resistance change [63]. Dynamic operating method measures the induced change in resonant frequency of the resonator due to the added mass (a microbalance). Its mechanical resonant frequency and its quality factor are dependent on the geometry and design of the sensor and the testing environment. Dynamic measurement methods introduce additional complexity due the requirement of actuation, which is generally performed electrostatically [7], piezoelectrically [64], or magnetically [65]. Due to the high resolution readout methods for both methods of operation, mechanical resonators possess very high sensitivity [14]. Their main drawback is fabrication compatibility. On-chip readout methods are not trivial and the necessary external instrumentation limits the sensor to a laboratory environment. Dynamic MEMS devices face an additional restriction of energy storage on the sensor chip to prevent possible environmental or analyte reaction to the instrumentation energy, i.e. ignition of volatile organic compounds (VOC) explosives due to possible discharge [66].

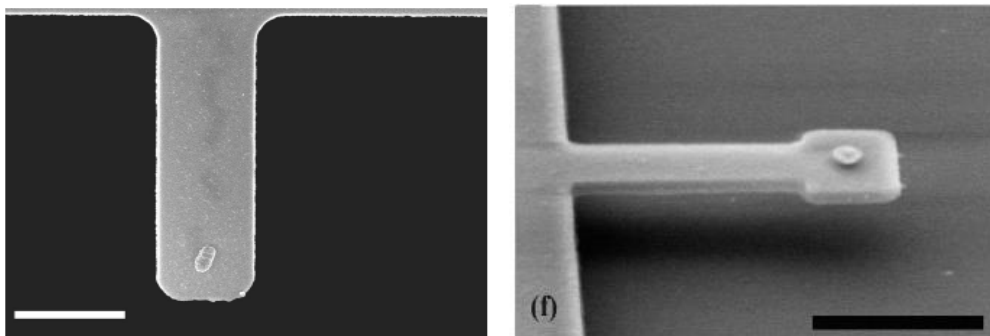


Figure 1-4 Cantilever sensor detection of (left) single E. Coli cell (600 fg) and (right) chemisorptions of thiols on gold (0.39 ag) [9]

Optical sensors are versatile and sensitive, and they are used in a wide range of applications. Light generation, light absorption, wavelength and phase shifts are just a few optical properties that are monitored for sensing applications. One branch of optical sensors is optical refractive index (RI) sensors, which are widely studied for numerous applications. RI devices utilize wave-analyte interaction that is measurable as a change in RI, providing high sensitivity, electrical parasitic and mechanical vibration immunity, with real-time output and no florescent labeling [67]. Examples of RI sensors include surface plasmon resonance (SPR) [3, 4] and photonic crystal structures [68], long-period fiber gratings (LPFG) [50], and various forms of optical filters including whispering gallery resonators.

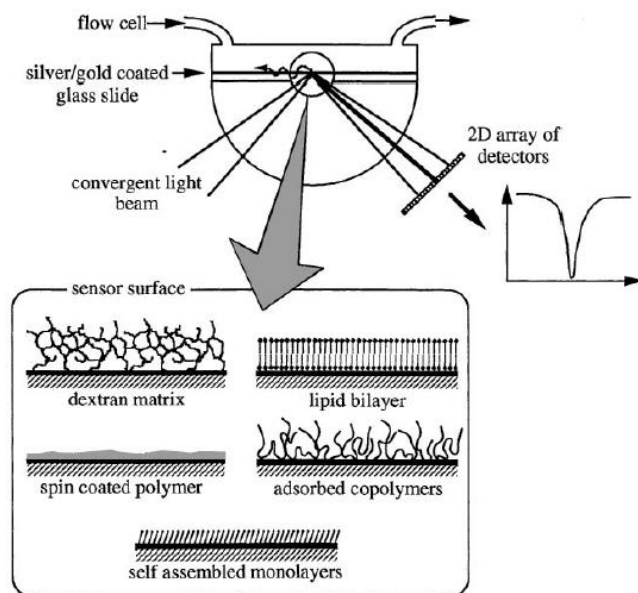


Figure 1-5 A schematic showing the principle of operation of a surface plasmon resonator. By tracing the shift of the resonant frequency at the surface, sensor surface modifications can be monitored [69].

A whispering gallery resonator can sustain Whispering Gallery Modes (WGM) electromagnetic (EM) modes [70]. The EM waves are totally internally reflected and focused by a spherical surface. Due to minimal reflection losses these modes can reach very high Q factors. Applications such as all optical switching, electro-optical switching, wavelength conversion, and filtering have been demonstrated using whispering gallery resonators. It is also a great candidate as a sensor transducer due to its high Q, enabling easy spectrum shift detection, and chemical responsiveness due to

longer wave-analyte interaction from the repeated wave circulation in the ring resonator. Furthermore, microring resonator sensors are compatible with both vapor and liquid sensing, since air and aqueous solutions are both appropriate cladding materials due to their low refractive indexes.

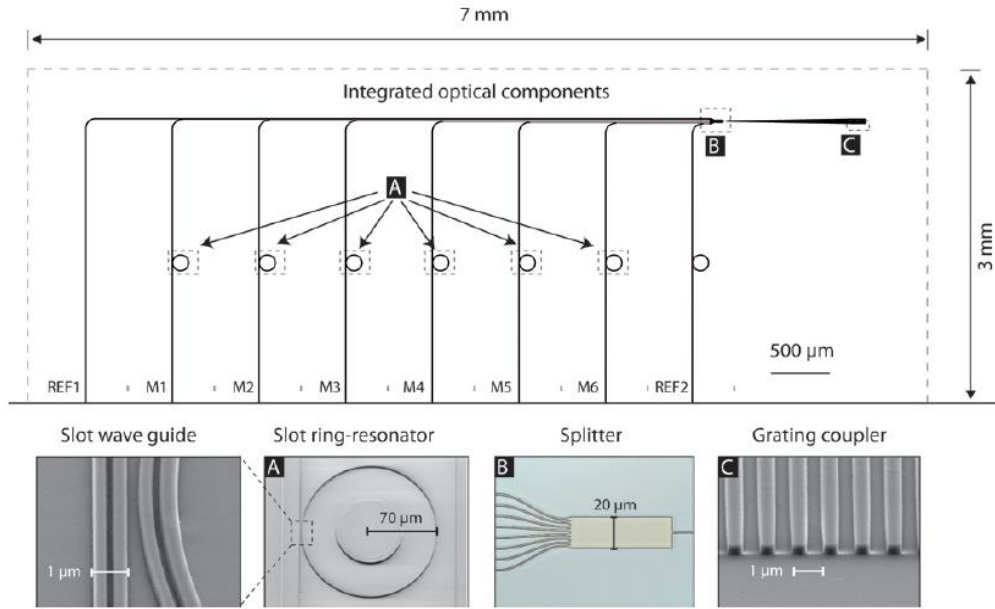
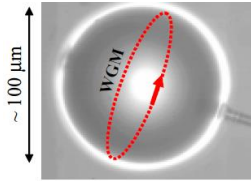
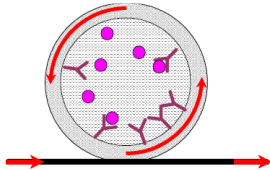
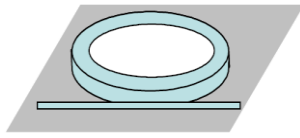


Figure 1-6 Diagram of a microring resonator array system showing (a) a microring resonator device, (b) beam splitter, and (c) grating coupler [71]

WGM propagation in a spherical resonator exhibits the highest Q in the WGM resonator branch, often surpassing 5 million. Although the high Q provides the highest sensitivity, spherical resonators are incompatible with system integration and are impractical for sensing applications due to their difficulty of fabrication [49]. WGM

are also observed in liquid core optical ring resonators (LCORR) where WGM propagates around the wall of a tube. LCORR has the advantage of high Q (1 million has been obtained). However, LCORR requires custom fabrication of the tubes and difficult serial integration with on-chip waveguide, limiting system integration and mass production of LCORR sensors [15, 16, 72-74]. WGM are also present in planar microring resonators (which will be referred as just ring resonators for the remainder of this proposal) which can be fabricated utilizing traditional MEMS fabrication technology [47, 75-77]. The microring resonators exhibit a slightly decreased Q factor (20,000) but the slight decrease in sensitivity is offset by easy on-chip system integration and array multiplexing for multi-sensor applications. Table 1-1 below summarizes the resonator properties and realization challenges of each WGM resonators.

Table 1-1. Properties of WGM Resonators (Adapted from [15])

			
	Microsphere	LCORR	Ring Resonator
Sensitivity	26 nm/RIU	>30 nm/RIU	70 nm/RIU (De Vos)
Q factor (in water)	5×10^6	1×10^6	2×10^4
Bulk Refractive index change detection	3×10^{-7} RIU	1×10^{-6} RIU	1×10^{-7} RIU

limit			
Protein detection limit (pg/mm²)	1-10	10	250
Photonics integration	Poor	Good	Good
Microfluidics integration	Poor	Good	Average
Mass-production	Poor	Poor	Good
Multiplexed detection	Poor	Average	Good

Microring resonators have been developed in different materials for a wide range of applications. The table below summarizes a list WGM sensor research in recent years.

Table 1-2. Literature Summary of WGM Resonator Sensors

Authors	Transducer	Sensing	Material	Liquid/Gas	Detection Limit
Hanumegowda, et al [49]	Sphere Resonator	Mercuric Ion	Silica	Liquid	50ppb
X. Fan, et al [13] I. White, et al [74] H. Zhu, et al [72]	LCORR	Ethanol, Antibody, M13 phage, bovine serum albumin (BSA), cell	Glass Capillary	Liquid	10pg/mm ² 10pM 1.8x10 ⁻⁵ RIU
Pang, et al [48]	Ring Resonator	Ethanol	Sol-gel	Gas	N/A
Y. Sun, et al [67]	Ring Resonator	Displacement	GaAs	N/A	10 ⁻⁴ Å ⁻¹
Ksendov, et al [44, 45]	Ring Resonator	IPA, Protein, Avidin	Polymer (Ethyl Cellulose), SiN, SiO ₂	Gas, Liquid	50ppm, 0.1 nM
Chao, et al [78]	Ring Resonator	Glucose, Straptavidin	Polymer (polystyrene)	Liquid	250 pg/mm ² 10 ⁻⁷ RIU
De Vos, et al [79] Yalçın, et al [80]	Ring Resonator	Avidin,	Silicon (SOI)	Liquid	1fg 10 ⁻⁵ RIU

Passaro, et al [81]	Ring Resonator	Ammonia	Silicon (SOI)	Gas	8×10^{-5} RIU 4 ‰
------------------------	-------------------	---------	---------------	-----	----------------------------------

The sensors listed all exhibit great sensitivity; however, the majority of work found in literature lacks a promising selective receptor layer. While many platforms are expected to be capable of being functionalized using established immobilization protocols for antibodies, nucleic acids, receptors and artificial sensing layers [82], rarely has there been demonstrated success beyond the few reports listed above.

1.3.2 Nanostructured Receptor Layers

1.3.2.1 Inorganic Material

A wide variety of methodologies have been employed in the synthesis of nanostructured materials such as nanotubes and nanowires, nanoparticles and quantum dots. Some of the most common processes used for the bulk fabrication of zero and one-dimensional nanomaterials involve vapor-liquid-solid reactions through the combination of catalytic particles on a substrate and chemical vapor deposition or epitaxial methods [83-87]. Other less expensive techniques such as hydrothermal synthesis [88, 89], thermal evaporation [90], sol-gel processes [91, 92] and electrodeposition [93] have been reported. In addition to bulk synthesis, hierarchical structures have been created through the use of porous templates [94, 95]. While all of these techniques demonstrate the significant progress in the field, they often have to balance the trade-off between good control over structural properties, variability of

available materials, and aspect ratios on one hand and low cost, external equipment and process compatibility with remaining fabrication steps (e.g. substrates and temperature) on the other.

1.3.2.2 Organic Materials

Biotemplating refers to synthetic routes that utilize biological building blocks to guide the assembly of inorganic materials. Some of the characteristic attributes of this approach compared to traditional methods include the structural versatility of biological molecules, their self-assembly properties, the existence of various functional groups that catalyze particle growth and the ability to tune their structure through genetic modifications, all combined with the low cost involved in the manufacturing process[96, 97]. DNA has been one of the most investigated templates due its controllable length and aspect ratio as well as its phosphate backbone and aromatic bases which create sites for nucleation through electroless plating reactions [98]. Several kinds of metal and polymer nanowires based on DNA strands have been produced [99-103] while more sophisticated approaches for selective mineralization of parts of the chain demonstrate the feasibility of using such particles for molecular-type lithography [104] (Figure 1-7 (a)). Other biological molecules including bacteria [105-107] and proteins [108] have also show selective affinity to non-organic molecules and have been used to fabricate fibers, nanoparticles and quantum dots. These synthetic pathways show diversity and great promise to replace semiconductor approaches for

nanoscale devices; however, they often lack coating uniformity, reproducibility and need special surface treatment prior to metallization and assembly.

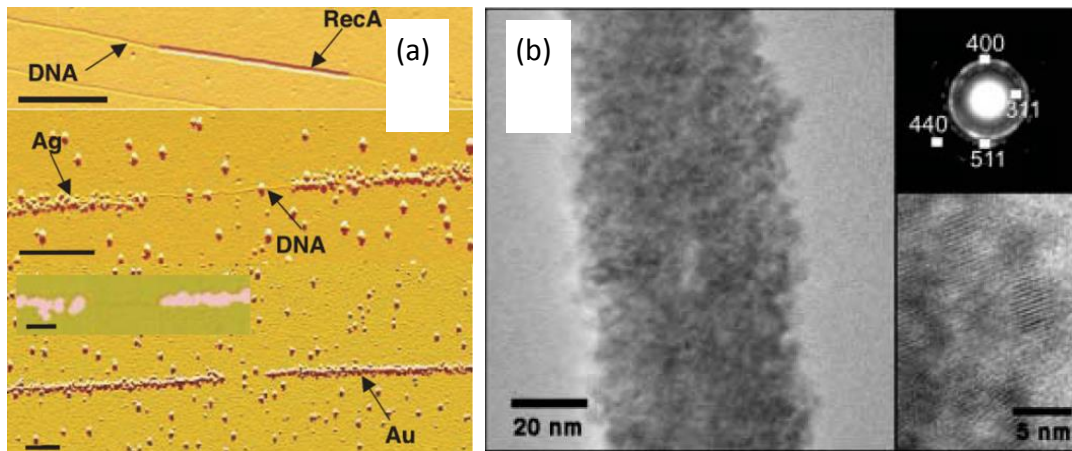


Figure 1-7 (a) AFM image of selective DNA metallization through the use of the blocking RecA protein [22], (b) TEM image of cobalt oxide M-13 bacteriophage nanowire [67].

Another interesting and popular choice of high affinity biological receptor molecules are peptides. Peptides are short chains of amino acid monomers that chained together by covalent chemical bonds, called peptide bonds. Distinguished from proteins by size, peptides generally consist of 50 amino acids or less and referred to as *N*-mer for *N* number of amino acids. There is the possibility to synthesize peptides with different combinatorial sequences of amino acids. This diversity in chemistry and structural geometry can lead to molecular recognition through multivalent and cooperative binding based on relatively weak hydrogen bonding or van der Waals

forces. The immune system is an example of such molecular recognition which utilizes specific protein-based receptors to target foreign antigens. The difficulty of utilizing sequence-specific peptides for sensing applications is to identify a particular sequence, N -mer amino acid sequence, which provides the strongest multivalent binding among 20^N possible sequences. As a result, a laboratory technique called the phage display to study the interactions between peptide and analyte. Phage display inserts a gene fragment into a gene responsible for the surface protein of a bacteriophage. This genetic mutation allows for the surface coating of the phage to display the new amino acid sequence and can be used to be tested for binding affinities. Phage display has been used extensively as a tool for drug discoveries, finding new peptides and proteins that target proteins [109-111], genes [112], and antibodies [113-115]. Phage display have also been use to explore the affinity of peptides to semiconductors [116, 117] and metals [118-120]. Moreover, sequence-specific peptides have been discovered to selectively binding to volatile organic compounds (VOCs), including explosive vapors such as TNT and DNT. Jaworski et al. [121], utilized this evolutionary screening process to identify two 12-amino acid long peptides (WHWQRPLMPVSI and HPNFSKYILHQR) that were specific to TNT and DNT. Through mutational analysis, they demonstrated that multivalent binding is the key to selectivity of the TNT binding motif.

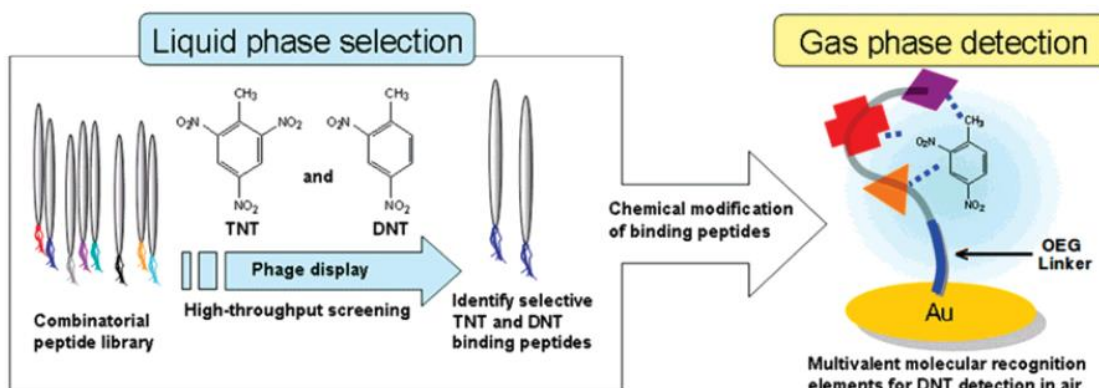


Figure 1-8 Diagram showing the selective identification of peptides as the receptors for TNT and DNT molecules [121]

1.3.2.3 Virus-based Templates and the *Tobacco mosaic virus*

Another category of biological nanostructures that offers unique opportunities for biotemplated fabrication are plant and bacteria virus particles consisting of macromolecular assemblies of nucleic acid packaged by many copies of coat proteins. In addition to their surface-exposed functional groups, self-assembly and tunability, these molecules display some unique advantages as they show exceptional stability in a wide range of temperatures and pH values; they can even withstand treatment in organic solvent-water mixtures [122]. Representative examples of biotemplated viral engineering have been achieved with the M-13 bacteriophage virus (Figure 1-8) which has been genetically modified through phage-display techniques to include specific peptides for inorganic material binding and nanoparticle fabrication [123-125].

Among the available plant viruses, simple plus-strand RNA viruses have been most widely used as metallization templates (Figure 1-9). Patterning has been reported for several of these viruses [126, 127], however, *Tobacco mosaic virus* (TMV) is the most extensively studied filamentous plant structure for nanoscale applications.

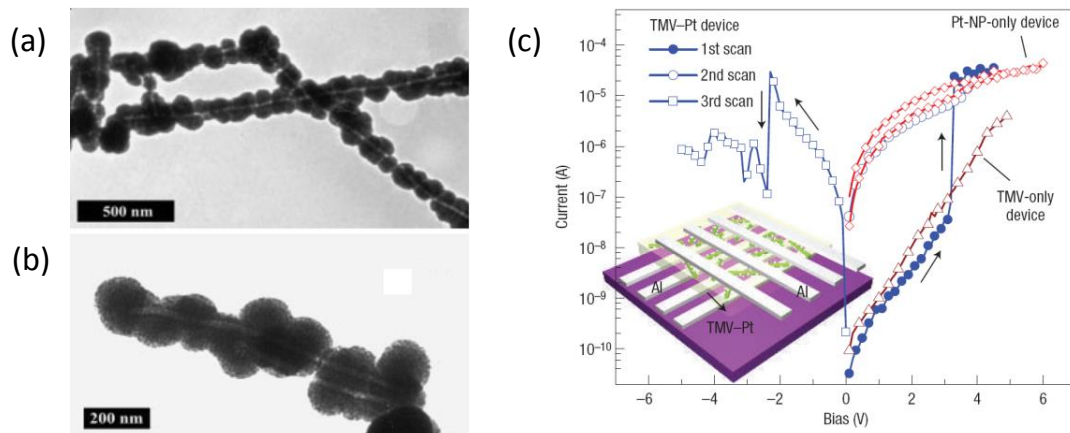


Figure 1-9 TEM images of nickel (a) and cobalt (b) coated TMV particles [45] and illustration of a digital memory device using the Pt-coated TMV and conductance switching between electrodes (c) [47].

Patterning of Nano-scale Materials

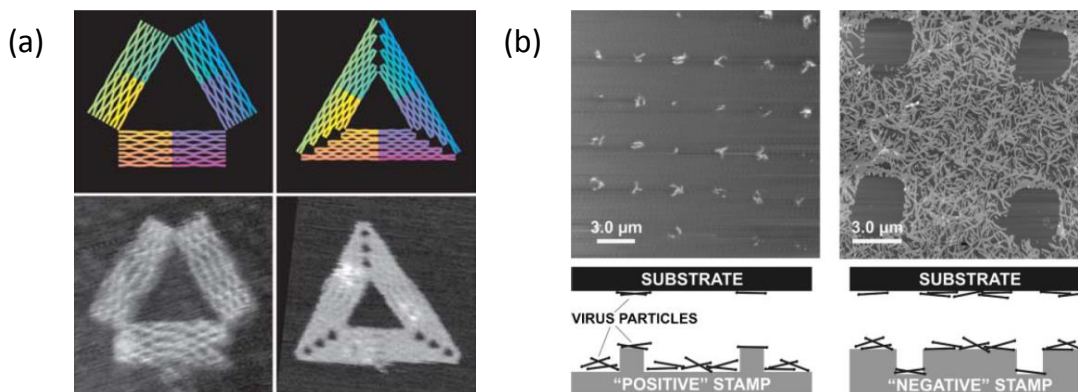


Figure 1-10 (a) Defined patterns of folded DNA using hybridization techniques [53], and (b) Patterning of TMV arrays using micro-contact printing with a PDMS stamp [54].

Conventional methodologies for arranging nanowires in nano-scale devices involve the use of electron beam lithography capable of achieving features on the order of tens of nanometers. In order to complement this technology, other approaches associated with less expensive instrumentation have been proposed [128]. Scanning probe [129] and dip-pen [130] nanolithography techniques utilize AFM tips operated under different modes to transfer molecules of interest to a substrate through capillary and other interactions. Selective placement of DNA nanowires onto patterned electrodes can be achieved through self-assembly and functionalization with specific chemicals [131], while nucleic-acid hybridization has been shown to create intricate patterns of DNA in a robust, “one-pot” reaction [132] (Figure 1-10)

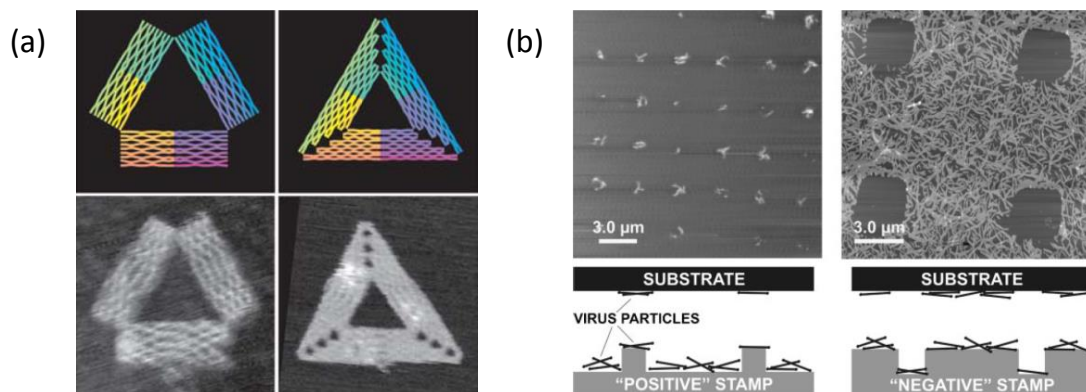


Figure 1-10 (a) Viruses and proteins can also be arranged on substrates through micro-contact printing [133, 134]. This technique uses an elastomeric structure fabricated through soft-lithography which is then wetted with the functional material and stamped on the target substrate Figure 1-10 (b)). Notwithstanding the individual advantages of these methods, they cannot always be scaled up (or down) at the wafer level or show compatibility with batch fabrication, attributes very important in high-throughput manufacturing. Consequently, novel schemes that combine self-assembly, templated synthesis and lithography [135, 136] are expected to have a tremendous impact on next-generation technological applications.

1.3.3 Microsensors

Systems integration of transduction platforms with nanostructured receptor layers has a wide array of sensing applications. The motivation behind microsensor systems ranges from homeland security to personal care to health care and

pharmaceutical applications. While the specifications of the sensor platform vary from application to application, the sensitivity and the selectivity is a common denominator for all. The flexibility and the programmability to detect different analytes are unique to this system. This dissertation demonstrates the detection of two targeted analytes using a programmable receptor template: (1) 2,4,6-trinitrotoluene (TNT), $C_6H_2(NO_2)_3CH_3$, chemical vapor signature, and (2) FLAG antibody biomolecule. Some of the most notable TNT microsensors developments are listed below, in Table 1-3, providing an overview of the current state of the art.

Table 1-3 List of work on TNT microsensors

	Transducer Mechanism	Receptor Layer	Sensitivity	Phase	Reference
1	Cantilever	Polymer	300 ppt	Vapor	Pinnaduwaage, 2004
2	Cantilever	SAM 4-mercaptobenzoic acid	ppb	Vapor	Seenva V
3	Cantilever	SAM 6-mercaptonicotinic acid	20-30 ppt	Vapor	Zuo 2006
4	Electrochemistry	Molecularly imprinted polymer	1.5×10^{-9} mol/L	Solution	Alizadeh 2010
5	Electrochemistry	N/A	7 ppb	Vapor	Krausa 1999
6	Electrochemistry	DNA-functionalized SWCNT modified electrodes	0.5 μ g/L	Solution	Liu 2009
7	Electrochemistry	maltose protein binding nitroreductase fusion modified with an	2 μ M	Solution	Naal 2002

			electropolymerized film of N-(3-pyrrol- 1-ylpropyl)-4,4- bipyridine			
8	Impedance/resistance		GaN nanowire/TiO ₂	0.5 ppb	Vapor	Aluri 2011
9	Microcapacitive membrane sensor		Peptide Probe	N/A	Vapor	Lim
10	Microring resonator sensor		Triphenylene Ketals based material N/A	1 ppb	Vapor	Orghici/ 2010
11	Photoluminescence		Mn ²⁺	1 nM	Solution	Tu 2008
12	Planar integrated optical waveguide (IOW) spectrometry		Organically modified sol-gel polymers	5 ppb	Vapor	Walker 2007
13	Quartz Crystal Microbalance		Polymeric matrix and peptide	N/A	solution	Cerruti 2009
14	Surface Acoustic Wave		Anti-TNT antibodies	N/A	Solution	Lee
15	Si photonic vertical microcavity		Conjugated polymers (MEH-PPV)	N/A	Vapor	Levitsky 2007
16	Surface Plasmon Resonance		a) SAM Oligo (thylene glycol) b) Antibody	a) 80 ppt b) 50 ppt	Solution	Mizuta 2008
17	Surface Plasmon Resonance		Polyclonal antibodies	6 ppt	Solution	Shankaran, 2006
18	SWNT-FET		PDA-based lipid membranes coupled with biologically inspired TNT peptide receptors	1 fM	Solution	Kim et al 2011
19	SWNT-FET		Peptide (P1ASP`C)	1 ppt	Solution	Kuang 2010

The challenge facing TNT transducer platforms is the TNT molecules' extremely low vapor pressure at room temperature, resulting in typical air

concentrations of 6 ppb. This vapor level is often below the sensitivity of the sensor platform operating in air, leading to detection of TNT molecules in solution phase. Pre-concentrator and amplification methods have been used to enhance the minimum detectable levels of TNT at the microscale. Furthermore, high selectivity of the receptor layers to TNT is difficult to achieve. While selectivity to TNT molecules is often claimed, the affinity of the receptor layers is actually towards all nitroaromatic compounds, preventing the distinction between compounds such as nitrobenzene, dinitrotoluene, and TNT.

The comprehensive list of the plethora of micro-biosensors would be too long to be included here. In-depth review articles that survey the recent development of antibody detection and monitoring as well as miniaturizing enzyme-linked immunosorbent assay (ELISA) on-a-chip are readily available [137-139]. The challenge to realize these sensors is not found in a need for a highly selectively receptor layer because antibodies naturally have a high affinity towards antigens. The challenge lies in the integration of the sensitive biomolecule with microfabricated transducer platforms without limiting the platforms' sensitivity. The integration of the receptor layer with the microstructured devices is usually not straightforward, as the bioreceptor layer is often not compatible with the harsh chemical environments, extreme pH levels, temperatures and physical strains often required by microfabrication. As a result, the

potential advantage provided by bioreceptor layers is dependent on their ability to be successfully integrated with microtransducer platforms.

In this dissertation, some of these issues will be addressed by utilizing a highly robust virus-based receptor that has high binding site density, can be self-assembled, and is compatible with microfabrication techniques. In addition, the versatility provided by the receptor layer allows for the nanostructured virus to be used as a receptor template for a wide range of sensing applications. This novel receptor layer will be demonstrated to be capable of detecting TNT in vapor phase and antibody in liquid solution.

1.4 Structure of Dissertation

The following text is divided into seven chapters. Chapter 1 gave an overview of this project, including its motivation, background, and a summary of research accomplishments. Chapter 2 describes the theory and design of an optical resonator. The design will dictate the fabrication process flow introduced in the following chapter. Chapter 3 will cover the in-depth characterization of the fabrication process. The optimized fabrication recipes are listed in the Appendix B. Also included in this chapter are the description of the testing setup and the characterization of the microfabricated optical resonator. Chapter 4 will transition to the second component of the microsensor system and introduce the two nanostructure bioreceptor layers used for the selective

detection of analytes. Chapter 5 is dedicated to the discussion of the integration of the bioreceptor layers with the optical resonator and Chapter 6 will detail the selective detection of analytes and a general discussion of the microsensor system. The final chapter, Chapter 7, gives a summary of the research presented. Future work is described, followed by a brief analysis of the potential impact of this work and the final conclusion.

Chapter 2. Theory and Design of Whispering Gallery Mode Resonator

2.1 Ring Resonator Theory

2.1.1 Principle of Operation

Propagation of an optical wave through a waveguide can be affected by the nearby environmental changes, resulting in a modulation in propagation characteristics. A whispering gallery mode resonator is one of many optical sensors used to detect target molecules due to its high sensitivity, simple integration with optoelectronics, and multiplexing capabilities. A ring resonator, one example of a whispering gallery mode resonator used to describe its principle of operation, is composed of two sets of bus waveguides and a ring resonator cavity, as shown in Figure 2-1.

The input optical signal is coupled on-chip via the input port and travels towards the resonator coupling cavity. There is a relative $\pi/2$ phase shift between the input waveguide and the ring resonator. Similarly, the signals coupled to the through port and the drop ports both exhibit a phase shift of π . As a result, with correct coupling coefficient design, the field coupled to the through port on resonance would completely extinguish the resonant wavelength, and all the power would be coupled to the drop port.

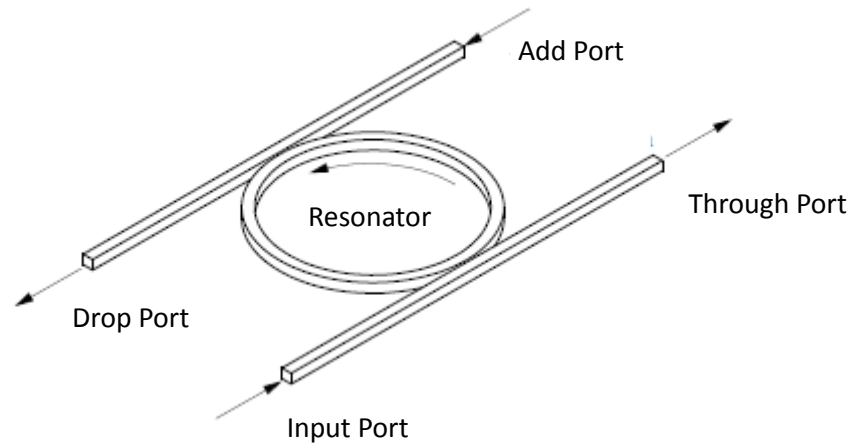


Figure 2-1 Schematic of ring resonator operation showing two waveguide buses and a resonator cavity. Arrows demonstrates the direction of light propagation.

Inside the microring cavity, whispering gallery modes are excited due to the total internal reflection of the light along the curved boundary surface. Optical power gets evanescently coupled to the ring cavity from an input bus waveguide. The intensity of a specific wavelength, determined by the ring properties, increases due to constructive interference as light travels multiple round trips in the ring. Since only specific wavelengths will experience constructive interference in the ring resonator, it can be used as a filter and evanescently couple the light out of the ring cavity with another waveguide. The specific wavelength is calculated by:

Equation 2-1

$$\lambda_o = \frac{L}{m} n_{eff}$$

where L is the circumference of the ring, n_{eff} is the effective index of the cavity waveguide, and m is the cavity mode order. In addition to the resonant wavelength, the resonator is characterized by its resonance width ($\Delta\omega$ or $\Delta\lambda$), free spectral range (FSR), and quality factor (Q), which can be calculated by:

Equation 2-2

$$\Delta\omega = \frac{2\kappa^2 c}{Ln_{eff}}, \Delta\lambda \approx \frac{\kappa^2 \lambda_o^2}{\pi Ln_{eff}}$$

Equation 2-3

$$FSR_{wavelength} = \frac{\lambda_o^2}{Ln_{eff}}$$

Equation 2-4

$$Q = \frac{\lambda_o}{\Delta\lambda_{3dB}} \approx \frac{\pi Ln_{eff}}{\lambda_o \kappa^2}$$

where κ is the coupling coefficient between A and B, and $\Delta\lambda_{3dB}$ is the resonance width at 3 dB. Derivations of these established relationships are detailed in [140]. These parameters are used to define losses in the system and the quality of the resonant peak, used to qualify the sensitivity of the transducer.

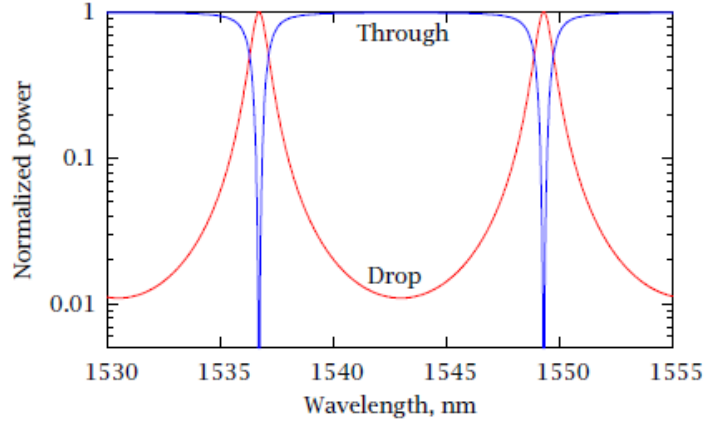


Figure 2-2. Spectral response of an optical channel dropping filter with a lossless ring. $L = 2\pi \times 9.55 \text{ } \mu\text{m}$, $n_{\text{eff}} = 3.15$, $\tau_1 = A\tau_2 = 0.9$. On resonance, all the power is transferred to the drop port.

2.1.2 Coupling Coefficient

When two waveguides are close to each other, the light in one waveguide will eventually transfer over to the second waveguide and then couple the light back to the first waveguide. This coupling can be illustrated by considering the modes of the two waveguides to be a superposition of the modes of the two individual guides. If only the lowest-order even-mode was used, a symmetric or anti-symmetric solution can be obtained. If all the power is in one waveguide, we can represent it as the superposition of the symmetric and anti-symmetric modes. Since the two modes have different n_{eff} , travelling speed, over some length (the “beat” length), the power is periodically transferred from one guide to another while the two waveguides are coupled in close

proximity. The beat length depends on the separation of the two waveguides and the difference in effective index of the two modes.

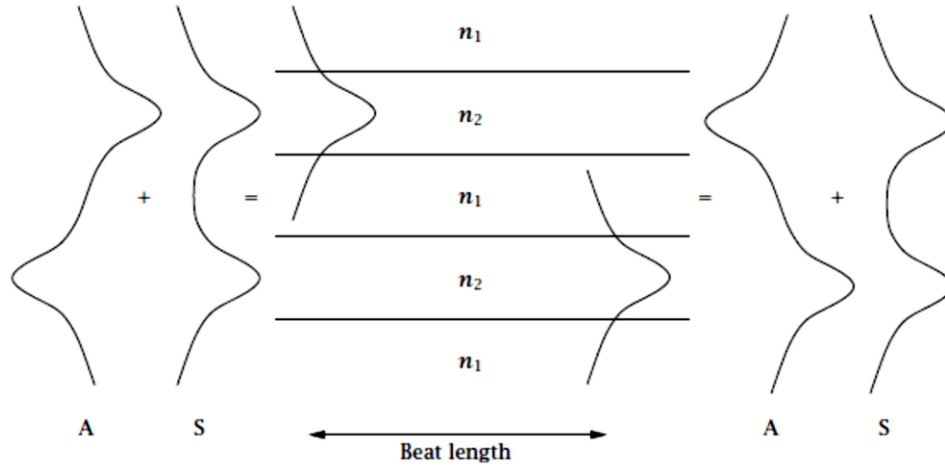


Figure 2-3. Diagram showing the coupling of two slab waveguides. The horizontal lines represent the interfaces between the core and cladding. The direction of propagation is left-to-right (or vice versa) [141].

If the coupling gap between the two waveguides and the physical coupling length (L_{PI}) between them are chosen properly, any fraction of the power from the input waveguide (BAR) can be coupled to the second waveguide (CROSS).

Equation 2-5

$$P_{BAR} = P_{IN} \cos^2(\kappa \cdot L_{PI})$$

Equation 2-6

$$P_{CROSS} = P_{IN} \sin^2(\kappa \cdot L_{PI})$$

Equation 2-7

$$\kappa = \frac{(n_{even} - n_{odd})k_o}{2} \sim \exp(-gap)$$

where $k_o = 2\pi/\lambda_o$. P_{BAR} and P_{CROSS} are both dependent on the coupling length and the effective indices of the even and odd modes [141].

2.1.3 Optical Losses

Loss can seriously degrade the characteristics of a ring resonator, since the $\Delta\lambda_{3dB}$ increases, and the Quality factor (Q) decrease. The degradation of Q directly affects the sensitivity of the resonator sensor. There are two optical loss mechanisms that need to be taken into account when designing and fabricating waveguides: bending and scattering losses.

2.1.4 Bending Loss

In ray optics, light is guided in dielectric waveguides by confining the propagating wave in a dielectric core bounded by a lower refractive-indexed cladding layer. The guided wave will reflect off the core-cladding boundary if the incident light is below a certain angle, the critical angle, and the phenomenon known as total internal

reflection will occur. Light which impinges at a larger angle than critical angle will not experience total internal reflection, generating a loss.

The ray-optics diagram depicts input rays entering a straight waveguide, Figure 2-4 (a), and a bent waveguide, Figure 2-4 (b), at a same angle (the dotted line represents the direction of the wave-vector).

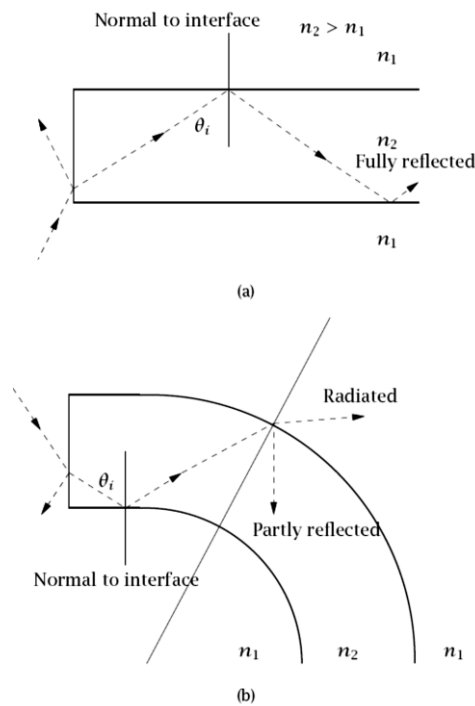


Figure 2-4 Schematic of wave propagation in (a) straight waveguide and (b) bent waveguide [140].

The ray in the straight waveguide is incident on the core-cladding boundary at a constant angle, experiencing total internal reflection. Thus the light is fully confined

without any losses. However, the angle of incidence increases in the bent section of Figure 2-4 (b) and the light is partially radiating out of the waveguide. The critical angle decreases with index contrast between the core and cladding. Thus, the larger the index contrast, the smaller the bending radius can be while maintaining total internal reflection. Bending loss needs to be taken into consideration when designing WGM resonators with small radiuses and is the defining parameter when deciding on the size and geometry of the resonator cavity.

2.1.5 Scattering Loss

The scattering loss is caused by a scattering wave due to the rough boundary between the core and cladding. Without a perfectly smooth plane, wave reflection scatters and total internal reflection will not occur. The scattering loss induced by the surface roughness of a waveguide can be modeled by Tien's theory [142],

Equation 2-8

$$\alpha_s = K^2 \left(\frac{1}{2} \frac{\cos^3 \theta}{\sin \theta} \right) \left\{ \frac{1}{\left[t + \left(\frac{1}{p} \right) + \left(\frac{1}{q} \right) \right]} \right\}$$

Equation 2-9

$$K = \left(\frac{4\pi}{\lambda} \right) (\sigma_{12}^2 + \sigma_{10}^2)^{\frac{1}{2}}$$

where θ is the angle of the rays propagating in the waveguide, $1/p$ and $1/q$ are the penetration depths of the modes into the cladding layers, t is the guide thickness, and K is a measure of the surface roughness defined by Equation 2-9, λ is the propagating wavelength through the waveguide, and σ_{12} and σ_{10} are the root mean squared of roughness between cladding layers ($\sigma_{12} = \sigma_{10}$ if the cladding layer is homogenous on all four sides). The penetration depth can be calculated by using wave theory of dielectric slabs guide [143]. From Equation 2-8, it is observed that the scattering loss in the waveguide is directly related to the surface roughness squared. The roughness of the sidewalls is typically related to the imperfection introduced by fabrication of the devices, which will be further detailed in Chapter 2. Scattering loss needs to be taken into consideration when designing the fabrication process flow of the resonators.

2.2 Design and Simulation

The whispering gallery mode resonator platform was designed based on theory, simulation, and fabrication and testing limitations and practicalities. The purpose of the designed resonator platform is to optimize the sensitivity of the sensor system, maximizing the wave-to-analyte interaction and signal-to-noise ratio.

The wave interaction with the analyte is restricted within the evanescent field located on the surface of the waveguide. The evanescent field intensity decays exponentially with increasing distance away from the surface (Equation 2-10). To

increase the sensitivity of the sensor, the evanescent field needs to be maximized, enabling stronger interactions outside of the waveguide. The evanescent field intensity normal to the sidewall, in the direction of “ z ”, decays exponentially based on,

Equation 2-10

$$I(z) = I_o e^{-\frac{z}{d}}$$

Where I_o is the intensity at the surface of the waveguide, and d is the penetration depth. The penetration depth is given by,

Equation 2-11

$$d = \frac{\lambda_o}{4\pi(n_1^2 \sin^2 \alpha - n_2^2)}$$

where λ_o is the wavelength of incident of light in a vacuum, α is the incident angle, and n_1 and n_2 are the refractive index of the waveguide and cladding materials, respectively. The penetration depth is independent of light polarity and decreases as the incident angle increases. Once the incident angle reaches the critical angle, d goes to infinity and the propagation of refracted light is normal to the waveguide surface. In order to extend the evanescent field, I_o needs to be maximized, and α , n_1 , and n_2 need to be taken into consideration.

In order to model the confinement of light inside and outside of the waveguide, waveguide geometric designs were simulated in COMSOL Multiphysics to solve for their optical modes. COMSOL Multiphysics mode analysis is made on the cross section of a rectangular dielectric waveguide surrounded on three sides by air and the bottom by a silicon oxide cladding layer (see Figure 2-5).

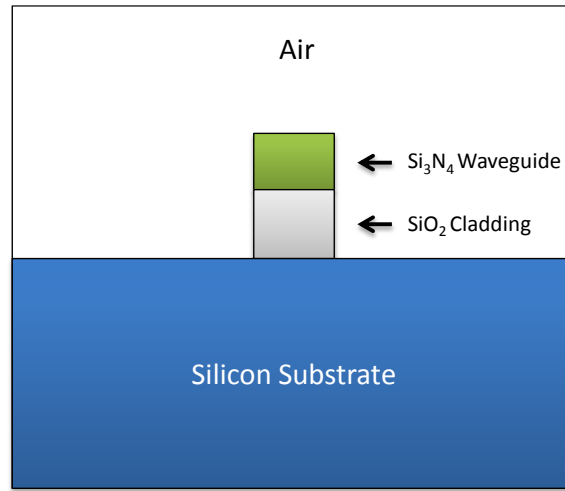


Figure 2-5 Diagram showing the cross section of a silicon nitride waveguide on a silicon substrate

The solver assumes a wave propagation in the ‘z’ direction, out of plane, with the form of

Equation 2-12

$$\mathbf{H}(x, y, z, t) = \mathbf{H}(x, y)e^{j(\omega t - \beta z)},$$

Where ω is the angular frequency and β is the propagation constant. An eigenvalue equation for the magnetic field \mathbf{H} is derived from Helmholtz equation,

Equation 2-13

$$\nabla \times (n^{-2} \nabla \times \mathbf{H}) - k_o^2 \mathbf{H} = 0$$

Which is solved for the eigenvalue $\lambda = -j\beta$.

Utilizing COMSOL Multiphysics, the waveguide geometries were optimized to maximize the evanescent field outside of the dielectric waveguide. The dielectric waveguide dimensions and material properties (i.e. refractive index and absorption coefficient) were largely restricted by fabrication limitations.

The primary modes of $\text{Si}_3\text{N}_4/\text{SiO}_2$ waveguide designs were simulated. The waveguide thickness was varied up to 1 μm with a constant width of 1 μm and a cladding thickness of 0.5 μm . The evanescent field outside the waveguide was measured by calculating the electrical field integral over a 100 nm thick border around three air-cladded sides of the waveguide, see Figure 2-7, where majority of the nano-bioreceptor resides. 0.4 μm thick waveguide possessed the highest electrical field integral. The thin waveguide core causes the mode to partially reside in the cladding layer. Further decrease in waveguide thickness would push the mode further into the cladding layer and into the leaky Si substrate. To prevent leakage into the substrate, a thicker cladding layer is required, which would pose additional fabrication challenges.

A slightly thicker core may be used, sacrificing some evanescent field to ease the fabrication requirements.

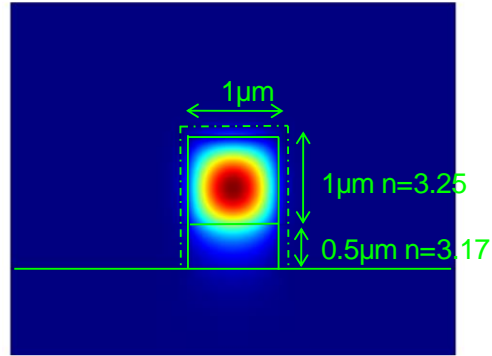


Figure 2-6 Simulation showing the primary optical mode profile in a square (side = $1.0\mu\text{m}$) silicon nitride waveguide sitting on a $0.5\mu\text{m}$ thick silicon oxide cladding

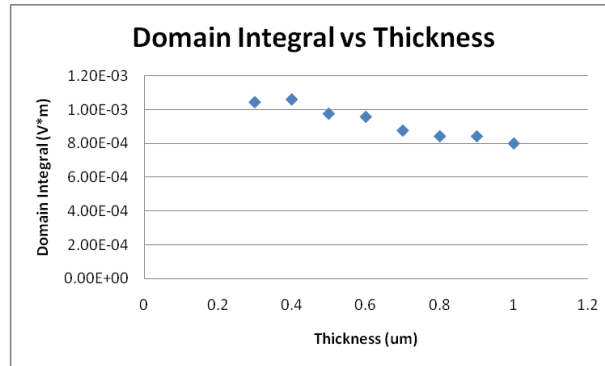


Figure 2-7 Intensity of evanescent profile 100 nm outside of the dielectric waveguide for different waveguide thicknesses

Core thicknesses below 200 nm were simulated but the Si_3N_4 waveguide would not support any modes. Core thickness larger than 0.5 μm supported second or higher ordered modes.

Alternative designs were simulated in COMSOL Multiphysics to further increase the optical propagation outside the waveguide. These designs are too complex to be fabricated due to complications in material growth, stress and strain balances, and high aspect ratio etch profiles. As a result, these results are only used for theoretical and conceptual understanding and may provide insights for future system designs.

Single and double vertical slotted waveguides were simulated with 50 nm and 100 nm slotted gap distances. The power density profile of the transverse electric (TE) and magnetic (TM) mode of the slotted waveguide vary greatly. While the primary TE mode resides in the dielectric layers and above the waveguide, the primary TM mode is concentrated within the lower indexed narrow slot, (Figure 2-8). The measurement of the electric field integral over a 100 nm thick boarder of these four designs are summarized in Table 2-1 through Table 2-4.

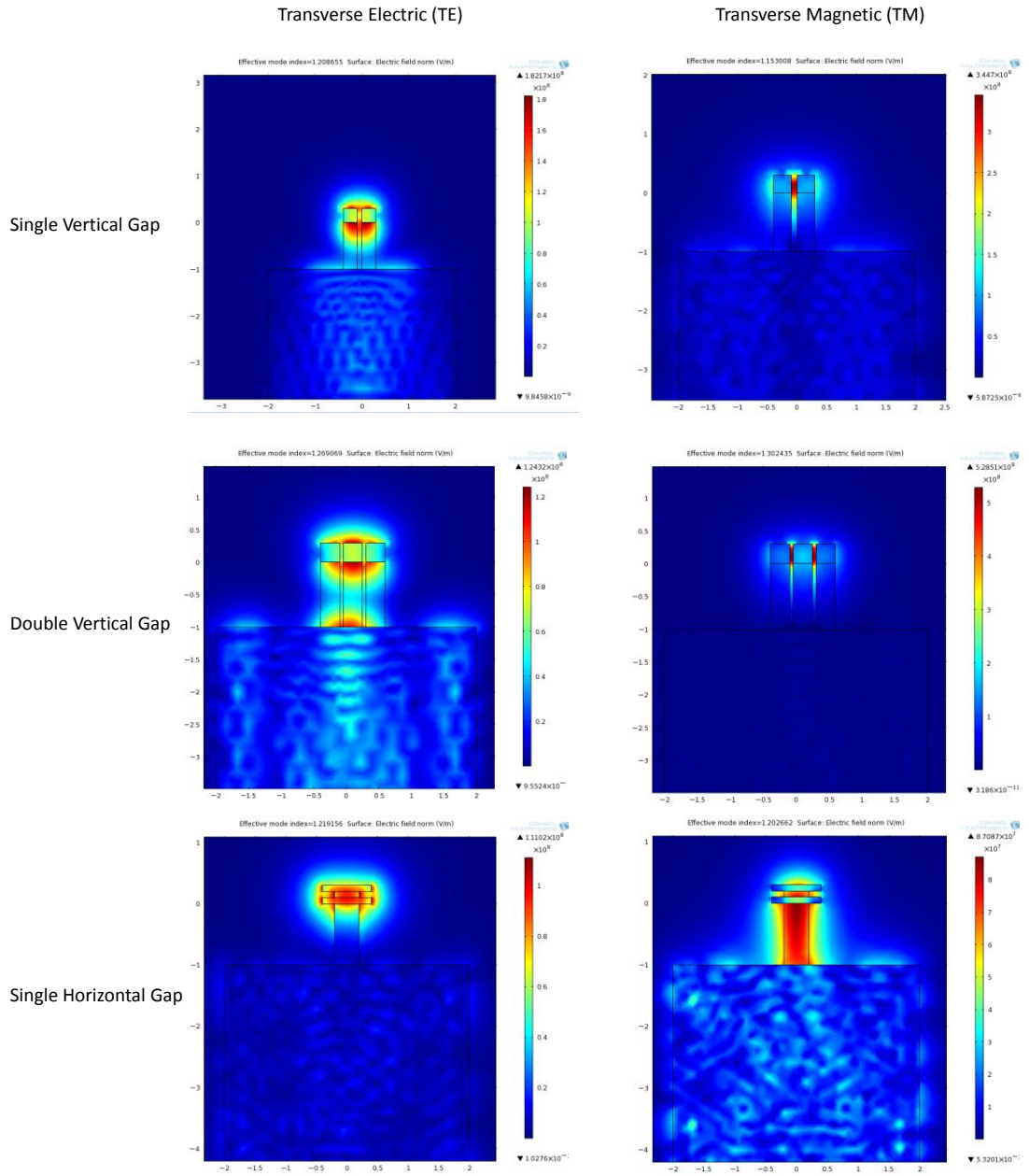


Figure 2-8 Simulation profile of optical modes (both TE and TM) in different waveguide geometries

Table 2-1 Electric field integral for single vertically slotted waveguide designs

Single Vertically Slotted Waveguide		
Waveguide Height (nm)	Gap Distance (nm)	Effective Index
300	100	1.153
300	50	1.199
500	50	1.297

Table 2-2 Electric field integral for double vertically slotted waveguide designs

Double Vertically Slotted Waveguide		
Waveguide Height (nm)	Gap Distance (nm)	Effective Index
300	50	1.302
300	100	1.230

Table 2-3 Electric field integral for three horizontally layered waveguide design

Three Horizontally Layered Waveguide			
Top Si₃N₄ Layer (nm)	Middle SiO₂ Layer (nm)	Bottom Si₃N₄ Layer (nm)	Effective Index
100	100	100	1.203

Based on these results, it can be concluded that these designs increase the propagation of light outside the dielectric waveguide and wave-analyte interaction compared to conventional rectangular designs. This would, in theory, increase the sensitivity of the transducer design if the following two assumptions were held true: (1) the assembly density of the nano-bioreceptor layer is uniform on all waveguide cladding surfaces and (2) the diffusion of analyte is not inhibited by the waveguide geometry.

It is believed that the gap distance would inhibit the diffusion of both the bio-nanostructured receptor layer and the targeted analyte so that the densely occupied optical region would be ineffective to interact with the bioreceptor layer and analyte. As a result of this degradation in sensor performance, coupled with fabrication challenges, vertical slotted and horizontally layered waveguide designs were not pursued further.

Based on the simulation and modeling results and taking in to account fabrication limitations, the following set of designs were developed and fabricated:

Table 2-4 Optical resonator design parameters

Coupling Gap Distance	100 nm – 300 nm
Resonator Radius	20 μm – 100 μm

Rectangular Waveguide Width	0.6 μm , 1.0 μm
Rectangular Waveguide Thickness	0.4 μm , 0.6 μm

The simulations and modeling are the basis of the platform design, narrowing the design parameters and obtaining an acceptable range of working conditions for the system. However, fabrication and testing environments can impede the ideal condition of the system. All designs were fabricated and tested. However, the final geometric design of the transducer platform was established empirically, derived from the design constraints above.

Chapter 3. Fabrication and Testing of Optical Resonators

3.1 Fabrication

The fabrication process flow of the optical resonator was aimed at developing a highly sensitive transducer compatible with functionally versatile nanostructured bio-receptor layers. The process was developed based on the design parameters presented in Chapter 1. Fabrication was conducted at two cleanroom facilities, the University of Maryland Nanocenter, FabLab, and the cleanroom at the Laboratory for Physical Sciences (LPS), where assistance was provided by Dr. Nathan Siwak. An abridged fabrication process flow is shown in Figure 3-1 and detailed fabrication recipes are listed in Appendix B.

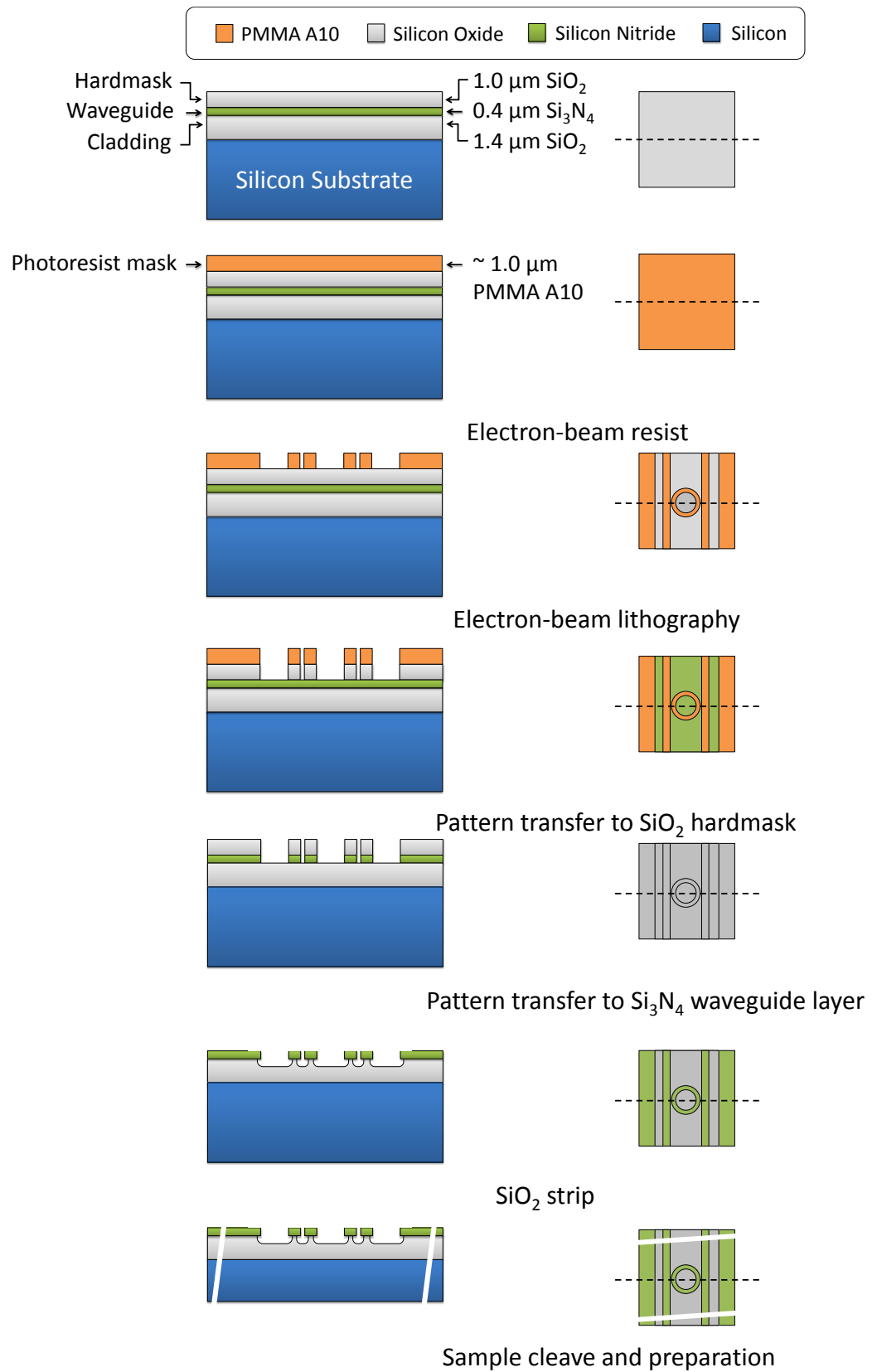


Figure 3-1 Diagram showing the abridged fabrication process for of an optical ring resonator.

3.1.1 Layer Structure

The optical waveguide was composed of a 0.4 μm thick Si_3N_4 core and 1.0 and 1.4 μm thick SiO_2 cladding layers (Figure 3-2).

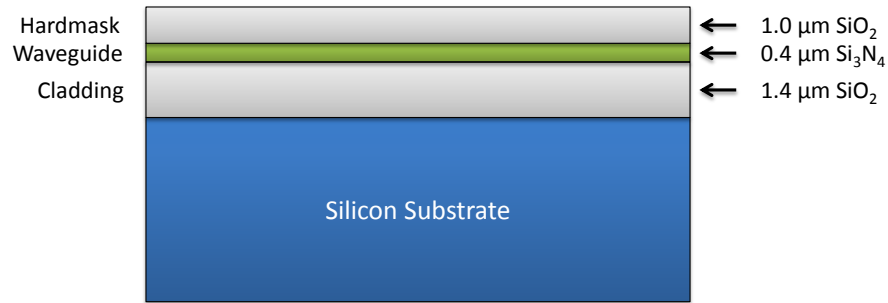


Figure 3-2 Diagram showing the material layer stack

The bottom 1.4 μm thick silicon oxide layer, used as an optical cladding layer, was wet thermally grown using Tystar Low Pressure Chemical Vapor Deposition (LPCVD) at the FabLab. The bottom cladding layer was grown as thick as possible to reduce waveguide loss, but was limited to 1.4 μm by the diffusion of oxygen into the silicon substrate. The oxide thickness is quadratically proportional to the growth time.

A 0.4 μm thick stoichiometric Si_3N_4 ($n \approx 2.0$) was deposited using LPCVD immediately following the lower SiO_2 cladding growth. While stoichiometric Si_3N_4 generally possesses higher tensile stress [10], it exhibits lower optical absorption than

the low-stress non-stoichiometric silicon nitride. The 0.4 μm thick Si_3N_4 was chosen to fit within constraints derived from the modeling and simulation detailed in Chapter 2. An N&K Spectrophotometer Analyzer was used to non-destructively verify the thickness of the deposited dielectrics.

A final 1 μm silicon oxide layer was deposited on the top layer of the stack to be used as a hard mask for the optical waveguide and resonator patterning. This hard mask needs to be patterned by a high resolution resist while remaining resistant enough to mask the Si_3N_4 layer below. The material composition and thickness were empirically derived based on fabrication compatibility and processing. Different hard mask materials, including polymers and metals, were initially investigated for the etching of the waveguide layer but could not be patterned easily or proved to be inefficient as masking layers. Silicon dioxide was finally explored as a top masking layer after satisfying the patterning and masking requirements for the waveguide layer. The top 1.0 μm oxide layer was deposited using an Oxford Plasma Enhanced CVD (PECVD) at 300°C (see Appendix B for the detailed recipe). The details of this process development will be further discussed in Section 3.1.3.

3.1.2 Electron Beam Lithography

Due to the submicron resolution needed for the waveguide/resonator coupling designs, electron beam (E-beam) lithography was required to pattern the waveguide

and the optical cavity. E-beam, unlike conventional optical lithography (i.e. projection, contact, or proximity lithography), is a maskless, direct-write lithography technique used to generate desired patterns. As the name indicates, e-beam lithography utilizes a focused electron beam that is selectively rastered across a resist covered surface.

E-beam is capable of patterning sub-micron features because it circumvents the critical dimension (CD) limitations of traditional optical lithography, which are dependent on the wavelength of light used for photoresist exposure. The minimum resolvable feature in optical lithography is given by:

Equation 3-1

$$W_{min} = k_1 \cdot \frac{\lambda}{NA},$$

Where W_{min} is the minimum feature size, k_1 a constant coefficient that encapsulates process-related factors, NA is the numerical aperture of the lens that focuses the beam on the wafer, and λ is the wavelength used. Utilizing a conventional UV 5x projection lithography in an academic setting, the CD is typically 0.5 μm . To achieve CD's of 100-300 nm, electrons are used instead of light. The minimum resolvable feature size of E-beam is not limited by the beam size, but rather the scattering of primary and secondary electrons.

An E-beam lithography system is very complex and consists of many different components. More detailed descriptions of an E-beam system are provided in the literature [144-146]. A very simplified model of an E-beam lithography system can be divided into 3 components: the electron gun, the electron optical column, and the sample surface.

The term electron gun is used to describe the electron emitter that supplies electrons to the electron optical column for focusing. Lower resolution systems use thermionic sources, which have a broader energy spectrum emission. Thermionic sources consist of a filament which is heated to emit electrons from the surface. When a high voltage is applied between the filament and an anode, the excited electrons accelerate toward the anode. By varying the voltage, the beam's trajectory and focus can be controlled. A commonly encountered example of thermionic filaments is the lanthanum hexboride (LaB_6) electron source. Systems with higher resolution require the use of field electron emission sources, such as zirconium oxide coated tungsten (ZrO_2/W) needles. Field electron sources emit electrons under high intensity electric field and are often differentiated from thermionic emission by using the term "cold emission". Field electron emission has lower energy spread, "monochromatic" electrons, and enhanced brightness, and as a result it is ideal for high resolution microscopes and E-beam lithography writers.

The electron optical column takes the electron beam produced in the electron gun and utilizes a system of electrostatic and magnetic lenses to direct and focus the beam to the desired location on the sample. Early electron beam systems used Gaussian-shaped beams and raster scanned the sample surface, blanking the beam in order to generate specific patterns. Modern systems utilize shaped beams which are deflected to specific locations in the write field using vector locations, decreasing the necessary write time.

The sample surface is covered with a resist as in other conventional lithography techniques. The resist polymer is normally less wavelength specific than traditional optical photoresists because the high e-beam energy will typically break up bonds in any polymer. However, due to the high electron energy incident on the sample surface, the secondary electrons generated in the resist volume can unintentionally expose neighboring areas of the resist. Higher resolution patterns can be easier resolved in thinner resist due to decrease probability of electron scattering. However, the resist needs to be robust and thick enough to act as a mask to protect the layer beneath during the following etch step. A thicker photoresist is better at protection. However, due to the spread of electrons through the thicker resist, smaller dimensions are harder to resolve. As a result, a balance of the resist thickness and the achievable resolution had to be determined.

The Raith e_LiNE lithography tool at the University of Maryland Nanocenter was used for all photolithography characterization and processing. The Raith e_LiNE is an ultra-high resolution electron beam Lithography and nano engineering workstation. It possesses a thermal assisted field emission gun to help obtain the sub-100 nm resolution needed to resolve the coupling gap between the optical waveguide bus and the resonator cavity. To resolve such small dimensions reliably, sample surface conditions needed to be optimized and the E-beam exposure condition needed to be characterized.

3.1.2.1 Sample Preparation

The lithography process characterization samples were prepared by first cleaning the wafer using acetone, methanol, and isopropanol (IPA). After dehydrating the wafer on a hot plate at 180°C for five minutes, it was transported directly onto a spinner for E-beam resist spin coating.

Poly(methyl methacrylate) (PMMA) is a popular commercial positive resist that has ultra-high resolution and great reproducibility. It has excellent surface adhesion properties with a very long shelf life. It's selectivity to dry etch chemistry is, however, relatively poor. PMMA requires an E-beam dosage between 50 and 500 $\mu\text{C}/\text{cm}^2$ depending on the beam source and equipment used. PMMA A10 (10% PMMA dissolved in anisole) and A2 (2% PMMA dissolved in anisole) were spun at 500 RPM

for 10 seconds followed by 4000 RPM for 45 seconds. The wafers were transferred to a hot plate for pre bake at 180°C for 90 seconds, resulting in a final A10 and A2 resist thickness of 1.6 µm and 200 nm, respectively. The wafers were then cleaved into approximately 15 mm by 15 mm square dies, ready to be written by E-beam lithography.

3.1.2.2 E-beam Write

In order to resolve features that are sub-100 nm and asymmetrically designed and located next to micron scale structures, beam and write conditions needed to be systematically characterized.

To characterize the dosage needed, both time and exposure area had to be taken into account as governed by the following equation:

Equation 3-2

$$D \cdot A = T \cdot I$$

where T is the time to expose the object (which equals (exposure time)/(step size)), I is the beam current, D is the dose, and A is the area exposed. The minimum step size is dictated by the tool (16 nm here); the beam current is dependent on the beam energy, (160 pA to 175 pA), dependent on the condition of the tool at 30 keV; the area exposed is based on the design dimensions; and the dosage can be controlled and calibrated. The

exposure time dictates the total length of time to write and is limited by the practicality of conducting the write in a reasonable period of time.

To calibrate the appropriate dose for a specific pattern, a 2D calibration grid of test structures was designed to vary the test structure dimensions and exposure dosage. The first generation of the calibration grid included a wide range of waveguide and coupling gap designs and a portion of various optical resonator designs (disk, ring, and racetrack resonators), see Appendix A. The calibration grid was used to optimize the beam energy, which was varied from 10 keV to the system's maximum of 30 keV. The highest resolution patterning was resolved using the higher electron beam energies due to less probability of electron scattering in the resist exposure region (see Figure 3-3). The higher beam energy penetrates deeper into the layer stack and causes electron scattering below the resist layer. This decreases the lateral resolution especially with nested and large pattern designs.

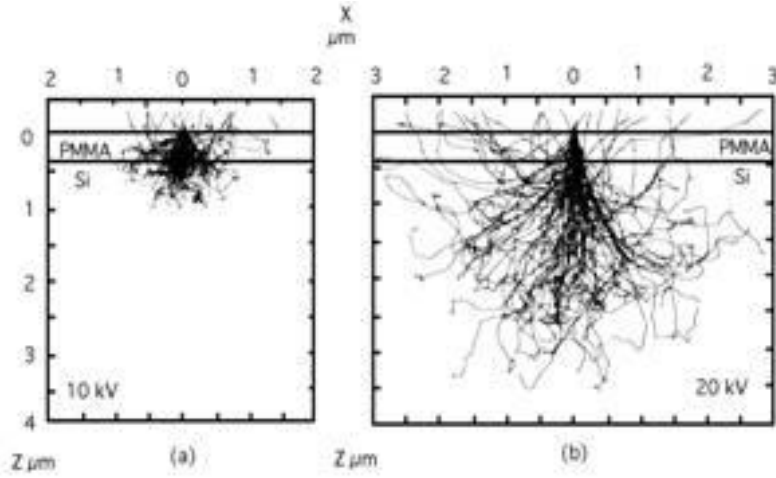


Figure 3-3 Monte Carlo simulation of electron scattering in a 400 nm thick PMMA resist of two different beam energies. (a) The 10kV beam showed electron scattering mostly in the PMMA layer and (b) the 20kV beam showed electron scattering mostly residing in the Si substrate beneath the PMMA layer [147].

Dose characterization grids consisted of a coarse grid, dose factor step size of 0.5, and then a finer grid, with a dose factor step size of 0.05. The optimal dosage range was determined by the inspection of the post-developed patterns with scanning electron microscopy (SEM). From each dose grid, an optimal dose was selected and divided into finer step sizes in the next subsequent dose grid in the development cycle. The waveguide width and the coupling gap of each test structure were compared to that of their layout designs and the error, $\frac{D_{measured}-D_{design}}{D_{design}} \times 100\%$, was calculated and plotted with respect to dose in graphs below.

PMMA A2 dose Grid Characterization

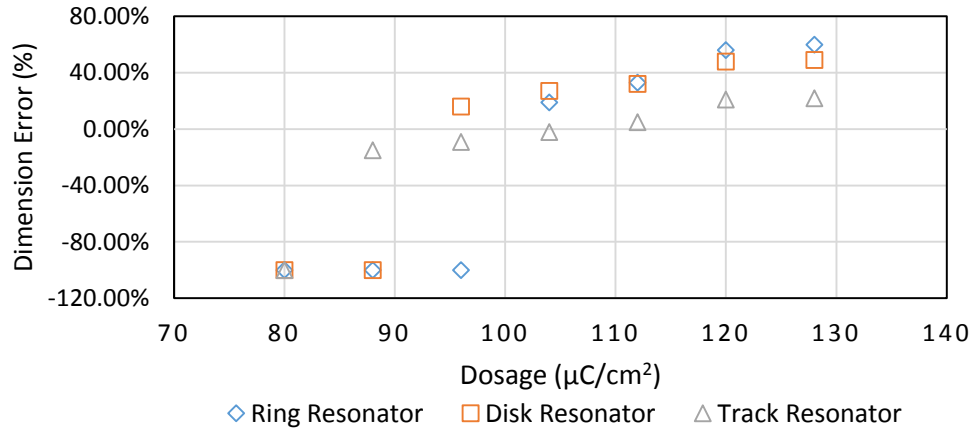


Figure 3-4 PMMA A2 dose grid characterization of ring, disk, and track resonator designs (unresolved gaps were given a -100% dimension error)

Based on the initial dose grid, it was immediately apparent that the PMMA A2 did not require any fine refinement. The initial dose characterization grid resolved dimensions down to ~ 100 nm with a dosage of $96 \mu\text{C}/\text{cm}^2$ (see Figure 3-5). However, due to its limited effectiveness as a masking layer as a result of its thin coverage, PMMA A2 was quickly abandoned.

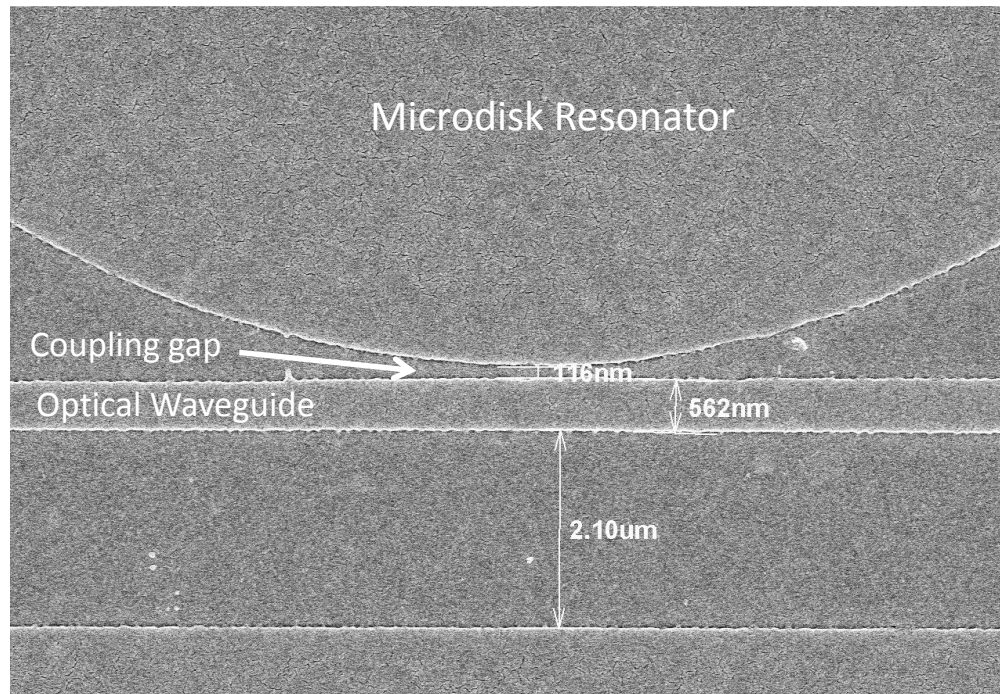


Figure 3-5 SEM image showing a 116 nm coupling gap resolved in PMMA A2 resist using E-beam lithography

The dose grid of the PMMA A10 showed a very different result summarized. The narrow coupling gap required a higher dosage to resolve compared to that of the large micron scale structures which defined the waveguides. This is explained by the proximity effect, where adjacent regions to the exposed area get exposed during the writing of features, expanding their dimensions and decreasing contrast between maximum and minimum exposure intensity. The proximity effect is caused by electron scattering, which ultimately defines the resolution of the pattern. Electron scattering is the deflection of primary electrons as they penetrate through the resist and layers

beneath and the generation of secondary electrons in all directions upon the impingement of the primary electrons (see Figure 3-6).

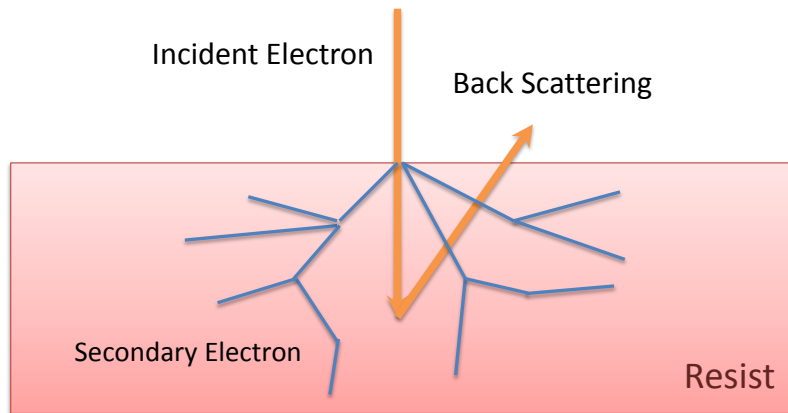


Figure 3-6 Diagram showing the possibility of back and secondary electron scattering in resist

The forward and backward scattering electrons can lead to complete exposure of resist over an area much larger than the geometry defined by the beam size. The proximity effect generally affects large nested features where the spill over exposure compounds the exposure intensity and extends the dosage. As a result, it was necessary to add proximity effect compensation to the design by adjusting the dosage based on the geometry of the pattern.

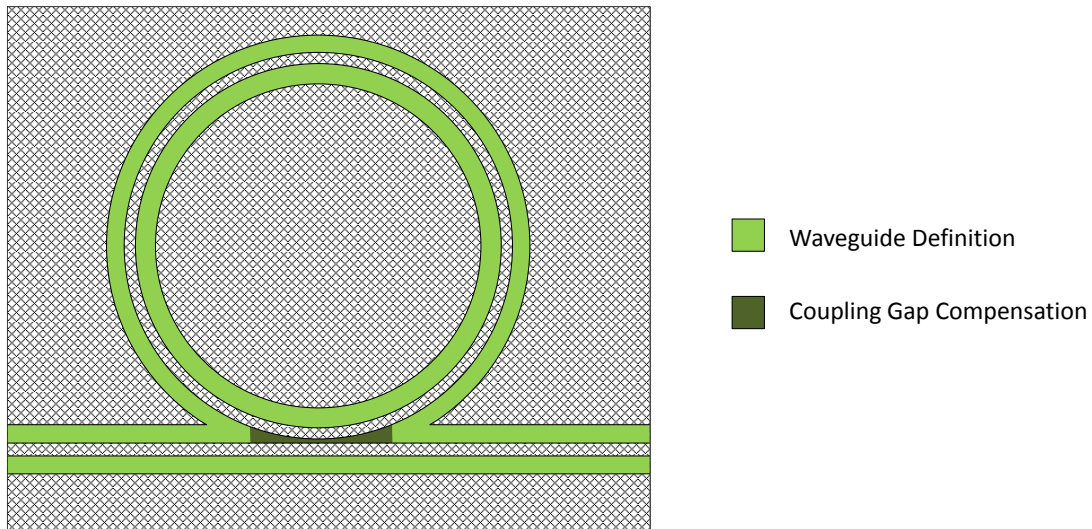


Figure 3-8 Diagram showing the regions exposed to Waveguide Definition dosage (light green) and Coupling Gap Compensation dosage (dark green) for a ring resonator design

Another set of dose grids was designed to compensate for the discrepancy between the sub-micron wide coupling gap and the 2 μm wide waveguide definition. The dosage of the coupling gaps and micron scale patterns were independently varied and analyzed using microring, disk, and track resonator structures. By analyzing the characterization grid, the final dosage for each dimension was selected: $D_{\text{Coupling_Gap}} = 360 \mu\text{C}/\text{cm}^2$ and $D_{\text{Waveguide_Definition}} = 248 \mu\text{C}/\text{cm}^2$. Based on these parameters, 1.0 μm waveguides resulted in a width of $0.9 \pm 0.1 \mu\text{m}$ and the 100 nm coupling gap resulted in a gap width of $105 \pm 15 \text{ nm}$. While it was easier to resolve a long coupling gap for a track ring resonator with a relatively constant and symmetric geometry along its

coupling gap, it was the most difficult to resolve a microring resonator. The microring resonator has an asymmetric coupling gap design where proximity effects contributed differently on each side of the two 1.0 μm wide waveguides. Due to this asymmetric balance across the waveguide, the coupling gap dimension changed dramatically during the remaining stages of fabrication. As a result, microring resonator designs were ultimately abandoned and only the microdisk and racetrack designs were pursued.

3.1.2.3 PMMA Development

Post E-beam exposure, the resist was developed in a 1:3 mixture of methyl isobutyl ketone (MIBK):IPA for 60-90 seconds. This dilute mixture of MIBK and IPA decreases the aggressiveness and the sensitivity of the development process and enhances the resolution. The development time was not critical. It was observed that even when extending the development time past 150 seconds, pattern resolution did not change significantly. The chip was finally rinsed in IPA for 60 seconds and dried either at room temperature or on a hot plate at 50°C. The E-beam patterned PMMA pattern was then ready to be transferred to the SiO₂ dielectric hard mask below.

During the process, resist exposed beneath the surface due to surface scattering effects was observed. This created a concave sidewall. The surface tension of the wet process pulls the slender structure to one side if there is any asymmetry across both sides of the waveguides. This was largely observed when the coupling gap dimensions

increased beyond the typical overexposure, leading to the belief that there was a physical displacement of the waveguide, see Figure 3-9.



Figure 3-9 SEM showing physical delamination of PMMA resist due to the resist development stage

3.1.3 Dielectric Waveguide Patterning

Many methods were investigated and characterized to transfer the patterned resist to the nitride waveguide layer, including various hard mask materials, etch tools, and other processing conditions. These characterization steps were needed to realize the 100 nm gap feature and minimize the sidewall roughness. Based on the coupling gap dimensions and the necessary photoresist thickness, the coupling gap required an aspect ratio of at least 4:1 with close to 90° sidewall verticality.

Metal hard masks have been used in literature to realize high aspect ratio structures due to their high selectivity to the chemical etch of silicon-based materials [148]. Because of this high selectivity, only a thin layer of metal would be required as a hard mask. They have been used as single [149, 150] or double layer mask [151] to define bulk and surface micromachining for dielectric layer patterning. Based on these advantages and previous work, a Cr layer was first selected as a single layer hard mask for the Si_3N_4 waveguide layer and later used as a double layer mask to pattern a SiO_2 hard mask (see Figure 3-10).

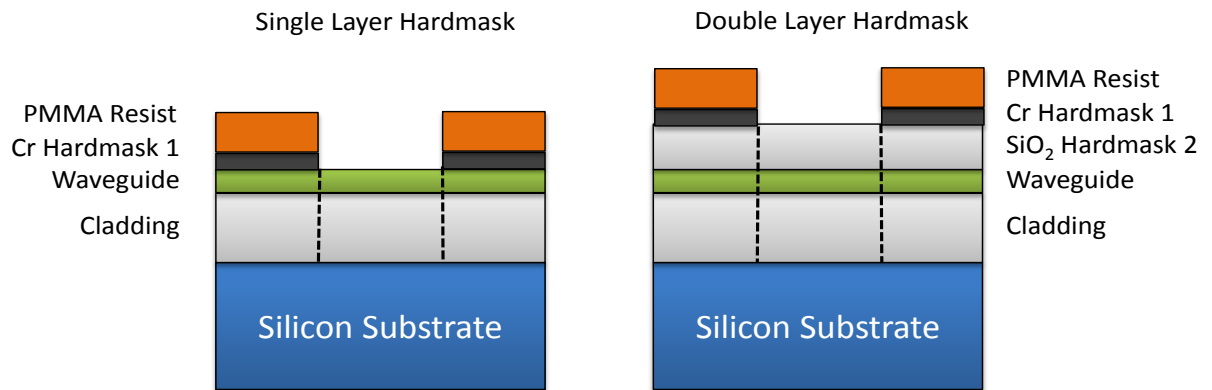


Figure 3-10 Cross sectional diagrams showing the single layer hardmask (left) and double layer hardmask (right) layer stack

The 200 nm thick Cr was deposited using an AJA sputtering unit (see Appendix B for deposition details). The Cr layer was first etched using a wet Cr etchant. This resulted in a significant over-etch do to the isotropic nature of the wet etchant and the

size of the features. A more anisotropic etching technique, reactive ion etching (RIE) and inductively coupled plasma (ICP), was used to transfer the PMMA pattern to the metal layer.

Reactive ion etching is a dry etch process that utilizes ions generated by plasma to react with the material being etched. Plasma is generated by a high intensity RF field between two parallel electrodes. A DC bias voltage can be applied between the electrodes to generate a uniform field and provide a directional etch preference. RIE is ideal for smooth sidewall anisotropic etches because it combines the advantage of the selective chemical etch and the directionality of a physical etch. The Inductively Coupled Plasma (ICP) is a plasma enhancement method used in the RIE system to increase the etch rate and directionality. A spiral coil is placed outside of the RIE's cylindrical chamber. When an AC current is passed through the coil, it induces an azimuthal current within the RIE chamber intensifying the existing plasma.

A chlorine based RIE gas chemistry was selected to etch the Cr layer due to chlorine ion's high reactivity to Cr. This etch process was highly aggressive. Even under a low RIE bias (30 W) and minimal ICP conditions (50 W), Cr etched at a rate of more than 14 nm/second and completed the 200 nm etch in less than 15 seconds. The etch process also consumed the PMMA masking material and exposed the waveguide layer beneath. An alternative etch method would be preferred if the

selectivity between PMMA and Cr was more favorable. Ion milling process was used next in an effort to etch the Cr layer but protect the waveguide.

Ion milling is a purely physical etch that bombards the surface of the sample directionally with Ar ions. Due to the non-reactivity of noble gases, the etch selectivity of ion milling is close to 1:1. The PMMA masked Cr was ion milled for 30 minutes at a current density of 0.27 mA/cm^2 (see Appendix B for detailed recipe), resulting in the complete transfer from the patterned PMMA layer to the Cr layer. However, the issue of micromasking was apparent in the following dielectric etch process, where high aspect ratio nano-pillars appeared in etched cavities. This was due to metal nanoparticles that were left behind on the surface during ion milling due to limited vacuum levels. These nanoparticles, with a high selectivity to silicon-based etch chemistry, acted as a micro-mask, creating nano-pillars when patterns are transferred to the layer below (Figure 3-11).

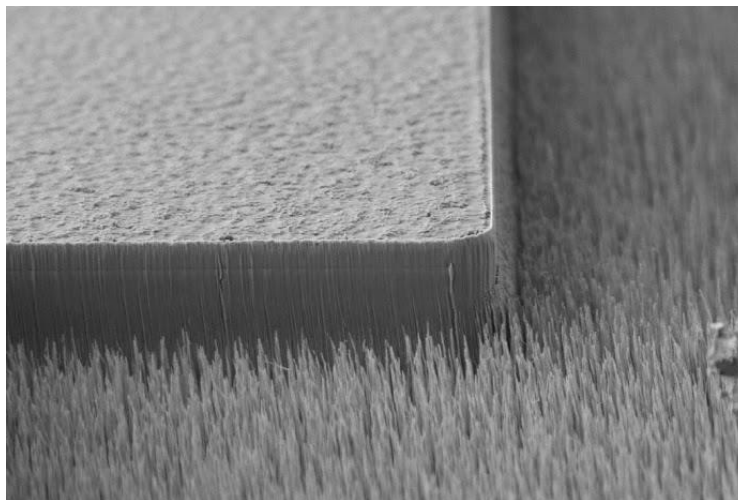


Figure 3-11 SEM image showing nano-pillars in the etched trenches due to micromasking from metal nanoparticles.

The limitation of the ion milling tool to increase the vacuum further prevented further process optimization and consequently the use of a metal mask was abandoned. The alternative process is to use a single layer SiO_2 hard mask.

PMMA is very reactive with chlorine based chemistry but less reactive with fluorine based chemistry, used to etch silicon-based materials. A fluorine-based chemistry will effectively etch the SiO_2 hard mask but preserve the PMMA layer. A RIE process was used to further decrease the aggressiveness of the physical etch. The process was conducted at the Laboratory for Physical Sciences (LPS) using a Plasmatherm RIE model 790 (all processes using the Plasmatherm RIE was conducted by colleague Dr. Nathan Siwak). The recipe used was previously characterized to result

in a high selectivity to photoresists and to produce close to 90° vertical sidewalls. A 10% overetch was employed to etch the 1.0 μm thick SiO_2 and compensate for etch variation across the surface. A 33.3 minute SiO_2 etch successfully transferred the PMMA pattern into the SiO_2 hardmask (see Figure 3-12). The coupling gap was successfully transferred with minimal changes in lateral dimensions. Nano-masking did not reoccur using the RIE process.

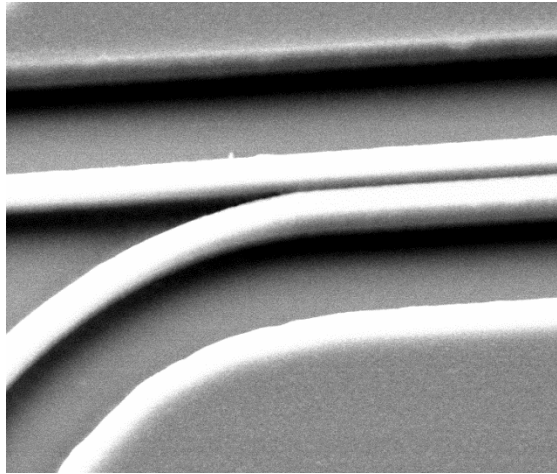


Figure 3-12 SEM image showing the successful pattern transfer, resolving the coupling gap and no signs of nano-pillars

After the successful pattern transfer into the SiO_2 hard mask layer, the pattern was transferred to the 400 nm thick Si_3N_4 waveguide layer. The selectivity between SiO_2 and Si_3N_4 does not need to be great due to the thicker SiO_2 hard mask compared to the Si_3N_4 waveguide etch layer. A fluorine-based RIE recipe (detailed in Appendix B) was

used to transfer the pattern using the same Plasmatherm RIE. Without breaking vacuum, Si_3N_4 was etched for 2.9 minutes using this fluorine based recipe, which includes a 10% over-etch to compensate for the etch non-uniformity. This concluded the patterning of the optical device.

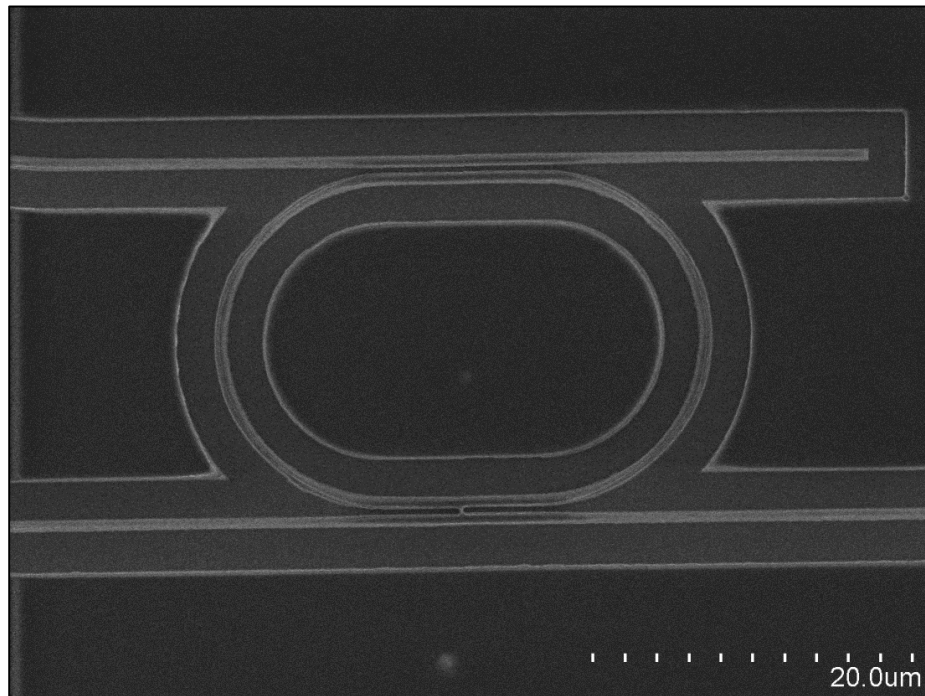


Figure 3-13 SEM image showing a completely fabricated track-ring resonator in Si_3N_4 waveguide layer

The SEM inspection of the completely patterned resonator showed a good pattern transfer. The sidewall roughness was difficult to measure due to imaging limitations but was estimated to be below 100 nm. The main contributor to the sidewall

roughness was the lateral waviness of the resist. Due to the small size of the chip, no noticeable variations were observed across devices.

3.1.4 Chip Preparation

The chip underwent an O₂ plasma clean and an acetone-methanol-IPA dip to remove any organic residues left on the surface before stripping off the SiO₂ masking layer. The oxide mask layer was stripped off by a 2-minute timed 6:1 buffer oxide etch (40% NH₄F in water to 49% HF in water). A timed etch is required because the isotropic wet etch will undercut the oxide cladding beneath the waveguide if left in the etchant too long. The waveguide, without an anchor to the substrate, would be released and no longer operational.

In order to optimize optical coupling via cross section butt coupling at the edges of the chip, crystalline smooth facets are required. To obtain good quality crystalline facets via cleaving, a very thin sample is required, typically less than 250 μm thick. Conventionally, this is done by using chemical-mechanical planarization (CMP). However, due to lack of access to a CMP tool, the substrate was thinned down by mounting the chip backside up onto a carrier wafer, using acetone dissolvable wax, and then etching it from the back side using a blanket Deep Reactive Ion Etching (DRIE). After a 75-minute etch, the substrate was thinned down to 250 μm and was successfully cleaved.

3.2 Characterization of the Optical Resonator

The optical resonator was tested in a custom optical setup at the MEMS Sensors and Actuators Laboratory. The optical loss, resonant conditions, stability, and minimum Refractive Index Unit (RIU) resolution was characterized for each resonator. These properties are key factors that influence the performance of an optical resonator sensor.

3.2.1 Testing Setup

The resonator's optical characteristics were evaluated with a custom testing setup. The optical setup is composed of an input optical source, an output photodetector, micropositioners, and tapered optical fibers to couple light on and off chip. The optical source is a Venturi Tunable Laser TLB-6600 with a tuning range of (1520 nm – 1620 nm) and a maximum output power of ~8.55 mW. The optical source is coupled on to chip using a lensed single-mode fiber by coupling the light to the on-chip input port via a small air gap. The output light signal was captured either at the drop or through port, also using a lensed fiber, and then guided to a high speed photodetector (New Focus Model 1811). The input and output lensed optical fibers are mounted on electrostatically controlled XYZ stages to allow for fine-adjustment of fiber position for optimal coupling. The sensor chip is mounted on an aluminum chuck which is secured to a third XYZ stage.

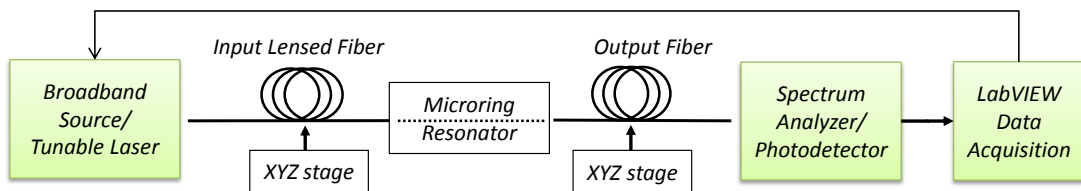


Figure 3-14 Block diagram showing the optical testing setup

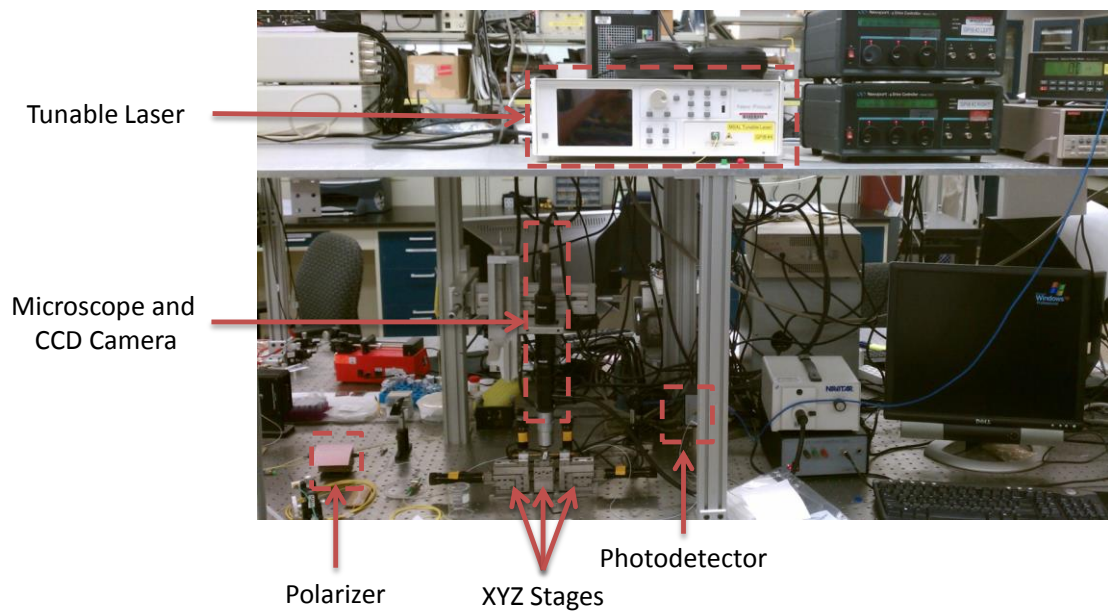


Figure 3-15 Picture showing the testing setup on an optical table.

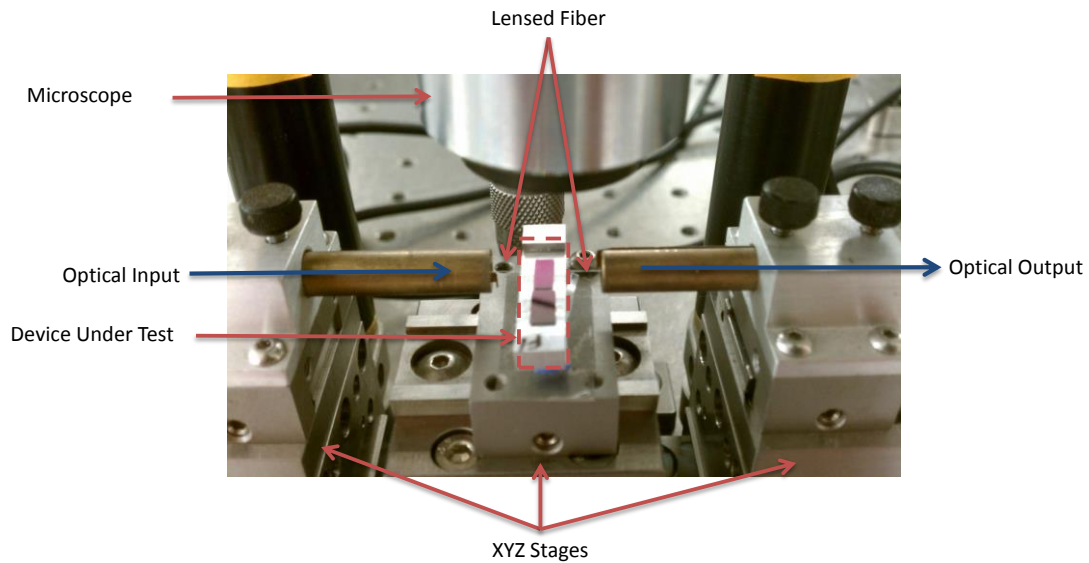


Figure 3-16 A picture showing optical coupling on to and off of chip via lensed fiber secured on xyz stages.

To obtain an optical spectrum of the optical device under test, the tunable laser output wavelength is synchronized with the acquisition of the photodetector via a custom LABVIEW program. The LABVIEW program triggers the start of the tunable laser output wavelength scan and at the same time acquires and records the photodetector's output signal. The program then correlates the acquired signal with the output wavelength and records the data. The photodetector's integration time is dictated by the scan speed of the tunable laser and the number of averaged scans. The scan speed of the tunable laser is 100 nm/s. Typically, a spectrum is captured by averaging 10-25

scans. A longer integration time helps to resolve the peaks in the optical spectrum and averages the noise in the system, which is dominated by the mechanical vibration of the setup and may cause misalignment between the lensed fiber and on-chip waveguide.

Data is imported into Origin in order to analyze the resulting spectra. Peak fitting to a single Gaussian curve is used to obtain the parameters to characterize the optical resonator, including its optical loss, quality factor, and resonant frequency.

3.2.2 Optical Characterization

To utilize this optical resonator transducer as a refractive index sensor platform, the optical setup, the acquisition method, and the baseline spectrum of the resonator were all characterized. The sensor system's overall resolution and sensitivity was established by independently and systematically investigating the noise level and the stability of each component.

The optical loss of the system was first characterized to determine the optical intensity and the signal to noise level of the optical coupling through the acquisition setup and the on and off chip coupling. The optical loss associated with acquisition setup (the fiber connectors, polarizer, and the photodetector) is -4.56 dB, measured by bypassing the lensed fiber and the test chip and directly connecting the output waveguide from the polarizer to the input of the photodetector. This loss is attributed to the loss in the four connectors used, propagation loss in the optical fiber (~1 meter

in length), and the polarizer. Including the coupling alignment between the two parabolic lensed fibers (without the testing device) elevated the loss by an additional -14.44 dB, resulting to a total loss of -19.0 dB. The -14.44 dB loss is attributed to the alignment capability of our xyz stage and the reflection and scattering of light off the tip surface of the lensed fiber. The misalignment between the two fibers leads to optical mode misalignment and results in optical loss. The mode mismatch can be calculated by the overlap integral

Equation 3-3

$$\eta = \frac{|\iint G_1(x, y)G_2^*(x, y)dxdy|^2}{(\iint G_1(x, y)G_1^*(x, y)dxdy)(\iint G_2(x, y)G_2^*(x, y)dxdy)}$$

where $G_1(x, y)$ and $G_2(x, y)$ are the single mode profiles of a cylindrical optical fiber and rectangular on-chip waveguide, respectively.

Equation 3-4

$$G_1(x, y) = \exp\left(-\left(\frac{r}{w_o}\right)^2\right) = \exp\left(-\frac{x^2 + y^2}{w_o^2}\right)$$

Equation 3-5

$$G_2(x, y) = \left(\frac{2}{\pi}\right)^{0.25} \left(\frac{1}{\sqrt{W}}\right) \left(\frac{1}{\sqrt{H}}\right) \exp\left(-\frac{x^2}{W^2}\right) \exp\left(-\frac{y^2}{H^2}\right)$$

η is the coupling coefficient, w_o is the cylindrical beam waist (typically $\sim 5 \mu\text{m}$ for the lensed fibers used), and W and H are the width and height of the rectangular waveguide, respectively. Using Equation 3-3 and the dimensions of fabricated waveguide cross section, a coupling coefficient of 0.381 was obtained.

A straight, rectangular microfabricated silicon nitride waveguide was placed between the two lensed fiber to characterize the optical losses associated with the input/output facets and the propagation loss through a straight $1.0 \mu\text{m}$ wide and 400 nm thick waveguide. A total loss of -30.46 dB was observed between the laser output and the photodetector input. The additional loss of -11.46 dB is attributed to the insertion loss, coupling between lensed optical fiber and on-chip waveguide, and propagation loss.

Propagation loss can be measured empirically by using the Fabry-Perot contrast method to circumvent the inconsistency of optical alignment. This technique hinges on the property of cleaved end facets of the waveguide to act as mirrors which form a Fabry-Perot resonator. The optical transmission of such a straight waveguide of uniform propagation loss α and length L is given by

Equation 3-6

$$T(\phi) = \frac{(1-R)^2 e^{-\alpha L}}{(1-r)^2 + 4r \sin^2 \phi},$$

Where R is the facet reflectivity, $r = R e^{-\alpha L}$, and ϕ is the phase, which is varied during the measurement. Measurement of the fringe contrast K is given by

Equation 3-7

$$K = \frac{T_{max} - T_{min}}{T_{max} + T_{min}} = \frac{2r}{1 + r^2}$$

Where T_{max} and T_{min} are the maximum and minimum of the periodic optical power created by the Fabry-Perot resonance. Equation 3-7 shows no dependency on the input coupling and as a result, input coupling and alignment inconsistencies are circumvented. An approximation of the reflectivity of the end facet and a measurement of the optical spectrum of a straight waveguide can thus be used to extract the propagation loss.

The effective refractive index, n_{eff} , of the system can be derived by measuring the free spectral range (FSR) of the optical spectrum and applying it to Equation 2-3, which is reiterated here.

Equation 3-8

$$FSR_{wavelength} = \Delta\lambda = \frac{\lambda_o^2}{n_{eff}L}$$

where $\Delta\lambda$ is the wavelength distance between resonant peaks, λ_o is the resonant wavelength, L is the circumference ($2 \times radius \times \pi$) of the resonator. A measured FSR of 22.53 nm for a 19.85 μm diameter microdisk resonator, resulted in a n_{eff} of 1.710, within the expected range based on COMSOL Multiphysics simulation.

The optical spectrum of the microdisk resonator was characterized for its stability across various optical power input levels. The input optical power was sequentially varied from 1 mW to 7 mW.

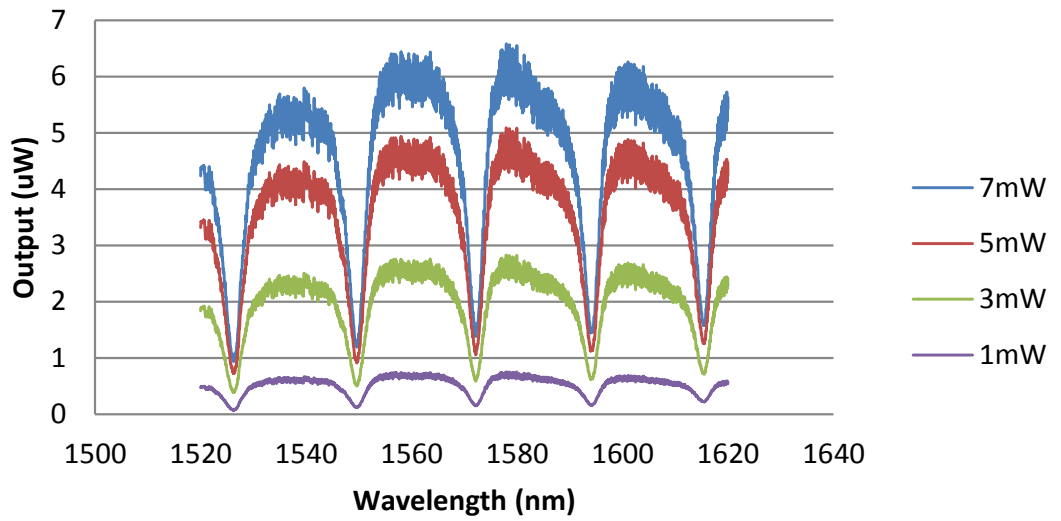


Figure 3-17 Graph showing the optical spectrum of a disk resonator at different input optical power intensities

Fitted resonant wavelengths resulted in a standard deviation of 2.11 pm. The stability of the resonator performance was monitored for 72 continuous hours, resulting in a fitted resonant wavelength standard deviation of 5.63 pm. The collected output power drifted over time during the continuous monitoring period. This was caused by mechanical relaxation of the xyz-stages, which led to miscoupling between the lensed fiber and the on-chip waveguide. In accordance with the power modulation characterization, the resonant wavelength stayed relatively constant with the change in optical coupling.

The minimum detectable wavelength shift of the sensor system is therefore 16.89 pm, three times the standard deviation of the resonant wavelength over a standard sensing experiment period. This corresponds to a minimum detectable effective refractive index shift of 1.59×10^{-5} RIU, which will be the key limitation to the dynamic range of the sensor system.

Based on characterizations conducted on the testing setup and the optical resonator, the stability and the minimum detectable RIU of the system have met the need of the transduction mechanism for the proof of concept demonstration of the specified sensing application. Future fabrication and system optimization that can be pursued to further increase the sensitivity and the dynamic range of this optical sensor system will be detailed in Chapter 6.

Chapter 4. Nanostructured Bioreceptor Layer

The receptor layer is responsible for the selectivity of a sensor system. A biological nanostructured receptor layer offers two main advantages: (1) the diversity and the programmability of biomolecules, which enable the highly selective recognition of analyte and (2) the high surface area and binding site density provided by nanostructured materials. If nanostructured bioreceptor layers can be successfully integrated within sensor systems, this would provide the selectivity sought by many sensor systems under development. This chapter will describe the synthesis of two

nanostructured receptor layers, the *Tobacco mosaic virus* (TMV) and the *Tobacco mosaic virus-like particles* (VLP).

4.1 Tobacco mosaic virus

The *Tobacco mosaic virus* is a highly infectious filamentous plant virus that is inert to humans. The TMV virion is a rigid rod consisting of ca. 2,130 identical coat protein (CP) subunits stacked in a helix around a single strand of RNA, leaving a 4 nm diameter channel through the 300 nm long virion axis. The encapsulated genomic RNA limits the length of the virus rod, terminating at the 3' and 5' ends. The molecular weight of each coat protein unit is 17.5 kDa and it self-assembles into a helical structure with a pitch of 23 Å with $16 \frac{1}{3}$ coat proteins per turn around the RNA. Each CP molecule of a wild type TMV is composed of a folded chain of 158 amino acids, with two termini (see Figure 4-1). The inner surface of the CP molecule lines the inner channel of the TMV structure; the outer radius of the CP molecule lines the outer surface of the virion, displaying both termini (N and C) of the amino acid chain.

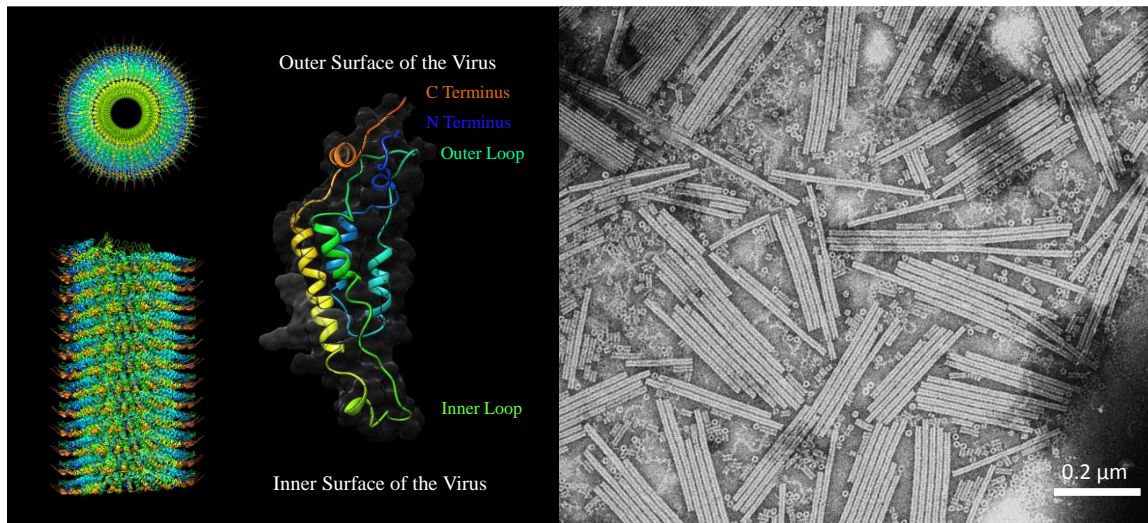


Figure 4-1 (Left) Diagram showing the structural composition of a TMV and one of its coat proteins. The top and side perspectives of the virus model show a helical tube viral structure. (Right) A TEM image showing TMV rods.

Stability of the TMV nanostructure is governed by the repulsive carboxylate groups located on opposite sides of coat protein subunits. The negatively charged carboxylates are stabilized by protons and the Ca^{++} ions that regulate the stability of the interrelationship between coat protein subunits to form a helical structure.

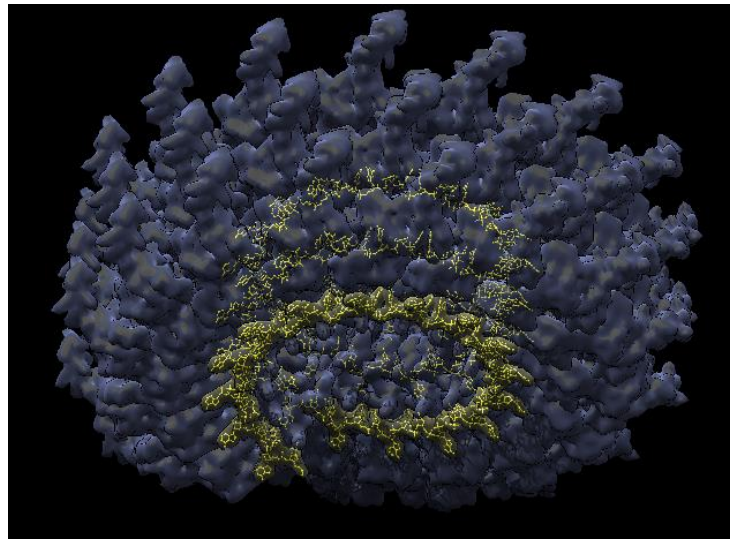


Figure 4-2 A model diagram showing the location of the coat protein binding to the RNA forming helical disks

Below is a summary of TMV properties that are beneficial for its integration with microsensor systems:

1. Well studied three-dimensional structure of TMV [152-155]
2. A wealth of biophysical information on the self-assembly characteristics of TMV [156];
3. The availability of a full-length infectious cDNA clone of the virus that allows the creation of novel virus structures and surfaces via established genetic mutations [157, 158];
4. A wide range of existing coat protein variants with diverse assembly properties [159]

5. Wild type TMV structure is very robust, surviving in pH levels 2-11 and temperature up to 60°C [122]
6. A large number of coat proteins to display and support binding sites
7. The ability to easily purify large quantities of virus and coat protein from infected plants
8. Previous demonstration of cysteine conjugation to allow for the self-assembly of TMV on the surface of microfabricated structures [160-164]

All the work associated with the synthesis and purification was done in collaboration with Dr. James Culver's laboratory in the Institute for Bioscience and Biotechnology Research.

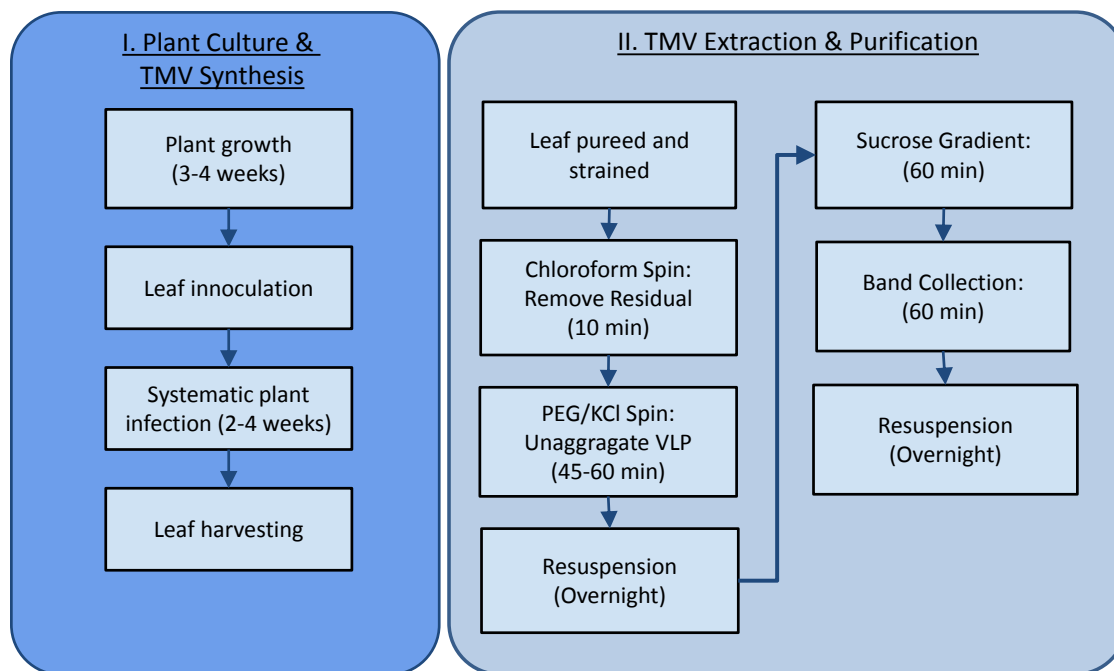


Figure 4-3 Block diagram showing the process flow of TMV synthesis and purification

4.1.2 Synthesis of TMV-n1Cys and TMV1Cys-TNT

The availability of a full-length complementary cDNA clone of the TMV genome and the well-studied structure of the coat protein and its architecture of assembly allows for specific targeted genetic alteration of the virion surface properties. Coat protein modifications are made by inserting or modifying amino acids sequences, typically 1 to 20 amino acids in length, using overlap-extension polymerase chain reaction (PCR). Potential locations for desired modifications include both the N and C termini of the coat protein will be repeatedly expressed on the external surface of the

assembled virion. The TMV virion outer surface properties were specifically functionalized based on this method. The display of a cysteine residue on the N terminus (*n1Cys*) and a TNT-specific peptide (WHWQRPLMPVSI) conjugation on the C terminus (*cTNTbp*) were expressed on the virion's outer surface.

Wild type and modified TMV are generated in large quantities by inoculation of tobacco cultivars such as *Nicotiana benthamiana* or *Nicotiana tabaccum* cv Xanthi. The plant leaves' surface is abrasively rubbed to allow the plant tissues to be vulnerable to infection. For wild type or other pre-existing stable TMV mutants (such as TMV-*n1Cys*) the plants are infected directly from existing virus stock solutions or infected plant tissues. Viruses that have been more extensively altered in a way that causes attenuation of amplification *in vivo*, such as TMV1Cys-TNT, have a greater chance of eventually being outnumbered by viruses originating from a spontaneous reversion to wild-type-like genotype (e.g. a mutation that causes premature termination of the coat protein translation), if they are produced by multiple generations of inoculation and purification. In these cases, plants were directly infected with RNA transcripts of the cDNA.

Nicotiana benthamiana plants were typically infected with TMV1Cys-TNT RNA transcripts due to their relatively weaker immune system, less likely to cause spontaneous reversion. *Nicotiana tabaccum* cv Xanthi are larger plants that have a stronger immune system and were used to infect the more stable wild type and TMV-

n1Cys viruses. The larger Xanthi produced a larger yield of the TMV solution without any significant spontaneous reversions.



Figure 4-4 Picture of *Benthamiana* ready for inoculation

The plants were grown in LCI Potting mixture (SunGro Inc., Bellevue, WA) in 4 inch pots. They were maintained under growth chambers at 28 °C with a 12 hour light/dark cycle. Plants were typically inoculated 4 weeks after transplanting their respective germinated seedling into pots. Leaves showed signs of infection when mosaic patterns appeared on their blades. Leaves were then collected after observing systematic infection throughout the plant, typically 2-4 weeks post-inoculation.

Large peptide modifications to the CP, such as TMV1Cys-TNT, may cause failure of CPs to form into a helical structure due to steric hindrance on the exterior

surface. As a result, a flexible linker was inserted before the large peptide to alleviate some of the steric hindrance. An additional approach to reduce this hindrance was to conjugate the peptide modification to the C terminus of the coat protein via an amber stop codon (Figure 3) [165]. The amber stop codon permits read-through and expression of the peptide encoding sequence in less than half of the CPs. Thus, both the unmodified and peptide modified CP subunits are produced during infection, resulting in virus particles that contain a mixture of the two CPs (Figure 3). Using this genetic control mechanism we can modulate the number of peptides present on a virus particle as means to vary the availability of target analyte binding sites and to relax the peptide steric hindrance during helical formation.

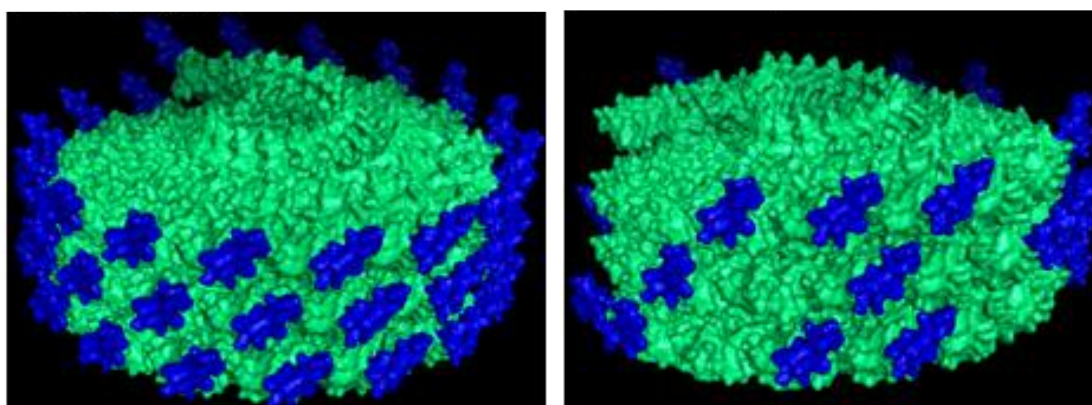


Figure 4-5 Model diagrams of (right) TMV fully expressing conjugations on each of its coat proteins and (left) TMV modulated expression of conjugations on its coat proteins due to the insertion of amber stop codon

4.1.3 Purification of TMV

Once the infected leaves are harvested, they can be immediately processed for TMV extraction and purifications or be frozen at -20°C and stored for extraction at a later date.

The purification process for TMV starts by blending the harvested leaves until smooth using virus extraction buffer made fresh just prior to use. The blended solution is then strained and the extract is collected. The filtered extract is further purified by adding chloroform (typically 10% of final volume) to remove organic soluble compounds from the solution, such as plant pigments and cell tissues, by centrifugation (17,000 g at 4 °C for 10 minutes). Polyethylene glycol 8000 (6 % w/v) and KCl/NaCl (1.5% w/v) are added to the supernatant to precipitate and collect the nanorods by centrifugation (17,000 g at 4 °C for 10 minutes). After the resuspension of the pellet in 0.1M (pH 7) phosphate buffer, the solution can be further purified by centrifuging. The resuspended PEG virus pellet is centrifuged (91,000 g at 14 °C for 2 hours) through a sucrose gradient (25% w/v) and then the translucent band, which matches the virus density, is collected using a syringe. A high purity virus pellet can be finally retrieved following a final centrifuge pelleting step (92,000 g at 4 °C for 2 hours) after the supernatant is poured off. The pellet is gently resuspended in 0.2 – 1.0 mL phosphate buffer overnight at 4 °C. A more detailed description of the purification steps can be found in the Appendix C and [166].

TMV and their derivatives are generally stored in 0.1 M pH 7 phosphate buffer solutions at -15 °C. Viruses can also be resuspended in or dialyzed [167] with deionized water. An in depth study on the lifetime and long term reliability of TMV storage has not been directly researched. However, TMV's structure and functionality can be preserved for at least 6 months in ideal storage conditions. Repetition of thawing and refreezing of the sample should be kept to a minimum as that can decrease the lifetime of the solution.

4.1.4 Analysis of TMV

Virus concentrations are determined by measuring absorbance (OD) at 260 nm, correcting for light scattering at 325 nm [168]. The typical TMV- *n*1Cys concentration resulting from a 100 g batch of leaves was 1-3 mg/mL for every milliliter yielded. The yield of TMV1Cys-TNT varied greatly from 0 – 0.2 mg/mL. The homogeneity of the TMV1Cys-TNT varied greatly as well due to its likelihood of reversion to TMV- *n*1Cys.

To verify the synthesis and purification of the TMV, samples were imaged under Transmission Electron Microscope (TEM) at The Laboratory for Biological Ultrastructure operated by collaborator Mr. Adam Brown (see Figure 4-6). Visualizing rod like structures confirmed the synthesis of CPs and the formation of the nano-rods.

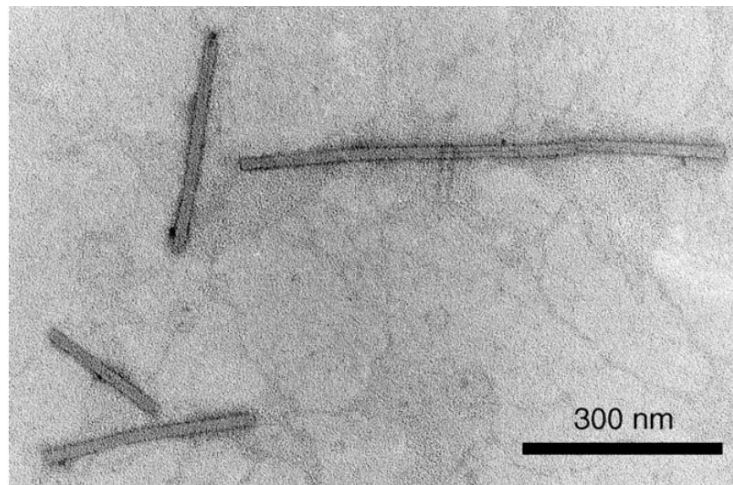


Figure 4-6 TEM image of purified TMV

To ensure that the TMV retained its genetic modifications, analysis techniques such as gel electrophoresis, Western blot, and mass spectrometry are used to verify the structure size, functionality, and sequence of the purified virus structures.

Gel electrophoresis

Gel electrophoresis is a macromolecule sample separation method based on their difference of mobility, dependent on their size and charge, as they travel through a conductive gel. Particles with similar size and charge will travel in bands through the gel. RNA gel electrophoresis (1% w/v agarose gel) was used to monitor the presence and size of the single strand RNA. Protein gel electrophoresis (15% w/v acrylamide) was also used to monitor the presence and size of CPs. The size of the TMV1Cys-TNT RNA and its CPs were compared to that of known TMV-*n*1Cys RNA and CPs,

respectively. The additional peptide (*c*TNTbp) causes an increase in length of RNA and size of CPs and shifts the band of the gel electrophoresis. CPs conjugated with the leaky stop codon, which allows the expression of the peptide only on a fraction of the CPs, displayed two bands in the protein gel electrophoresis, showing the separation between the larger expressed and smaller suppressed *c*TNTbp on its CPs.

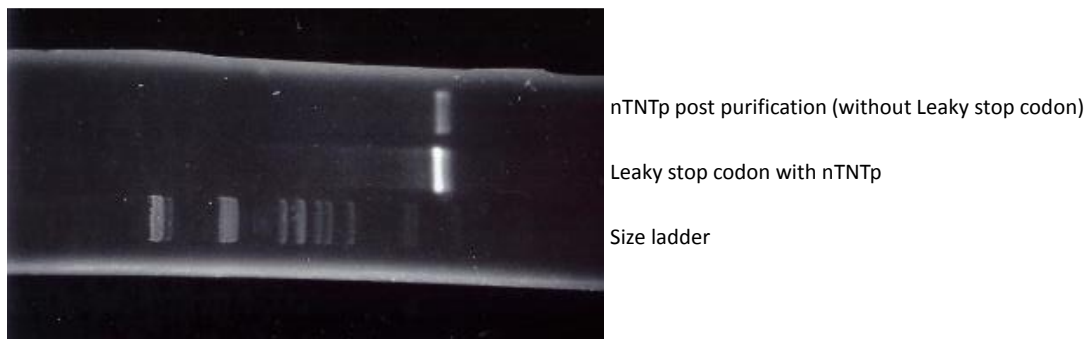
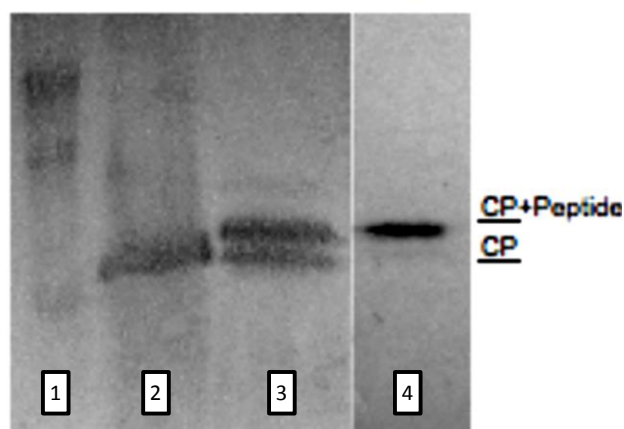


Figure 4-7 Image of gel electrophoresis showing the presence of *n*TNTbp conjugation with and without leaky stop codon

Western Blot

Western blot, also known as protein immunoblot, is an analytic technique to detect the presence of a specific protein in a sample. This technique is more functionally specific because it employs binding affinity of antibodies and is visually more sensitive than gel electrophoresis. This technique employs the protein separation from the protein gel electrophoresis and conducts enzyme-linked immunosorbent assay on a nitrocellulose membrane. The presence of TMV CPs on the membrane can be

visualized by exposing the coat proteins to a selective antibody with color changing enzymes. The appearance of a blue violet hue after the substrate assembly indicates the attachment of the selective antibody and the presence of TMV CPs, see Figure 4-8. For a detailed protocol of the Western Blot process, please see Appendix C.



1. Size ladder
2. Unmodified coat protein only
3. Leaky stop codon with TNT-peptide coat protein
4. TNT-peptide coat protein only

Figure 4-8. Image courtesy of Dr. Culver showing a Western blot of TMV1Cys-TNT with and without leaky stop codon in reference to unmodified coat proteins

4.1.5 Discussion

The synthesis and purification of TMV structures is a long series of processes that need to be developed and optimized. The process developments were initially conducted by Dr. Culver's group for the synthesis and purification of TMV-*n*1Cys. The

standard protocol for TMV-*n1Cys* synthesis and purification were reliable and consistent, resulting in a consistent supply of TMV-*n1Cys*.

However, these process protocols have proven to be very coat protein modification dependent. When the protocol was transferred to synthesizing and purifying TMV1Cys-TNT, the end yield was dramatically lower and less consistent compared to that of TMV-*n1Cys*. Most of the development time was dedicated to improving the yield of TMV1Cys-TNT. The time required for the plant growth and the systematic infection inhibited quick optimization iterations. Consequently, long periods of time were lost waiting for the result of each iteration. When the purification process resulted in low or no yield, it was often difficult to pin point the cause — lack of systematic infection or lost in the purification process — of the decreased yield. As a result, many parallel batches of plant growth and purification process were conducted for redundancy purposes. A purification resulting in purified viruses did not guarantee that the coat proteins were of the correct modification. Leaves that were inoculated with TMV1Cys-TNT had a high chance of reverting back to wild-type TMV or TMV-*n1Cys*. The retention of the *cTNTbp* peptide was confirmed only post-purification when virus samples were analyzed using mass spectrometry.

This process protocol ultimately yielded sufficient samples for subsequent integration and sensing experiments, detailed in the following chapters. There was a

clear need to develop a bio-nanostructure with a shorter synthesis period which would allow faster iteration sequences and a shorter development period.

4.2 Virus-like-Particles

To address the challenges faced by TMV1Cys-TNT and similar constructs, Dr. Culver's lab modified the TMV coat protein genetically and structurally to produce a nano-rod that is expressed and self-assembled in bacteria. This system allows the modification of the viral coat protein in the absence of virus replication and enables production of virus-like particles (VLPs) directly in bacteria, thereby avoiding problems associated with recombination and construct instability and decrease the synthesis period to 48 hrs.

The stability of the VLP is governed by the same repulsive carboxylate groups of TMV, as previously described in Section 4.1. The third axial carboxylate interaction that significantly drives the particle assembly occurs between the residues E50 and D77. The mutations of E50Q and D77N have been shown to block virus disassembly even in the absence of the nucleic acid backbone. As a result, our collaborators have exploited this finding to carry out the E50Q and D77N modifications in the TMV coat protein open reading frame and optimize for expression in *E. coli* bacterial cells. This modification has helped to realize a VLP structure consisting of self-assembled TMV CPs but without the necessity for the CPs to bind to a viral nucleic backbone. The

nucleic backbone dedicated the length of the virion's helical structure. Due to the absence of this limitation, the length of VLP nano-rods has a higher variation. Their inner and outer diameters remain similar to that of the TMV dimension.

Further modifications to the N- and C- terminus of the coat protein were achieved by primer based PCR mutagenesis, identical to that of the TMV coat protein modification. Similar to that of TMV-*n1Cys*, a cysteine codon was added at position two of the N-terminus of the coat protein ORF to produce VLP-*n1Cys*, resulting in enhanced binding affinity to substrate surfaces. Sequences encoding the binding peptides for FLAG epitope (DYKDDDDK) were added to the C-terminus of the coat protein ORF, producing TMV1Cys-VLP-FLAG. This binding peptide expression allows for the specific recognition of FLAG antibodies.

All the work associated with the synthesis and purification of VLPs was done in collaboration with Dr. James Culver's laboratory in the Institute for Bioscience and Biotechnology Research as well. Dr. Culver's group developed all VLP constructs created in *E. Coli* DH5 alpha cells and then expressed in either BL21 or JM109 bacterial cells. The initial protocols developed by the Culver group were modified as shown below in this research.

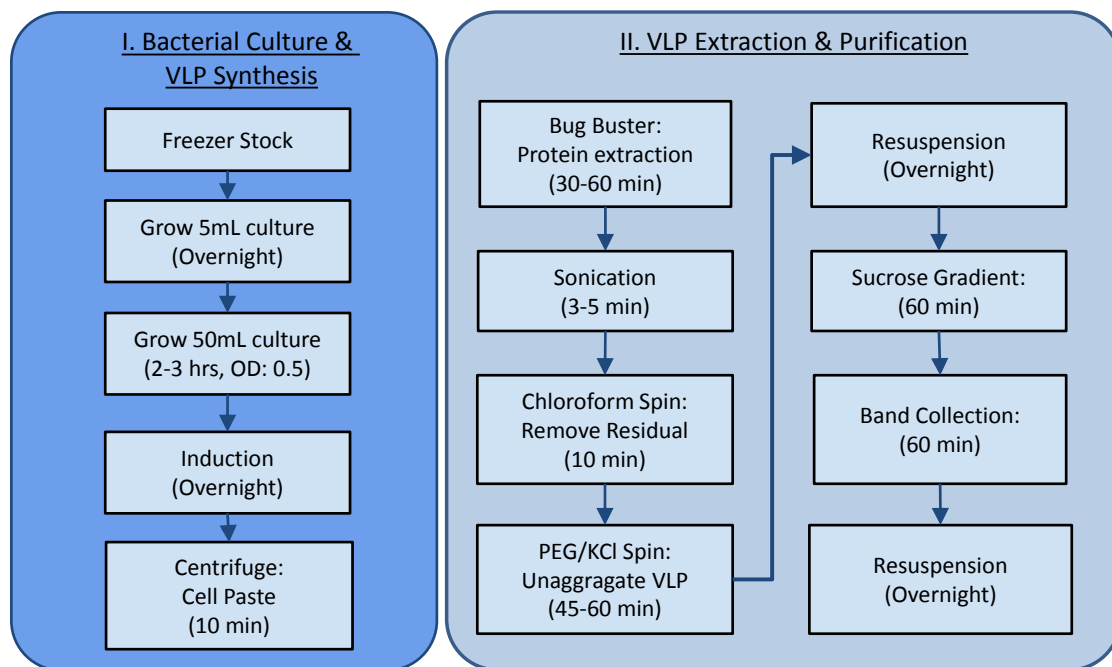


Figure 4-9 Diagram showing the process flow of the synthesis and purification of TMV1Cys-VLP-FLAG.

4.2.1 Bacterial Culture and Synthesis of TMV1Cys-VLP-FLAG

To obtain a purified solution of TMV1Cys-VLP-FLAG, a new batch of bacterial cells need to be first cultured from a small sample of BL21 freezer samples whose bacterial cells already contain TMV1Cys-VLP-FLAG vectors (a RNA molecule that contains the CP sequence). The freezer sample is placed in a test tube with 5 mL of Lysogeny broth (LB) media with antibiotics (ampicillin (100 $\mu\text{g/mL}$) and chloramphenicol (50 $\mu\text{g/mL}$)) and cultured on a shaker in an incubator overnight at 37 $^{\circ}\text{C}$.

The bacterial culture was then scaled up to a 50 mL LB media solution and incubated on a shaker at 37°C until Optical Density (OD) reading reaches 0.5 at $\lambda = 600$ nm.

The bacteria were induced once the OD was reached. The bacteria were induced by adding 0.1% v/v 1 M Isopropyl β -D-1-thiogalactopyranoside (IPTG) to trigger the formation of proteins by reading preprogrammed vectors inside the bacteria. The bacterial culture solution was induced overnight on a shaker at 25°C. CPs form and then self-assemble into helical nano-rods in the bacterial cells by the following morning.

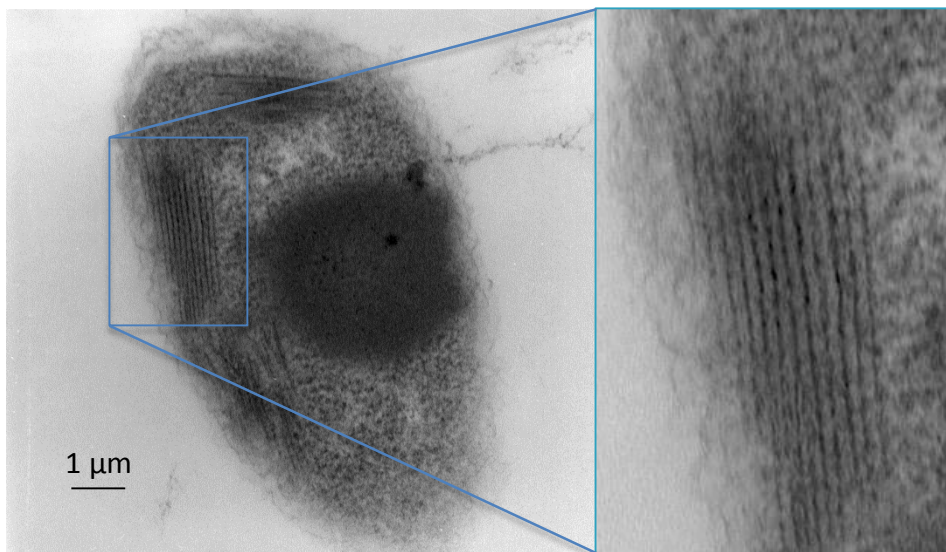


Figure 4-10 A TEM image, courtesy of Dr. Culver, showing the formation of VLP nanorods in bacterial cells

A more detailed protocol on the synthesis of VLPs can be found in Appendix C.

4.2.2 Extraction and Purification of TMV1Cys-VLP-FLAG

The purification of VLPs is similar to that of TMV. Induced cells were harvested by centrifugation at 4°C from the LB media. The cell pastes were lysed using Bugbuster™ with Lysonase™ according to the manufacturer's protocol (Novagen, Madison WI) to free the VLPs in solution. 0.5 mM Dithiothreitol (DTT) was added to the cell lysates to deter disulfide bond formation between two VLP structures leading to clusters and bundles of VLPs. This is then followed by a 3-5 min sonication to break up any existing bundle formation. Chloroform (33% v/v) was then added and mixed to the lysates, to extract cell tissues left in the solution. Chloroform was separated by centrifugation for 10 min at $17,000 \times g$ at 4 °C. To precipitate VLPs, 1.5% KCl and 6% polyethylene glycol by weight were added to the suspension and mixed for one hour at 4 °C. VLPs were then pelleted by centrifugation for 10 min at $17,000 \times g$ at 4°C. The resulting pellet was resuspended by shaking overnight in 0.5 to 2 mL of 0.1 M pH 7 sodium phosphate buffer. To further purify the resuspended VLP, a sucrose gradient is used to filter the suspension by density. The VLP pellets were loaded onto a 25% w/v sucrose gradient in 0.1 M pH 7 sodium phosphate buffer and centrifuged for 30 min at $91,000 \times g$ at 14 °C. A diffuse band in the sucrose gradient corresponding to

the purified VLP was isolated was removed by syringe. This band was diluted with 0.1 M pH 7 sodium phosphate buffer and then centrifuged for 45 – 60 min at $92,000 \times g$ at 4 °C. The purified VLP pellet was then resuspended in 0.1 M pH 7 sodium phosphate buffer and ready for use. Typical VLP-*n1Cys* and TMV1Cys-VLP-FLAG constructs resulted in purified solutions of 0.5-2.5 mg/mL in concentration and up to 1.5 mL in quantity.

From the start of the bacteria culturing to the purified VLP pellet resuspension, the entire process takes less than four days.

The purified solution was image under TEM (Figure 4-11) and showed nano-rod structures very similar to that of purified TMV structures. The variation in the length of the rods was expected. Recent work by our collaborators has shown that the length of the rod can be controlled by modifying the pH level of the solution, controlling the protonation level between coat proteins.

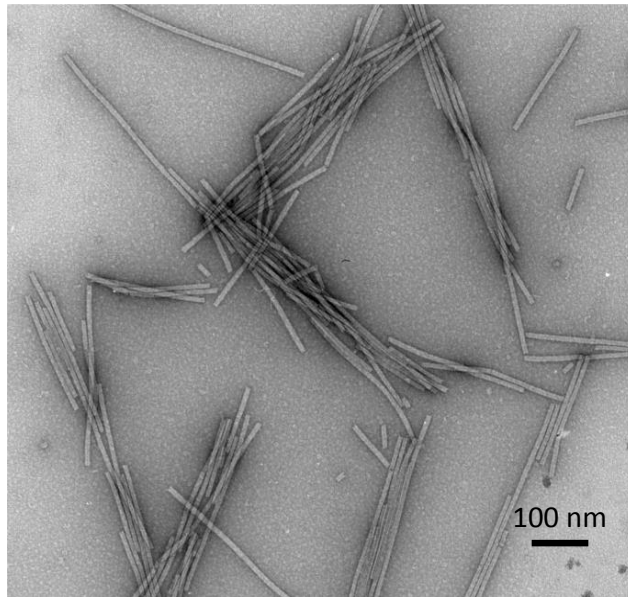


Figure 4-11 A TEM image, courtesy of Dr. Culver, showing VLPs after purification process

Gel electrophoresis and western blot of TMV1Cys-VLP-FLAG samples were conducted to verify their coat proteins against those of VLP-*n*1Cys. The columns confirmed the size of the TMV1Cys-VLP-FLAG coat proteins, matching very similarly to those of VLP-*n*1Cys.

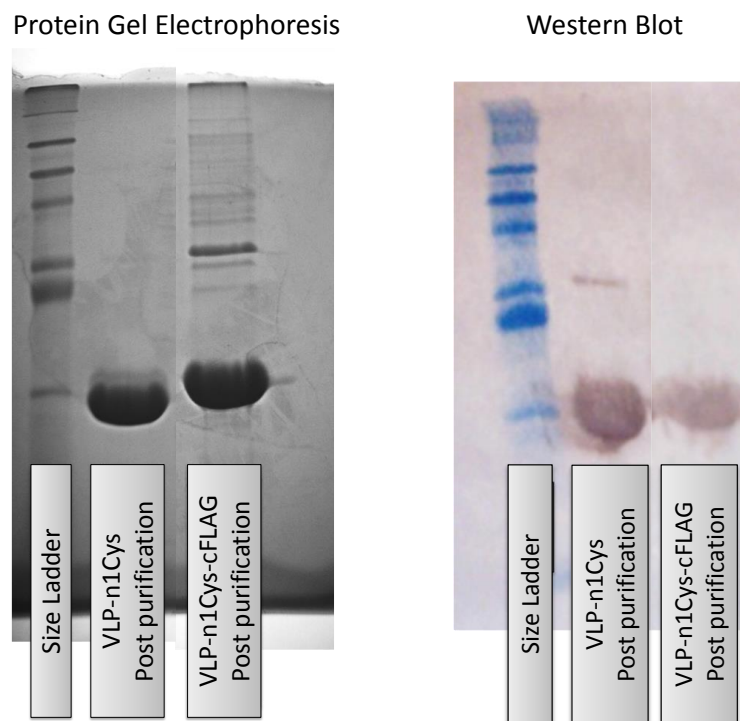


Figure 4-12 Pictures of gel electrophoresis and Western Blot results showing the successful purification of VLP-*n1Cys* and TMV1Cys-VLP-FLAG

4.2.3 Discussion

The reduced time needed to synthesize and purify various constructs of VLP enabled a shorter iteration time to develop and optimize the process. The final protocol reduced the synthesis and purification period from up to 12 weeks down to four days. Furthermore, bacterial cell replication ensures the construct stability. Unlike TMV1Cys-TNT, where reversion to TMV-*n1Cys* was a difficult issue to overcome, TMV1Cys-VLP-FLAG constructs consistently produced the expected mutation.

Similarly, other modified constructs can be synthesized using the VLP scaffold. Parallel work is focused on modifying the VLP with a TNT specific peptide. Initial results demonstrate successful extractions with concentrations up to 3.0 mg/mL. Further optimization is required to further increase its yield and purity of the solution.

The quantity of purified VLPs available for use is limited by the logistics and cost of the purification process rather than the process yield. The established protocol was aimed at small volume quantity purification. However, large quantities protein purification for production purposes has previously been demonstrated and can be similarly applied to VLP purification if needed.

Finally, the successful synthesis and purification of TMV1Cys-TNT and TMV1Cys-VLP-FLAG allows for the subsequent development and characterization of the integration of these bio-nanostructures with microfabrication and microstructures.

Chapter 5. Integration of Bioreceptors with Microfabricated Structures

The integration of biological molecules with semiconductors is often challenging due to the incompatibility between the two very different materials groups. Biological molecules are usually highly sensitive to harsh environments and incapable to tolerate extreme pH levels or temperatures. While they have innate high binding affinity, they can also be denatured by various solutions, such as alcohol, solvents, and solutions with extreme pH levels.

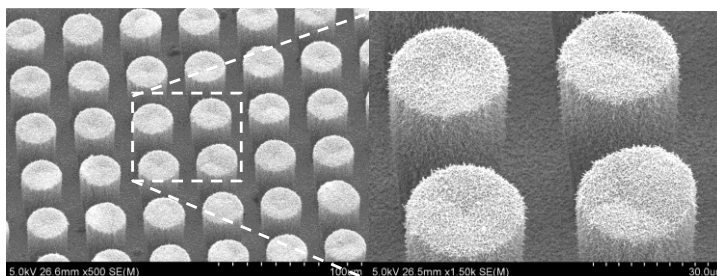
A bioreceptor that is compatible with semiconductors and their fabrication techniques is advantageous because the combination of the two can yield the high sensitivity provided by microtransducers and the high selectivity provided by biomolecules. Microsystems that leverage the affinity of bioprobes or bioreceptor layers have been extensively used as described in Chapter 1. Fabrication processes have been design to circumvent the issue of incompatibility by reserving the integration of biomolecules with the semiconductor system for the last process step. This is typically a suitable solution, but for applications that require processing after the biomolecule assembly, a fabrication challenge remains.

Tobacco mosaic virus (TMV) and *Virus-Like-Particles* (VLP) are good candidates for integration with microfabrication processes because of their structural stability. Wild type TMV can survive in a wide range of pH levels, temperatures, and solvent-water mixtures [122]. In this chapter, our efforts to integrate TMV and VLP with microfabrication processes is targeted towards the realization of a microsensor system.

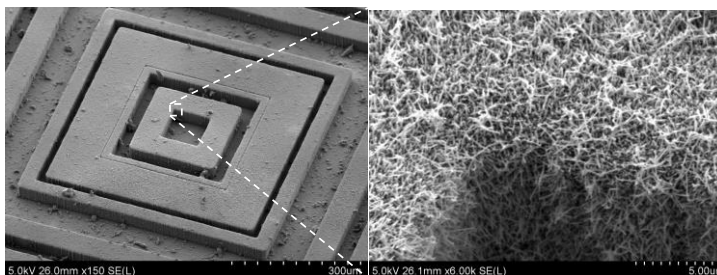
5.1 Self-Assembly of Bio-Nanostructures

The conjugation of the cysteine residue (*n*1Cys) on the outer surface of TMV has previously been demonstrated through the self-assembly of this complex onto 3D microfabricated structures from high aspect ratio pillars [169-171] to hollow cylinders can be assembled on a wide range of material surfaces, including semiconductors (i.e. Si, InP), dielectrics (i.e. Si₃N₄), polymers (i.e. Photoresists), and metals (i.e. Cu, Au), using a TMV-*n*1Cys concentration of 0.1 – 0.2 mg/mL.

***Assembly on Au
Microstructures***



***Assembly on SU-8
Microstructures***



***Assembly on Si
Microstructures***

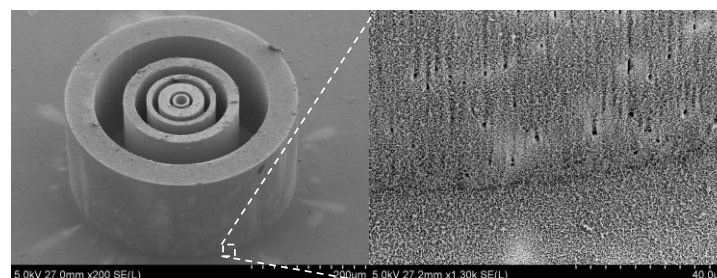


Figure 5-1 SEM images showing TMV-*n*1Cys self-assembled on a wide range of materials and microfabricated structures

Based on these precedents, we utilized TMV-*n*1Cys and VLP-*n*1Cys to coat the surface of microfabricated optical devices. To image the assembly of these bio-nanostructures under Scanning Electron Microscopy (SEM), they require a layer of metal coating. The cysteine residues were used as nucleation sites for palladium (Pd) electroless plating, leading to the formation of Pd nanoparticles on the surface of the

TMV-*n*1Cys or VLP-*n*1Cys. Pd nanoparticles act as nucleation sites for the electroless plating of Ni. Submerging the chip in Ni plating solution, the surface is plated with a thin layer of Ni, making the surface conductive and visually dark (see Figure 5-2).

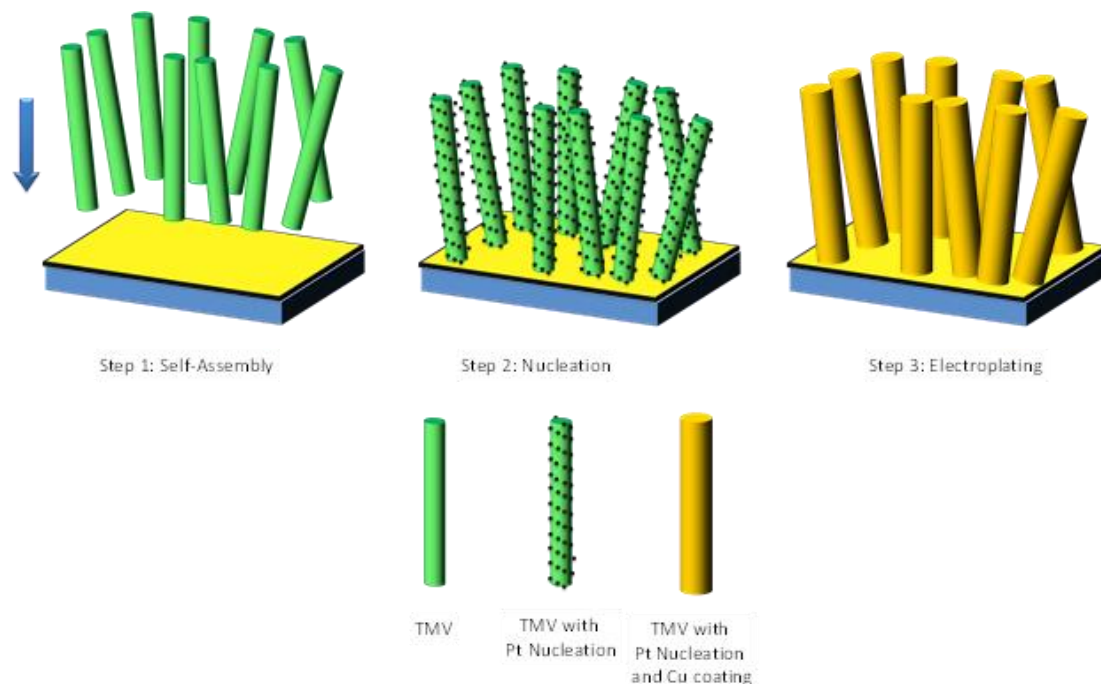


Figure 5-2 Diagram showing the self-assembly and metallization of TMV in three sequential steps. (Step 1) Self-assembly of TMV on substrate, (Step 2) Palladium nucleation on assembled TMV, and (Step 3) electroplating of Ni to conformally coat TMV rods.

Samples coated with metal were imaged using SEM, which illustrates a dense covering of TMV and VLP structures. Nanostructures conformally coated the sidewalls

of microfabricated structures even between gaps less than 1 μm in width (Figure 5-3). The TMV-*n*1Cys and VLP-*n*1Cys structures were generally assembled perpendicular to the surface. This orientation of nanostructure assembly could only be preserved when the substrate was kept wet and underwent metal coating for structural support.

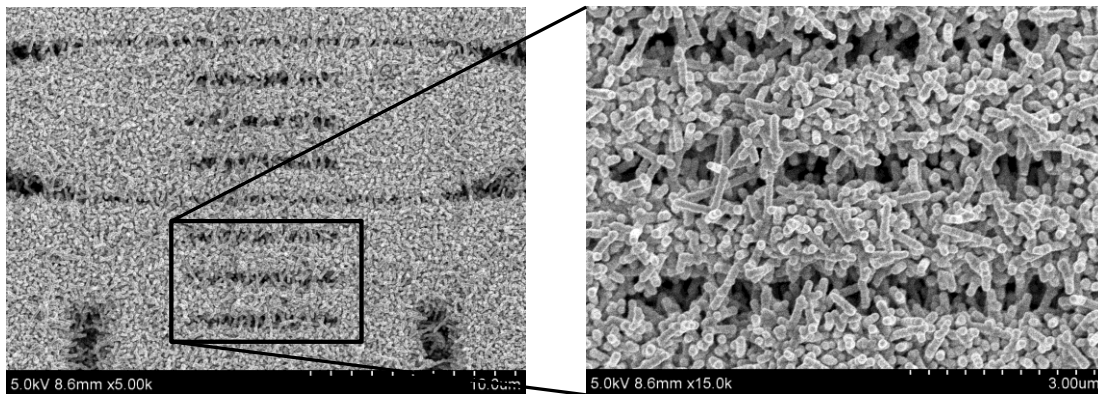


Figure 5-3 SEM images showing TMV assembly on microfabricated optical devices. TMV can be seen in sub-micron wide trenches.

If the chip was dried without the metal layer support, the bio-nanoparticles laid horizontally on the surface due to surface tension during the drying process. This was verified when a dried sample without the Pd/Ni metal coatings was imaged using Atomic Force Microscopy (AFM). A Veeco Dimension 3000 Atomic Force Microscope was used in tapping mode to scan the surface of the sample under dry condition. The AFM image showed that the dried nanorods lay on top of each other flat on the substrate surface, (Figure 5-4).

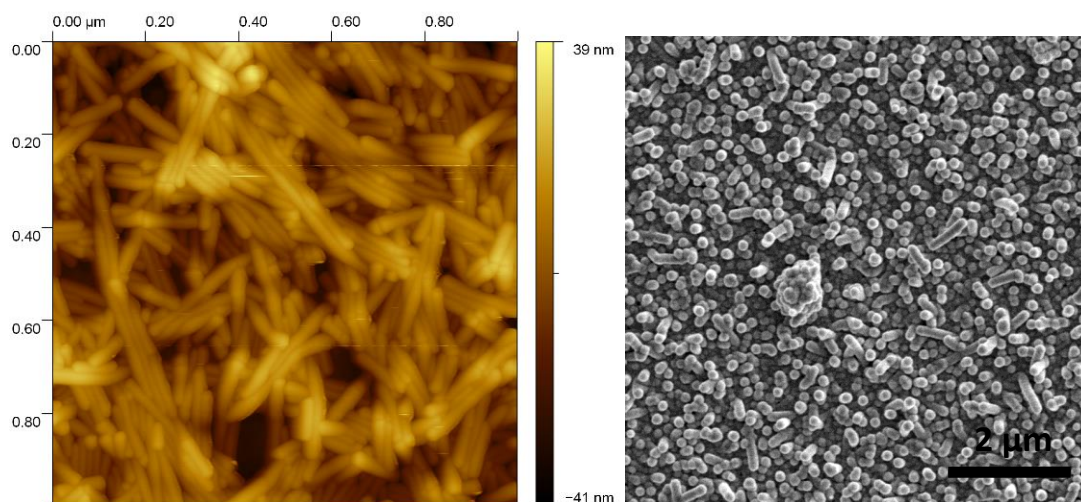


Figure 5-4 (Left) An AFM image showing a densely covered TMV-*n1Cys* assembly after dehydration. (Right) A SEM image showing metallized TMV-*n1Cys* assembled on a Au coated substrate.

Utilizing the same protocol, TMV1Cys-TNT and TMV1Cys-VLP-FLAG were assembled on gold surfaces and microdisk resonators, respectively (Figure 5-5 and Figure 5-6). From the AFM images, a more sparse coating of the TMV1Cys-TNT and TMV1Cys-VLP-FLAG than TMV-*n1Cys* can be observed. The decrease in the assembly density could be attributed to conjugating the C-terminus of the TMV and VLP coat proteins with a peptide residue and adding a second functionality on the surface of the nanorod. The secondary conjugation seemed to have a negative impact on the self-assembly properties of the nanorod. The decreased assembly may be caused by hindrance from the peptide or decrease in nanorod purification yield and or quality.

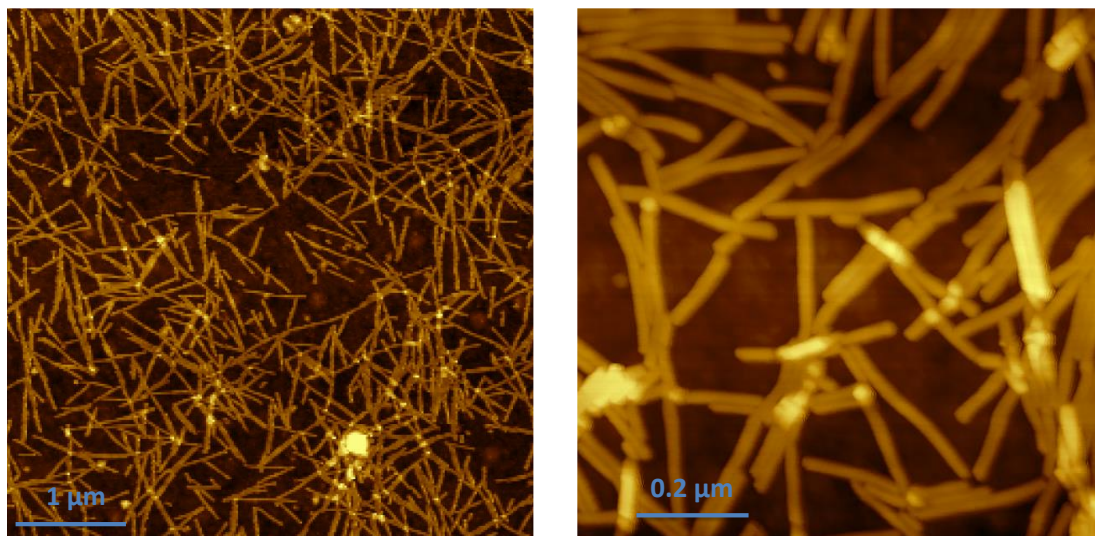


Figure 5-5 AFM images showing the assembly of (left) TMV1Cys-TNT and (right) TMV1Cys-VLP-FLAG on Au coated substrates

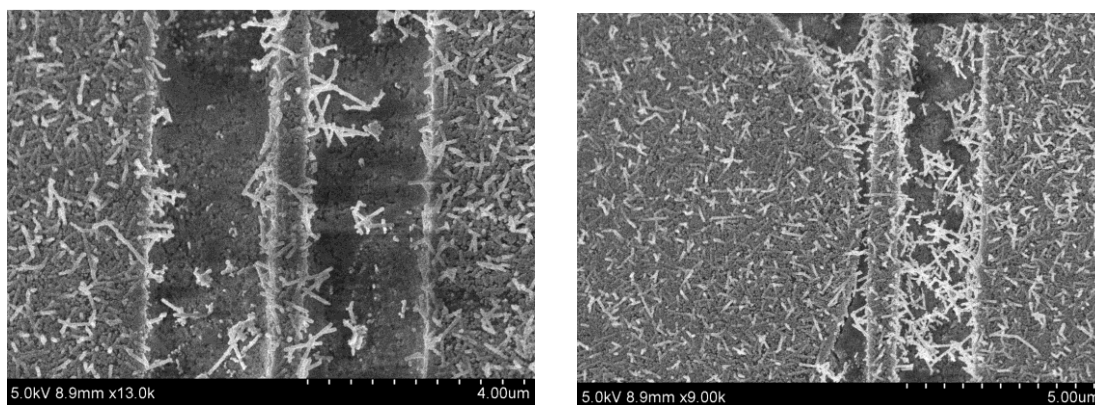


Figure 5-6 SEM images showing the assembly of TMV1Cys-VLP-FLAG on an optical waveguide and a microdisk resonator

5.2 Patterning of Bio-nanostructures

Patterning of the bio-nanostructures would enable their selective attachment on particular surfaces and potentially enable their immobilization on different locations of the sensor chip. The selective placement of biomolecules can isolate the effects of the nanostructure assembly on the system, potentially decreasing energy loss or parasitic effects, and increasing the performance of the platform. Patterning of the bio-nanostructures can also enable multi-sensor array design on a single chip by immobilizing particles with different affinity on various active device surfaces.

Microfabrication patterning typically originates from photolithography, which uses UV light to create patterns on a substrate. However, this process requires organic solvents or strong bases to develop the pattern, neither of which typically compatible with biomolecules. In collaboration with colleague Dr. Konstantinos Gerasopoulos, lift-off patterning processes were developed to allow the patterning of TMV and VLP bio-nanostructures on microdevices, as shown in Figure 5-7.

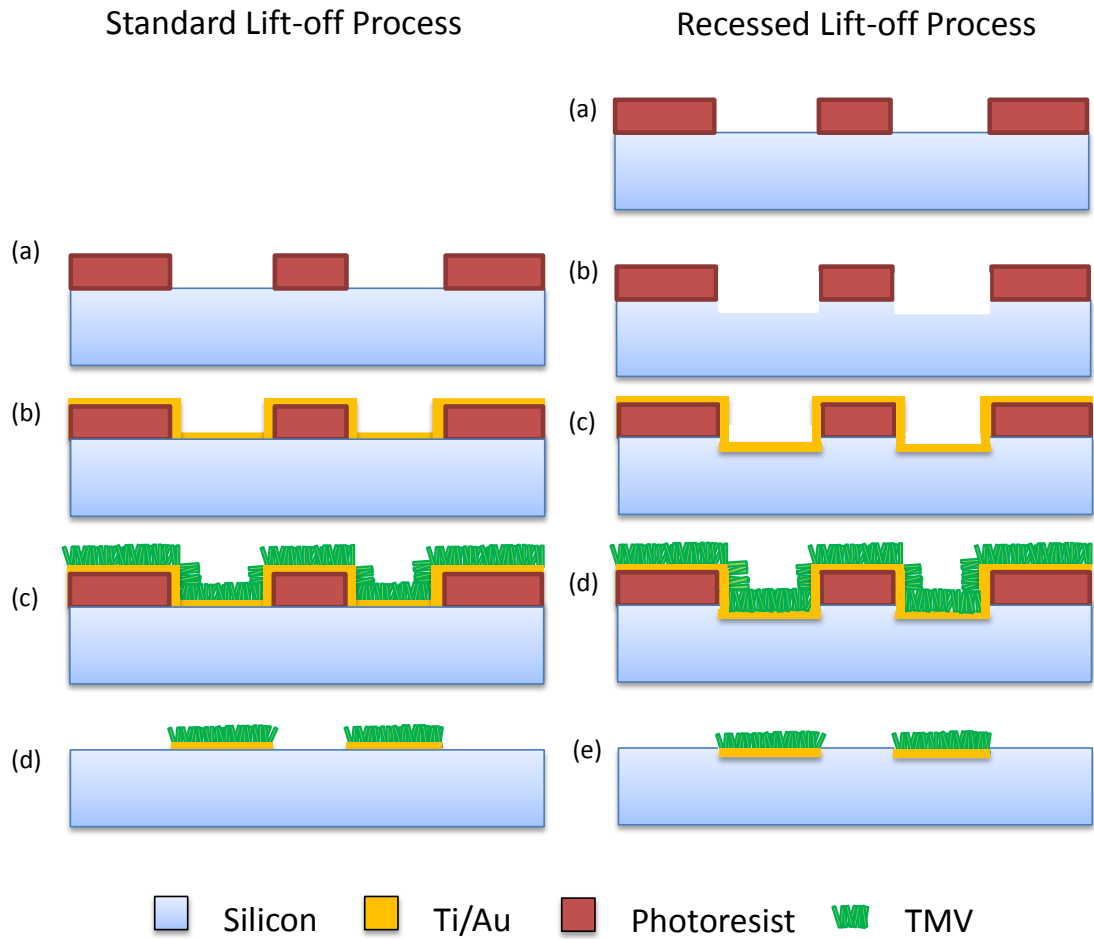


Figure 5-7 Process flow of two lift-off processes to pattern self-assembled TMV

Two different lift-off processes were developed: (1) standard lift-off process and (2) recessed lift-off process. A lift-off process utilizes a patterned photoresist layer as a sacrificial layer in order to release, or lift-off, the layer on top of the photoresist. This lift-off process begins with patterning a layer of positive Shipley-1813 photoresist

on a substrate to resolve the region where the bio-nanostructure will ultimately be immobilized. The photoresist is exposed by UV light for 15 seconds and developed with Microposit-352 developer solution. Post-development, the photoresist is flood-exposed for 30 to 40 seconds to expose all photoresists left on the wafer and to allow lift-off. The recessed lift-off process has an additional step that consists of using the patterned and exposed photoresist as a mask to etch a 1 μm recess in the substrate using Deep Reactive Ion Etching (DRIE). The recess is etched in an effort to accelerate the process of lift-off by creating an easier access to the photoresist. An optional Electron Beam (E-Beam) Evaporation of titanium (Ti) (10 nm) and gold (Au) (50 nm) layer is deposited to form a homogenous bonding surface for bio-nanostructure assembly. Finally, the chips are immersed in TMV-*n*1Cys or VLP-*n*1Cys solution (0.1-0.2 mg/mL) overnight to allow for the self-assembly of bio-nanostructures on the surface.

Solvents used for lift-off need to be carefully considered because excessive exposure to the TMV or VLP can result in structural destabilization. Two lift-off methodologies utilizing developer and acetone were used and their results were compared. Microposit developer in its pure form is too basic with a pH level of 12 or higher. Microposit 352 was diluted with sodium phosphate buffer (0.1 M, pH 7) at ratios of 1:3 and 1:5, decreasing its pH level to ca. 9 and ca. 8, respectively. The milder conditions allowed for the bio-nanostructures to remain more stabilized during the process compared to the extreme pH conditions. The chips were immersed in lift-off

solution heated to 55 °C and agitated occasionally to assist in the lift off process. The lift-off process using acetone was simpler. The chip was directly immersed in acetone at room temperature. Similar agitation was used to accelerate the lift off process.

In both processes, larger structural dimensions were faster to resolve. The developer-based solution required 5 to 7 hours for patterning designs with 10 μm features. Smaller features took up to 30 hours to resolve. Moreover, the extended time to resolve these features caused some instability in the TMV structure. In contrast, acetone lift-off required only 1 to 2 hours to resolve similar featured patterns. There was no obvious sign of structural destabilization in the latter process. In both lift-off solution processes, agitation and recessed-etch accelerated the process of lift-off, decreasing the solvent exposure times. The AFM images below (Figure 5-8) show the patterned TMV-*n*1Cys on the Ti/Au layer after rinsing the chip in DI water and drying it on a hotplate at 40 °C.

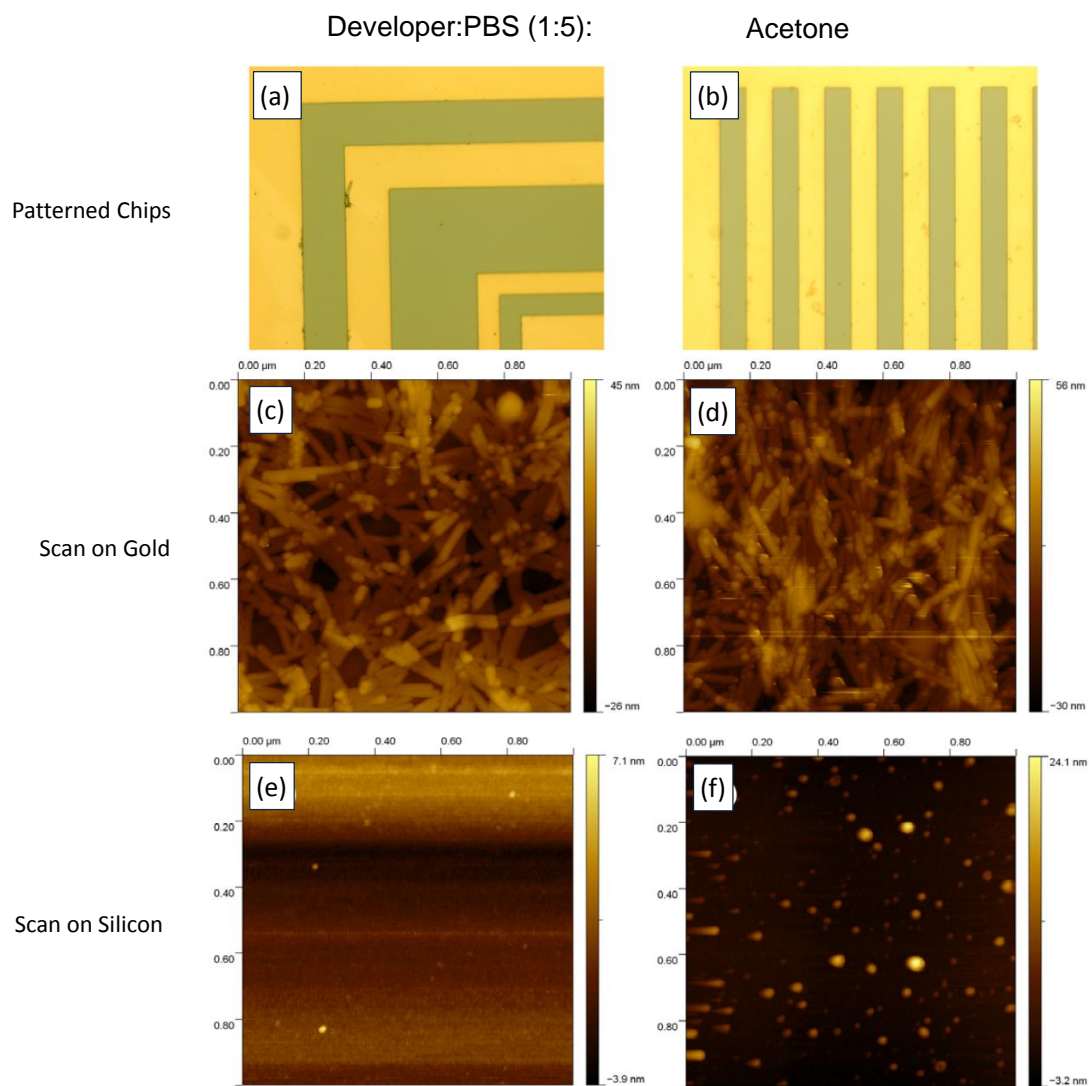


Figure 5-8 AFM images showing the surface morphology of patterned TMV using (left) diluted developer and (right) acetone

The optical image in Figure 5-8 shows the successful patterning of Ti/Au using both 1:5 diluted developer and acetone lift-off. Moreover, the bio-nanostructures assembled on the Ti/Au surface were investigated using AFM. An untreated sample with TMV-*n1*Cys assembled on the surface of Ti/Au was imaged as a control sample. As expected, a dense coating of TMV-*n1*Cys laid horizontally on the substrate. Figure 5-8 c, d, shows scans taken from the gold surfaces of the processed chip exhibiting similar to the control. Finally, the lift-off region of the chip was scanned, showing the smooth surface of the silicon substrate and the absence of nanostructures (as expected).

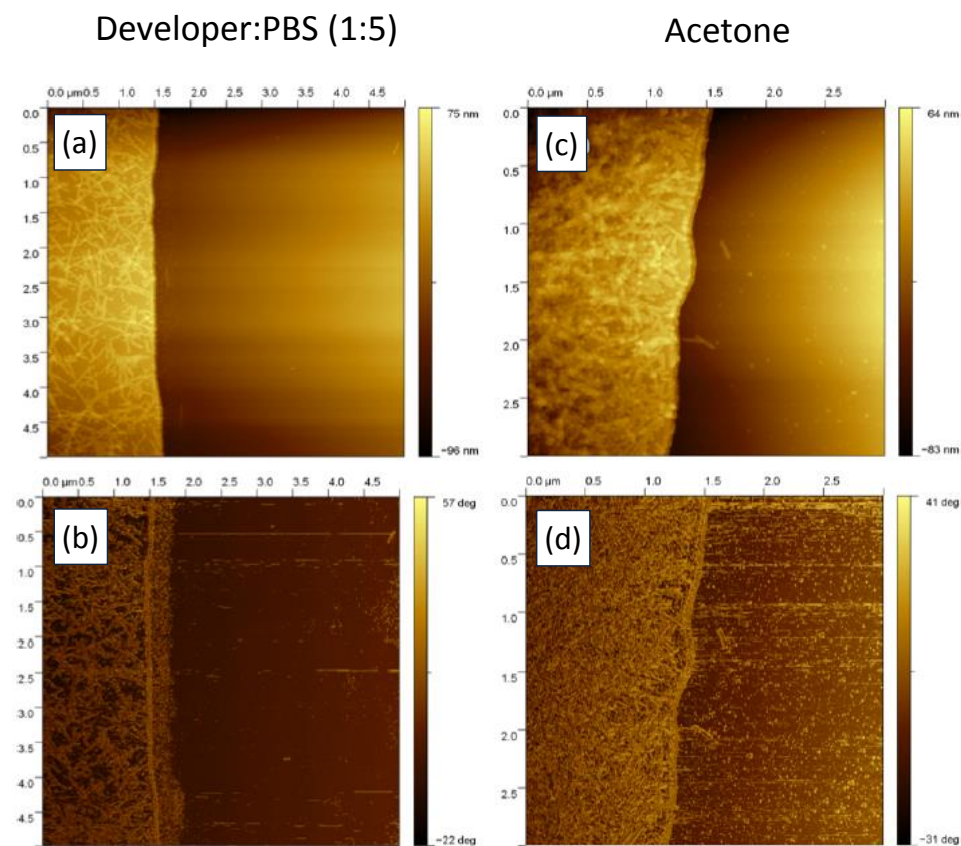


Figure 5-9 AFM images showing the boundary of the patterned TMV. (a, b) shows the amplitude and phase of the boundary patterned by diluted developer showing no obvious structure instability. (c, d) shows the amplitude and phase of the boundary patterned by acetone showing some possible denaturation

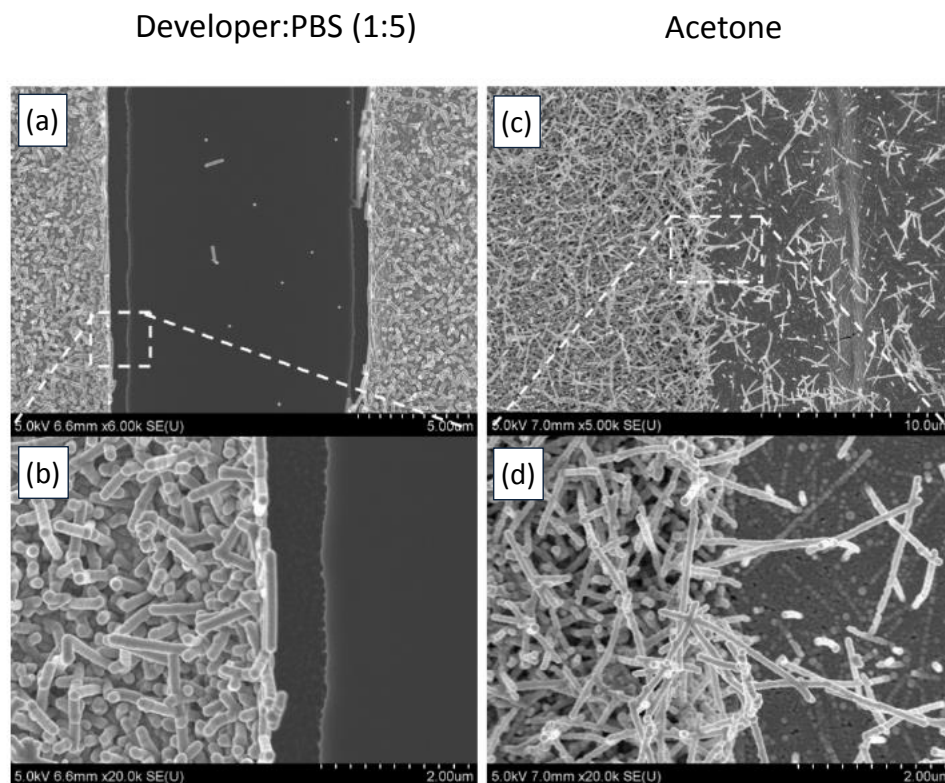


Figure 5-10 SEM images showing the boundary of TMV patterned using (a, b) diluted developer and (c, d) acetone. The TMV-*n*1Cys were metallized post patterning, demonstrating its engineered functionality is conserved through the patterning process.

Figure 5-9 shows the boundary of the Ti/Au/Bio-nanostructure lift-off in an AFM image. Figure 5-9 (a) and (b) are the amplitude and phase scan of a patterned chip using 1:3 diluted developer. Figure 5-9 (c) and (d) are the amplitude and phase scan of a patterned chip using acetone. All four images show a clear interface between Ti/Au/Nanostructure and silicon surface. By comparing the surface morphology of 1:3

and 1:5 diluted developer in Figure 5-8 and Figure 5-9 to that of the control, very minimal effect to the bio-nanostructures' surface bond and structural stability is seen. However, acetone lift-off, most evident from the phase mode AFM scan, shows virus fragments on the silicon surface. These may be attributed to the disassembly and unfolding of coat proteins from the virus structure, leading to precipitation and assembly on the bare silicon surface. This suggests that diluted developer in the range of 1:3 to 1:5 maybe a better lift-off solution than acetone in order to maintain the structural stability of the virus.

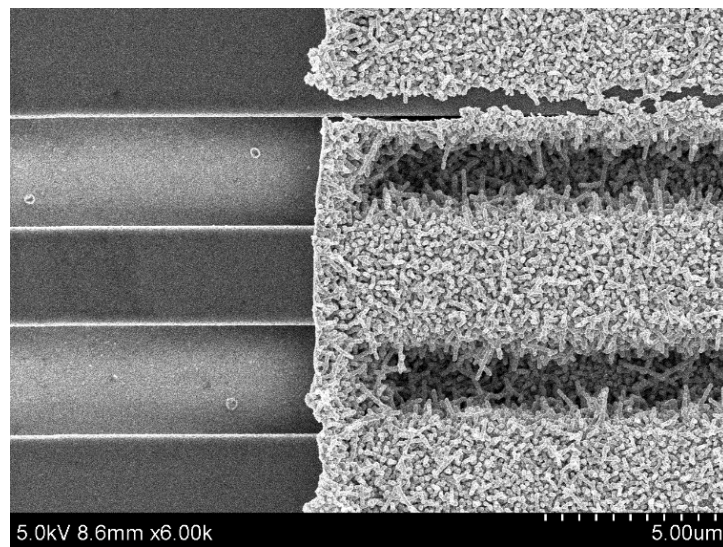


Figure 5-11 SEM image showing the patterning of TMV-*n*1Cys on microfabricated Si waveguide

Patterning of metallized TMV-*n*1Cys and VLP-*n*1Cys assembled on microstructures were also demonstrated. Figure 5-11 shows the patterning of metallized TMV-*n*1Cys on a 2.5 μm wide Si waveguide after processing a standard lift-off process. The clear boundary between assembled virus and clean surface demonstrates that the lift-off process can be used not only on planar surfaces but also on 3D structures. This allows the patterning of assembled receptor layers on specific regions of microfabricated devices.

The assembly and patterning of TMV and VLP presented in this chapter demonstrate the feasibility of integrating two distinctively different platforms. The ability to self-assemble and pattern biological particles via a traditional lithography technique provides avenues to bioreceptor integration with microsensor systems. The next chapter will describe the development of such a sensor system and its targeted applications.

Chapter 6. Selective Detection of Analyte

The demonstration of successful integration of bio-nanostructures with microfabricated optoelectronics directly leads to the application of selective sensing. The versatility provided by genetically programmable biomolecules allows for TMVs and VLPs to be receptor layers for various analytes, from explosive chemical compounds to biological antibodies. In this chapter, the detection of trinitrotoluene (TNT) vapor and Flag antibody in solution will be detailed.

6.1 TNT Sensing

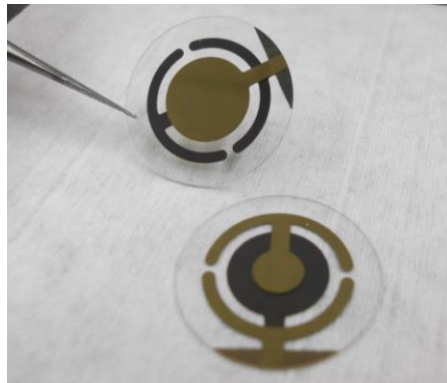
TNT is an explosive that is widely used in both military and construction purposes. Because of its toxicity and high energy, careful handling and monitoring during its production, transportation, and utilization are required to prevent potential environmental and safety hazards. TNT is a compound with small molecular weight (227 g/mol) and very low vapor pressure (ca. 2×10^{-4} torr at 25°C), which require an ultrasensitive sensor for its detection. In addition, the selectivity of TNT is important due to its electronegativity similarity to all benzene based molecules. For example, the difference between dinitrotoluene (DNT) and TNT is often indistinguishable. As a result, we leveraged the selectivity provided by the genetically modified TMV (TMV1Cys-TNT), as a receptor layer for the specific binding of TNT in vapor phase.

6.1.1 Experimental Setup

6.1.1.1 Transducer

A quartz crystal microbalance (QCM) is a bulk resonator that is used as a highly sensitive mass sensor. Its high Q resonant frequency shift is primarily dependent on the added mass on its surface electrodes with multiple secondary influences (e.g. change in dampening and viscosity). A QCM was selected as the transducer to verify the functionality of the modified virus because of its intrinsic stability, compatibility with TMV assembly, and high sensitivity.

a)



b)

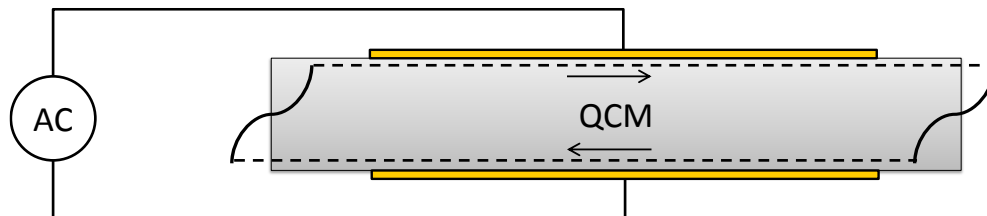


Figure 6-1 (a) A picture showing an example of a QCM used. (b) A Diagram showing the shear wave induced in a QCM generated by an external AC signal

Quartz with piezoelectric properties can generate bulk acoustic waves which may be probed electrically. When an alternating current (AC) signal is applied to the quartz resonator, a shear transverse wave is induced. Due to the specific dimensions of the resonator cut, the bulk acoustic wave can undergo constructive interference resulting in resonant conditions at specific frequencies. Either steady state operation, actuating the QCM at its resonant frequency, or transient state operation, observing the transient response of the resonator following an impulse excitation, may be used to trace the resonant frequency of a QCM. The mass loading, M_f , can be calculated by the change in resonant frequency governed by Equation 6-1).

Equation 6-1

$$\Delta f = -\frac{f_q^2 M_f}{N_{AT} P_q S}$$

where, f_q is the resonant frequency, N_{at} is frequency constant of AT-cut (1.67×10^5 Hz-cm), P_q is the density of quartz (2.65 kg/dm^3), and S is surface area of the electrode ($\sim 36.1 \text{ mm}^2$).

The velocity of the shear wave decays exponentially into its surrounding medium, rendering the QCM transduction mechanism to a surface-specific platform. The penetration depth for a 5 MHz QCM in water is only $\sim 250 \text{ nm}$ [172]. As a result, the energy dissipation caused by the medium dampening is minimal leading to only a

slight decrease in Q . The short penetration depth allows the QCM to be operated in a liquid environment and be used as a mass sensor to monitor the assembly of TMV in phosphate buffer solution.

6.1.1.2 Receptor Layer and Transducer Integration

Two different functional groups have been expressed on the virus coat protein: (1) a cysteine residue attached to the n-terminus of the TMV coat protein (TMV-*n*1Cys) that facilitate self-assembly onto substrate surfaces and (2) a TNT-specific peptide sequence fused to the c-terminus of the TMV molecule for the expression of TNT-specific binding. Two different viruses were assembled onto two sets of QCMs for TNT vapor sensing: TMV with only a cysteine residue mutation (TMV-*n*1Cys) and TMV with both cysteine residue and TNT-specific peptide mutations (TMV1Cys-TNT). A third set of QCM was used as a control with no TMV receptor layer coating (uncoated).

The TMVs were assembled on the transducer by covering the top surface of a QCM with 0.3 mL of their respective TMV solution at a concentration of ~ 0.1 g/mL. The QCM surface was covered with the solution for 24 hours before it was rinsed with DI water to remove any unassembled virus on the surface. QCMs were then dried on a hot plate at 40°C for 30 minutes.

An independent experiment was conducted to continuously monitor the attachment of TMV-*n*1Cys on a QCM by tracing the QCM's resonant frequency shift

during the assembly period. Atomic force microscopy (AFM) images of the QCM surfaces were taken post-assembly to verify the assembly of the virus and inspect the surface morphology.

6.1.1.3 Testing Protocol and Data Acquisition

The resonant frequency of the QCMs (purchased from ICM, USA) was measured pre and post-receptor layer assembly, and continuously monitored during the introduction of TNT vapor to the QCMs' surface. The resonant frequency of the QCMs was measured in steady state operation using an oscillation circuit (ICM, USA) and an Agilent E4402B spectrum analyzer. The resonant frequency is calculated, monitored, and logged using a LABVIEW acquisition program. Resonant frequency samples were logged every four seconds, limited by the time required for the DAQ card to communicate with the spectrum analyzer via a GPIB connection.

TNT vapor was introduced to the QCM surface by vapor pressure released by solid-state TNT. The QCM resonator is housed in a metallized container to isolate electric interference and sample introduction. TNT stimulant were placed inside the metallized contained and saturated the air inside the QCM container at room temperature (~25°C). A commercial TNT stimulant product called Non-hazardous Explosive for Security Training and Testing (NESTT) — TNT (purchased from XM Division of VanAken International, USA) was used as the source of TNT vapor.

NESTT are non-explosive substances that are conventionally used to train bomb sniffing canines. NESTT TNT is made by coating fused silica with real TNT (8% by weight). The coated TNT, although very light by weight, has a large surface area and generates a very high vapor pressure. Due to the low vapor pressure of silica compared to TNT, NESTT TNT expresses only a TNT vapor signature, and is calibrated to express the same vapor signature and pressure as the same volume of pure TNT material. NESTT TNT is ideal for safe characterization of a TNT sensor.

The resonant frequency of the QCMs was measured for 30 minutes to establish a baseline measurement of each sample before and after the virus assembly. The minimum detectable frequency shift, based on the standard deviation of the noise level, of the resonators was determined from their respective baseline measurements. Each QCM was monitored for at least 30 minutes starting from the introduction of TNT vapor. Extended monitoring for multiple hours was also conducted to examine the long term stability of the sensor system and to verify the full saturation of TNT attachment onto the receptor layer or adsorption onto the surface of the QCM

6.1.2 Results

AFM images of the QCM surfaces showed the assembly of TMV (Fig. 3). However, TMV1Cys-TNT resulted in a reduced and less uniform coating density than the TMV-*n*1Cys. TMV1Cys-TNT aggregated into clusters rather than a uniform

monolayer of TMV (Figure 6-2 (c)). This assembly of the virus was also indicated in the smaller mass shift measured by the microbalance, shown in Figure 6-2.

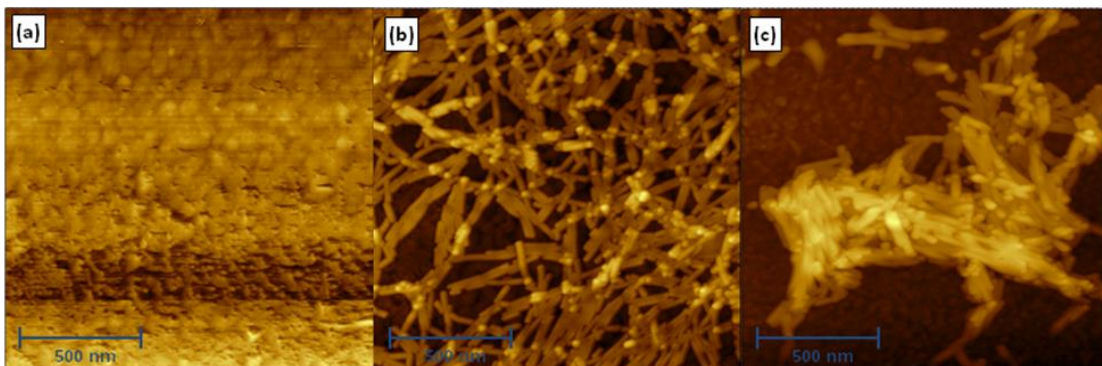


Figure 6-2 AFM images showing the surface morphology of (a) uncoated, (b) *I*cys-TMV, and (c) TNT-TMV coated QCM surfaces.

The continuous monitoring of the TMV-*n*1Cys assembly onto a QCM surface showed that 90% of the final virus assembled within the first 7 hours of the virus introduction. The final assembled mass of the TMV-*n*1Cys at the end of the 24 hour assembly period was 2.20 $\mu\text{g}/\text{cm}^2$.

After exposing TNT vapor to the surface of the QCMs, the resonant frequency of the uncoated, TMV-*n*1Cys, and TMV1Cys-TNT coated QCMs shifted 3 Hz (19.2 ng), 8 Hz (51.2 ng), and 12 Hz (76.9 ng) respectively. Final TNT sensing measurements were made after the resonant frequency had leveled off to a steady state for 10 minutes. TNT attachment to the surface of the QCMs was saturated in approximately 15, 20,

and 40 minutes for the uncoated, TMV-*n*1Cys coated, and TMV1Cys-TNT coated QCM, respectively.

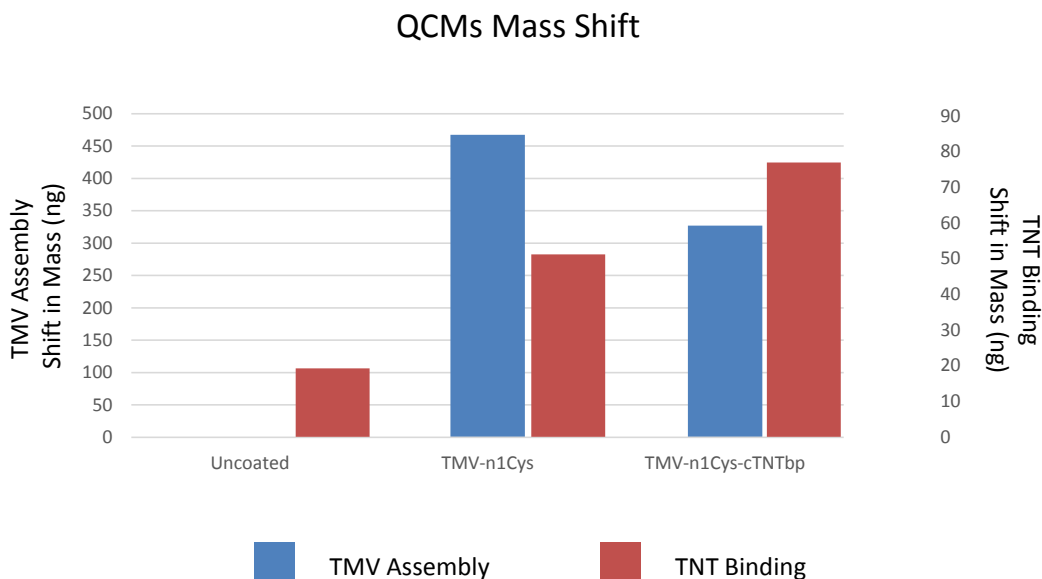


Figure 6-3 Graph showing the mass shift due to TMV virus assembly (blue) and TNT exposure (red) of uncoated, TMV-*n*1Cys, and TMV1Cys-TNT coating of QCM surfaces

TMV1Cys-TNT coated QCM was then continuously exposed to saturated TNT vapor for 10 hours without any additional shift in frequency after the initial saturation curve. The noise level of the resonant frequency measurement is below that of the minimum resolution of the spectrum analyzer used, causing discrete jumps of 1 Hz in measured frequency shift.

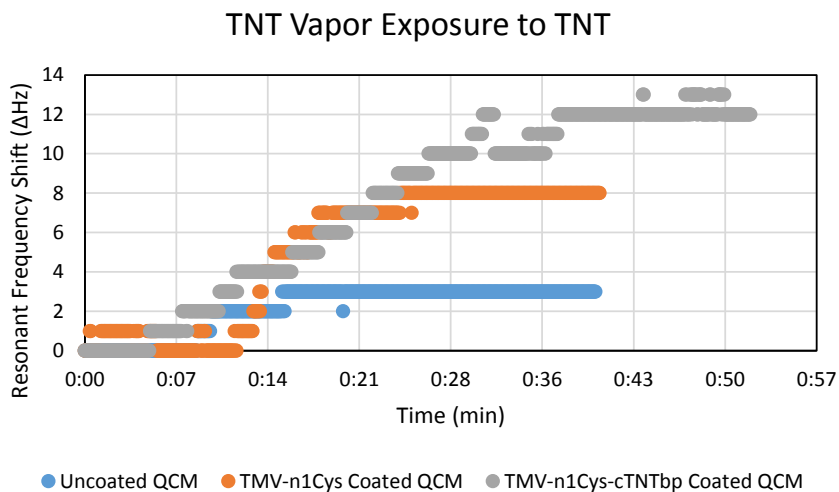


Figure 6-4 Graph showing the resonant frequency shift due to TNT vapor introduction of three QCMs with uncoated (blue), TMV-*n*1Cys (Orange), and TMV1Cys-TNT (grey) coating of QCM surfaces

6.1.3 Discussion

The 300% and 50% increase in resonant frequency shift of the *TNT*-TMV coated QCMs compared to that of uncoated QCM and TMV-*n*1Cys coated QCM, even with less uniform and sparser virus morphology, is attributed to the successful expression of TNT-specific peptides on the outer surface of the viral structure, which caused an increase in binding affinity. Uncoated and TMV-*n*1Cys frequency shifts are attributed to nonspecific binding and adsorption. Based on the successful detection of TNT vapor, which has a vapor pressure of $\sim 2 \times 10^{-4}$ Torr, ~ 7.6 ppb at 25°C, the detection

limit of these resonator sensors is below a few ppb. The detection limit of the QCM is believed to be even lower because the current mass resolution limit is restricted by the resolution of the spectrum analyzer used to detect the resonant frequency of the QCM. The noise level of the QCM's resonant frequency is lower than the resolution limit as evident in Figure 6-4, demonstrating discrete jumps in frequency. As a result, a minimum measurable shift of $1 \pm 0.5\text{Hz}$ can be measured, corresponding to a mass resolution limit of 3.2 ng in the current setup. The sensitivity of the system, the change in resonant frequency with respect to change in mass, is directly proportional the squared of the resonant frequency ($\Delta f_o/\Delta M_f \sim f_o^2$, from equation (1)). By utilizing a higher resonant frequency QCM, e.g. doubling the QCM's resonant frequency to 10 MHz, the sensitivity of the system can be increased by a factor of four.

To further increase the sensitivity and the effectiveness of the TMV1Cys-TNT receptor layer, the assembly of the virus on the gold surface needs to be improved upon. If uniform assembly of high density virus can be achieved, exposure of TNT selective peptides can be dramatically increased. Both functional groups need to be properly expressed on the coat protein of the TMV. Based on recent results, it is believed that the mutant expression on the coat protein may have been denatured or destabilized during incubation. In order to increase the virus packing density, further experiments are needed to investigate the dependence of substrate material and the virus genetic stability through the infection and incubation stages.

6.2 Selective Antibody Detection

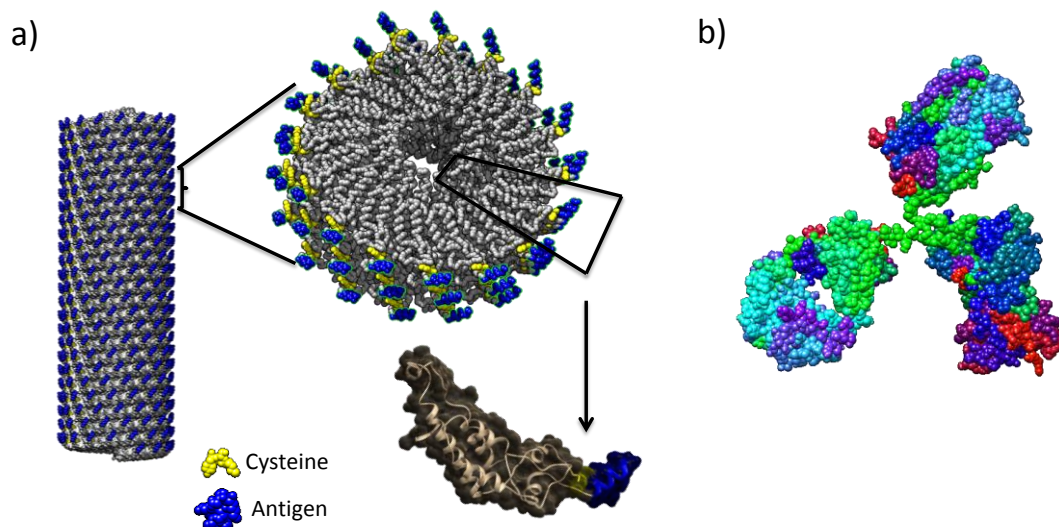


Figure 6-5 CAD diagram showing the molecular structure of (a) a TMV1Cys-VLP-FLAG showing both the cysteine and FLAG antigen on the outer surface of the VLP nanorod and (b) an representative antibody with two antigen binding sites

To demonstrate the versatility of the TMV to be genetically programmed to express high affinity towards different target analytes, antibody binding was selected as a demonstration of proof of concept towards selective biomolecule detection. Antibodies are used by the immune system to identify and neutralize foreign objects. Antibodies are Y-shaped proteins. Each tip of the Y possesses a paratope, which is complementary to an epitope present on an antigen. The high recognition property

between a paratope and an epitope is the basis for the high affinity between antigen and antibody. This special bond is not only used as a tag but also can neutralize its target by suppressing the targets functionality. In research, the detection of antibodies is critical for medical diagnosis and treatment and drug discoveries. In the following sections, TMV1Cys-VLP-FLAG will be used to leverage its programmed selectivity towards a targeted antibody. Conventional enzyme-linked immunosorbent assay (ELISA) on a chip, consisting of a TMV1Cys-VLP-FLAG receptor layer and an optical resonator, will be detailed. The sensor system's sensitivity and selectivity will be investigated. Furthermore, the platform's capability to detect analyte in a label-free manner will be explored, potentially decreasing the time and cost of traditional detection methods.

6.2.1 Experimental Setup

6.2.1.1 Transducers

The transducer used in the detection of antibody binding was an optical whispering gallery mode resonator. Transitioning from a bulk resonator to a microresonator platform will facilitate future system integration, enable sensor multiplexing, and decrease cost. The theory, design and simulation, fabrication, and testing of this optical resonator platform were previously detailed in Chapters 2 and 3.

6.2.1.2 Receptor Layer and Transducer Integration

Virus-Like-Particles (VLP) were synthesized and purified as previously described in Chapter 4. VLP conjugated with the cysteine residue (VLP-*n*1Cys) was used as a control receptor layer to test the non-specific binding of the nanostructured receptor. VLP conjugated with the cysteine residue and the complementary antigen to FLAG antibody (TMV1Cys-VLP-FLAG) was used as the selective receptor layer for the binding of FLAG antibodies. The cysteine residues expressed in both VLP-*n*1Cys and TMV1Cys-VLP-FLAG allowed for the self-assembly of the VLPs onto the surface of the optical resonator. The chip was immersed in a 0.2 mg/mL solution of VLP overnight (minimum of eight hours) to allow for the assembly of VLP. The resonator chip was then dipped in DI water to rinse off any unattached VLP on the surface. The chip is then placed on a hot plat at 40°C for 30 minutes until it is dried and ready for optical characterization.

6.2.1.3 Testing Protocol

An optical spectrum of the resonator was acquired before and after VLP assembly utilizing the optical testing setup described in Section 3.2. Post VLP assembly, the chip underwent conventional ELISA protocols (see Appendix C). ELISA is a wet biochemical assay that utilizes solid-phase enzyme immunoassay to monitor

and track the presence of proteins, such as antigens or antibodies, in a liquid or wet sample.

Traditionally, ELISA is conducted by:

- (1) Immobilizing antigens on sample surface
- (2) A complementary antibody (primary) is applied over the surface for specific binding to the antigen
- (3) A color changing enzyme can be either attached to the antibody or a secondary antibody that specifically attaches to the primary antibody, as a visual indicator
- (4) The enzyme's substrate is added to induce a change in color to produce a detectable signal, which can be quantified using an imaging software.

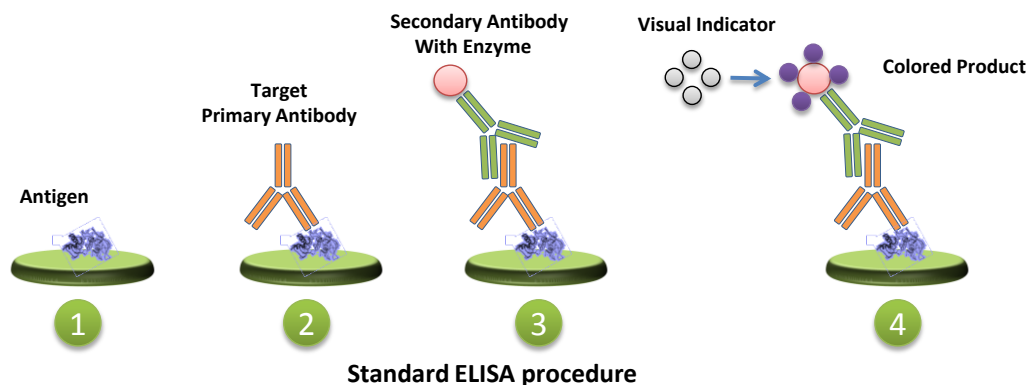


Figure 6-6 Process flow showing the standard procedure of a sandwich ELISA protocol

In this experiment,

(1) Antigens (FLAG) are expressed on the outer surface of the VLP for antibody binding and are immobilized on the transducer surface via the cysteine residue. The VLP decorated optical resonator is then immersed in 5% non-fat milk in Tris Buffer Solution (TBS) for 30 minutes at room temperature as a blocking step, to block any non-specific binding sites.

(2) The chip is then transferred to a 1/1000 dilution of primary antibody sera in TBS and 5% non-fat milk solution for 2 hours at room temperature. The chip was then rinsed with TBS and TBS with 0.05% Tween 20 detergent (TBS-Tween).

(3) A secondary antibody with color changing enzyme was added to the primary antibody by introducing the chip to 1/5000 dilution of anti-rabbit alkaline phosphatase

in TBS 5% non-fat milk for an additional 2 hours at room temperature. A similar TBS/TBS-Tween rinse step was carried out.

(4) Finally, enzyme substrate (color indicator) in substrate buffer was used to change the enzyme, now decorated on each attached antibody, to a violet color. After a rinse and dehydration step, the optical spectrum of the optical resonator was captured.

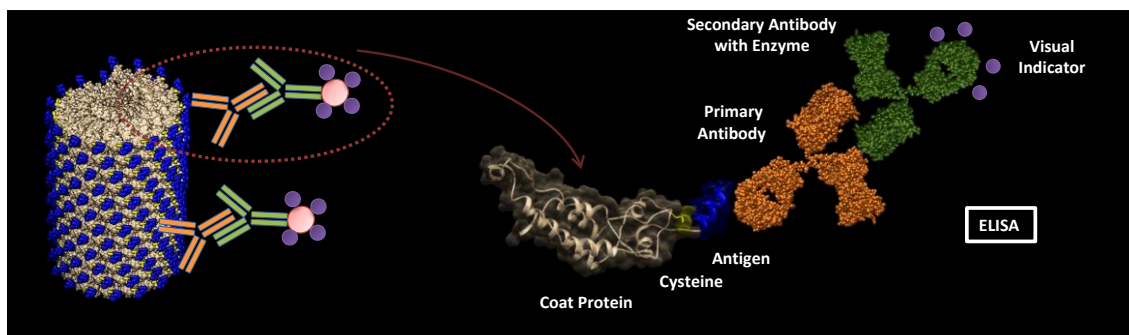


Figure 6-7 Diagram showing the principle of ELISA-on-a-chip using self-assembly TMV1Cys-VLP-FLAG

The entire immunoassay process is a continuous all wet protocol that requires all biological agents to be kept in liquid conditions. As a result, the optical spectrum of the resonator was only taken before and after the ELISA procedures.

The detection limit of the resonator was found to be lower than the required sensitivity to detect the entire binding sequence of ELISA – the attachment of the primary antibody, secondary antibody with enzyme, and the substrate indicator

assembly. The platform was used to simplify ELISA by monitoring just the binding of each antibody, without the use of substrate indicator, eliminating the need to label or tag target molecules. This would simplify traditional ELISA protocols, decreasing the time of experiment and reducing the required biomolecule participants and cost. Primary antibody of different concentrations, varying from 1/8000 to 1/2000 dilution, were used to calibrate the sensitivity of the sensor platform. To accomplish label-free detection of antibody binding, the optical spectrum of the resonator was taken before and after the immobilization of VLPs onto the resonator and after the assembly of each antibody. The chips had to be tested in dry conditions due to the limitation of the testing setup. As a result, post antibody assembly in milk, the chip was rinsed in TBS and DI water, dried at room temperature, and then tested.

The viability of drying the biomolecules needed to be verified. To investigate the effects of dehydration and rehydration of the VLP and the attached antibody, independent ELISA tests were conducted on gold coated Si chips. The full protocol of ELISA was conducted on two sets of gold coated chips. Each set was immobilized with 4 different concentrations of TMV1Cys-VLP-FLAG receptors: 10^{-2} mg/mL, 10^{-4} mg/mL, 10^{-6} mg/mL, and 0 mg/mL. The first set of chips underwent traditional ELISA and used as a control. The second set of chips underwent a modified ELISA procedure where a DI rinsing and drying step was inserted between each biomolecule assembly, resulting in a total of three dehydration and rehydration steps. Final color intensity

changes between the two sets were compared, reflecting the level of preserved functionality of the dehydrated and rehydrated biomolecules.

Lastly, specificity of the TMV1Cys-VLP-FLAG binding was investigated in three independent experiments. Introduction of FLAG antibody solution were compared to that of (1) non-fat milk solution, (2) non-complementary His-Tag antibody, and (3) non-complementary HA-Tag antibody. Non-fat milk is used because it contains a multitude of amino acids, proteins, vitamins, and minerals that could potentially non-specifically bind to the sensor surface. His-Tag and HA-Tag antibodies detect recombinant proteins containing the 6xHis and the HA epitope tag, respectively, both not present in TMV1Cys-VLP-FLAG structures.

6.2.2 *Results*

6.2.2.1 VLP Attachment

The optical spectrum taken before and after the overnight VLP attachment showed a resonant wavelength shift of 2.21 ± 0.34 nm and 1.05 ± 0.23 nm for VLP-*n*1Cys and TMV1Cys-VLP-FLAG, respectively. The 2.21 nm and 1.05 nm shift corresponds to an effective refractive index shift of 2.08×10^{-3} and 0.99×10^{-4} RIU, respectively. Based on SEM imaging, the morphology of the two types of VLPs showed a small variation in VLP coating density. VLP-*n*1Cys coating was denser and more uniformly conformal than TMV1Cys-VLP-FLAG's coverage. The variability in the

wavelength shift within each type of VLP assembly is attributed to the randomness of the nanostructure assembly on the surface of the disk resonator and the variation between batches of VLP synthesis and purification.

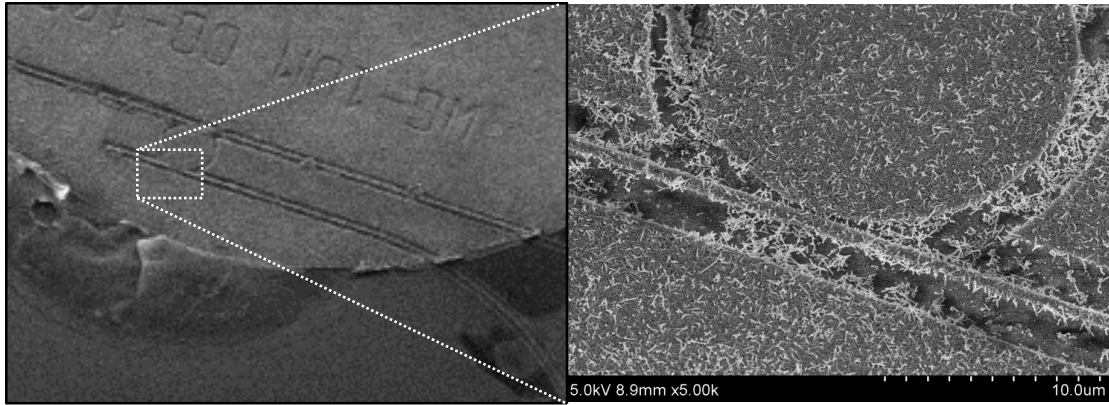


Figure 6-8 SEM images showing the assembly of TMV1Cys-VLP-FLAG on a fully microfabricated disk resonator

The VLP assembly, as observed in the SEM images, show non-uniform assembly across the surface. The length, orientation and density of the VLP on the surface of the resonator will influence the propagating wave – receptor layer interaction and shift the effective refractive index by a different magnitude.

6.2.2.2 ELISA: TMV1Cys-VLP-FLAG vs VLP-*n*1Cys

The optical spectrum shifts of 2.13 ± 0.57 nm and 7.00 ± 2.68 nm, corresponding to a -3.62% and a +567% relative shift in wavelength compared to the shift caused by their initial VLP assembly, were observed on resonator chips decorated

with VLP-*n*1Cys and TMV1Cys-VLP-FLAG, respectively. Each chip underwent parallel VLP assembly followed by ELISA protocol procedures, which assembled primary and secondary antibodies followed by enzymatic substrate assembly.

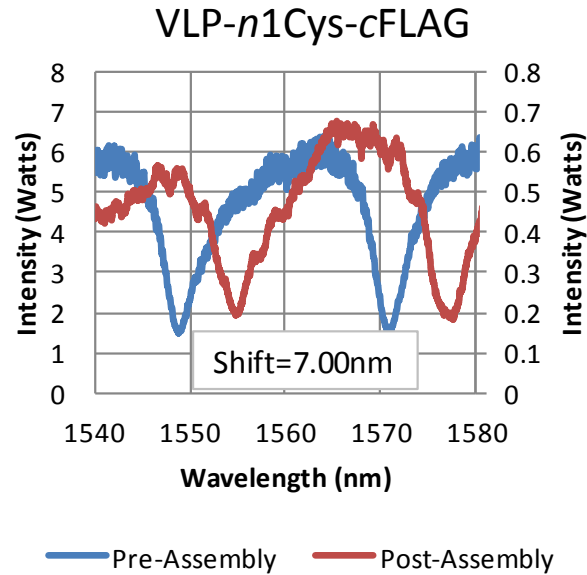


Figure 6-9 Optical frequency spectra showing the shift in resonant frequency due to the assembly of TMV1Cys-VLP-FLAG

The negative shift 3.62% resonant wavelength shift produced by VLP-*n*1Cys decorated sensor suggested that not only did the primary and secondary antibody not bind to the VLP-*n*1Cys receptor layer, but some VLP structures may have been disassembled or denatured in the process. The optical chip immobilized with TMV1Cys-VLP-FLAG, on the other hand, showed a positive shift of 567%, produced

by TMV1Cys-VLP-FLAG assembly and the full ELISA procedure. This additional shift corresponds to an additional 5.61×10^{-3} RIU shift. This dramatic shift is attributed to the primary and secondary antibody binding with enzymatic substrate reaction. The comparison between the -3.62% and the 567% shift of the TMV1Cys-VLP-FLAG and VLP-*n*1Cys, respectively, demonstrated the selectivity provided by the expressed FLAG antigen on the outer surface of the VLP, proving that the VLP receptor layer can be used for selective sensing.

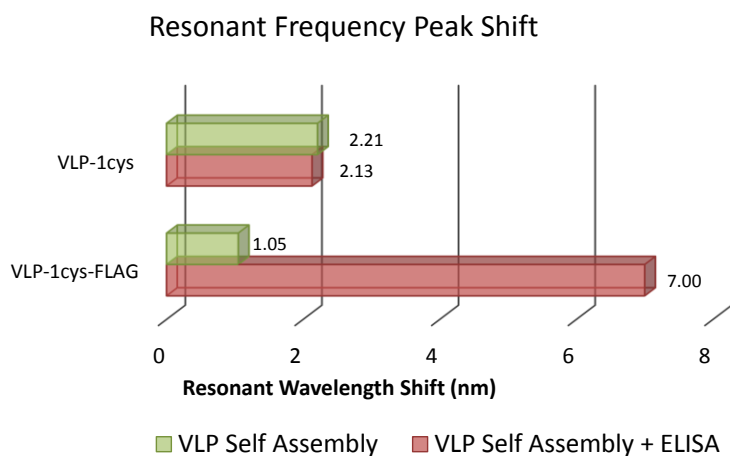


Figure 6-10 Resonant frequency shift due to the assembly of VLPs, followed by conducting ELISA-on-a-Chip

6.2.2.3 Primary antibody attachment and secondary antibody attachment

Label-free detection, without the use of enzymatic substrate reaction, was investigated. After immobilization of TMV1Cys-VLP-FLAG on to two disk resonator chips, primary antibody was introduced onto one sensor system and primary and secondary antibody was introduced onto the other. Neither system underwent enzymatic substrate reaction that induces the change in the color indicator. The binding of the primary antibody and primary and secondary antibodies onto VLPs caused a shift in resonant wavelength of 0.79 ± 0.41 nm (+51%) and 2.10 ± 0.78 nm (+135%), respectively. These increasing positive shifts correspond to the binding of the primary antibody followed by the secondary antibody, demonstrating the ability of the sensor platform to detect the binding of analyte without labeling or visual indications. The reduced magnitude in wavelength shifts caused by antibody bindings further suggests that the 567% shift caused by the full ELISA procedures was predominantly induced by the substrate indicator assembly.

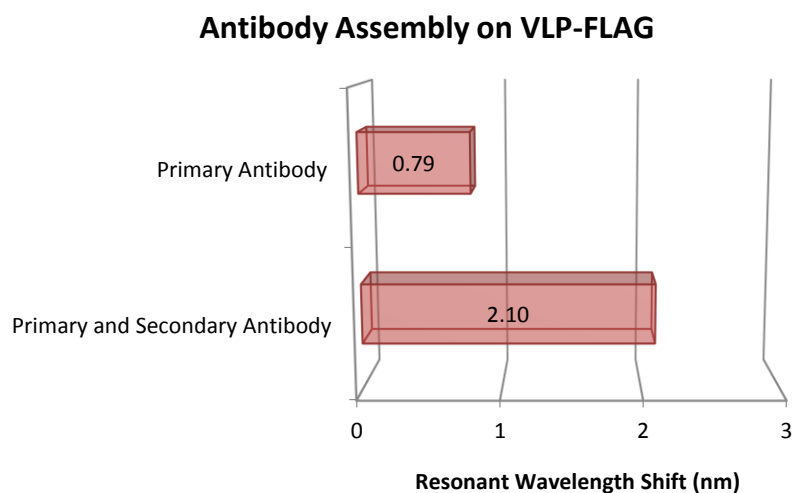


Figure 6-11 Resonant frequency shift induced by the binding of the primary and secondary antibodies

To further verify the selectivity of TMV1Cys-VLP-FLAG to FLAG antibodies, another experiment was conducted using TMV1Cys-VLP-FLAG decorated resonator chips. Three resonator devices were immersed in milk for 2 hours and then rinsed and dried. This immersion in milk caused a -0.021 nm (-7.09%) in resonant wavelength. A second set of devices were immersed in milk containing FLAG antibodies and caused a $+0.124$ nm ($+41.9\%$) shift in resonant wavelength. The difference in the wavelength shift caused by the different solutions further demonstrated the ability of the sensor platform to selectively detect targeted analyte against milk contents without the use of labeling. To demonstrate the VLP's selectivity against non-complementary antibodies,

two sets of TMV1Cys-VLP-FLAG decorated resonator chips were each introduced to milk spiked with either antibody His or antibody HA. Both antibodies should not have any special affinity to VLP, 1Cys, or anti-FLAG. This was validated by the sensor response. All sensors showed no binding effects on the resonator, causing a negative shift in both responses.

All the negative shifts in resonant wavelength acquired were caused by the introduction of non-complementary solutions. It is hypothesized that substances were removed or detached from the surface of the optical cavity caused by either the disassembly or mild denaturation of the VLPs. This was investigated by a set of independent experiments done on bare gold coated silicon chips. The full ELISA protocol was conducted on two sets of gold chips with different concentrations of TMV1Cys-VLP-FLAG immobilized on its surface. After each antibody assembly (primary and secondary) stage, both sets of chips underwent the same rinsing protocol. The only difference in procedure between the two sets of gold chips is that while one set, the control set, remained in a wet condition, the other set was dried at room temperature under a fume hood until complete dehydration (approximately 10 minutes) after each rinse stage. The color intensity of the enzymatic substrate assembly of each chip was acquired and analyzed using ImageJ software. The results show that the set of chips that underwent drying had an overall lower color intensity compared to the chips that remained wet during the entire duration of ELISA.

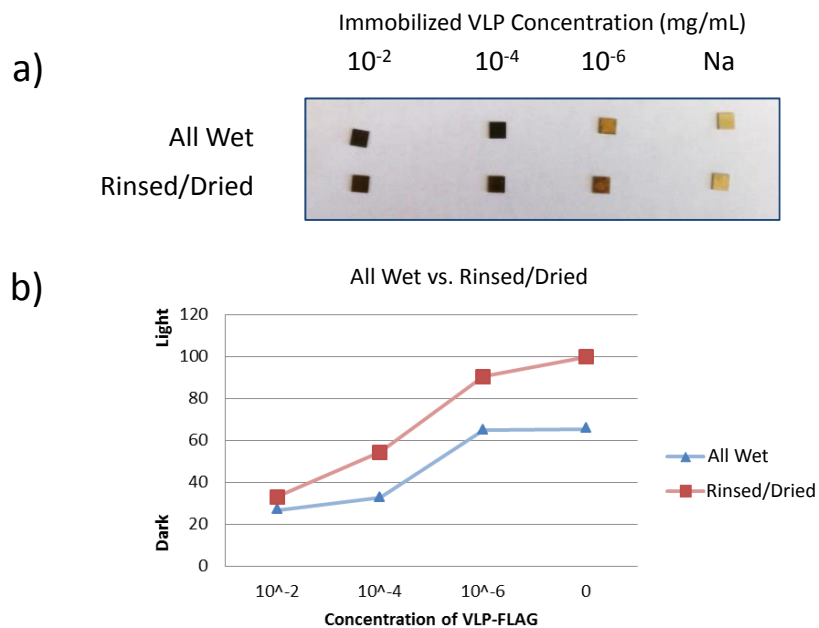


Figure 6-12 (a) Picture showing the color intensity of ELISA conducted on gold coated chips under all wet conditions versus rinsed and dried conditions. (b) Color intensity analysis of the two set of ELISA chips showing an overall less dense color intensity for the rinsed and dried samples

The lower color intensity indicates less enzymatic substrate reaction due to the reduced presence of secondary antibodies. This indicates that dehydration and rehydration have an adverse effect on the expression of the colored indicator on immobilized TMV1Cys-VLP-FLAG.

6.2.3 Discussion

The difference between the assembly of VLP-*n*1Cys and TMV1Cys-VLP-FLAG on resonator sensors is expected. The self-assembly of *n*1Cys on the sample surface can be affected by the additional mutation of FLAG antigen in numerous ways: (1) the FLAG antigen expressed on the outer surface may disrupt the self-assembly of VLPs due to steric hindrance, blocking the cysteine binding site on the n-terminus on the 3' end and reducing the number of VLPs bound to the surface; (2) the presence of FLAG antigen may cause a weaker bond between the cysteine and the surface. During rinsing and chip manipulation, some VLPs may have detached from the surface, leaving uncovered surfaces on the resonator; and (3) FLAG antigen expression on each coat-protein of the VLP may have influenced the VLP to form shorter helical rods, resulting in a thinner layer of VLP structures and a smaller amount of coat protein on the surface of the resonator interacting with the evanescent wave. These factors could have all led to a smaller wavelength shift induced by the TMV1Cys-VLP-FLAG assembly compared to that of VLP-*n*1Cys.

The standard deviation could be caused by the VLP assembly variation across the sensor chip. Due to the small footprint of the resonator cavity, $<1200 \mu\text{m}^2$, random cluttering on the cavity surface or between the coupling gaps can greatly influence the resonant wavelength shifts, as observed in the SEMs below,. It has been observed that there are variations across a chip and certainly between chips, both in TMV and VLP

immobilizations. The purity and concentration of the purified VLP vary from batch to batch. As a result, all sensing experiments were compared to parallel control experiments. In addition, resonant wavelength shifts subsequent to the initial VLP immobilization was characterized by the relative wavelength shift percentage,

$$\frac{\Delta\lambda_{Analyte\ Attachment}}{\Delta\lambda_{VLP\ Immobilization}} \times 100\%$$

Rather than absolute wavelength shift. This would more accurately report on the subsequent attachment relative to the available VLP participating in the optical interrogation from the resonator.

The 5.95 nm (567%) shift observed by the TMV1Cys-VLP-FLAG decorated resonator is a very dramatic shift for a RI sensor. The magnitude of the shift compared to that of the VLP assembly suggests that the large resonant shift is dominated by the coloring of the surface caused by the enzymatic substrate reaction, rather than the assembly of the antibodies. This dramatic shift led us to believe that this sensor system platform is capable of resolving smaller binding events, potentially sensitive enough to monitor the assembly of antibodies rather than its visual indicators.

The wavelength shift induced by the primary and secondary antibodies were considerably smaller than the wavelength shift induced by the entire ELISA protocol, but still well above the noise level. The comparison between the induced shifts caused

solely by the primary antibody attachment (+51%) versus the secondary antibody (84%) is also reasonable due to the extra enzyme attached to the secondary antibody.

It is difficult to quantify the binding density of the antibodies because the wave – analyte interaction is not only dependent on quantity but also exponentially dependent on the location with respect to the surface of the resonator and the distance from the circumference. This is another source of variability in the magnitude of the resonant wavelength shifts.

The negative wavelength shifts and the discoloration of the gold chips strongly suggest that fewer substances are involved in the interaction with the optical wave due to the hydration and dehydration steps. While this decreases the sensitivity of the sensor system, it is just a limitation of the experimental setup that requires the sensor chip to be dried during the optical characterization process. The optical resonator was designed as a universal sensing platform that could be interrogated under wet conditions. A microfluidic device needs to be designed and integrated with the existing platform to confine the solution and allow optical coupling on and off the chip. This design would circumvent the need to dehydrate the chip and allow for multisensors on a single chip. This proposed system design and development as well as sensor sensitivity optimization are all part of the future work of this project and will be elaborated in more detail in the next chapter.

Chapter 7. Summary and Future Work

7.1 Summary of Work

This dissertation presented the development of sensor systems that take advantage of the sensitivity provided by optical transducers and the high affinity binding offered by bioreceptors. The impact of this project lies in the integration vastly different components to develop a sensor system that possesses the advantages of each technology. Significant effort was undertaken to understand and integrate each component, including the development of an optical whispering gallery mode resonator and the synthesis of genetically mutated viruses

An optical resonator is a highly sensitive refractive index sensor that was selected as a transducer platform to monitor the assembly of molecules. This sensing platform is ideal for Lab-on-a-chip applications due to its real-time response, compatibility with both vapor and liquid phase detection, versatility in material integration, and ability to be arrayed and multiplexed. A microdisk resonator was designed based on finite element modeling analysis. The microdisk was fabricated in a Si_3N_4 stack on top of a SiO_2 cladding layer. Systematic fabrication characterization was conducted to ensure proper pattern transfer. Finally, the testing and characterization of the optical resonator was done utilizing a customized optical setup. The characterization of the optical resonator resulted in a Quality factor of 350, an effective

refractive index of 1.710, and a minimum detectable effective refractive index shift of 1.59×10^{-5} RIU.

In parallel, the synthesis and purification of two genetically programmed bioreceptors, *Tobacco mosaic virus* (TMV) and its derivative *Virus-like-particle* (VLP), were developed. Both TMV and VLP are high aspect ratio nanorod structures, consisting of identical coat protein subunits. Due to their genetically programmable coat proteins, they can potentially be used as a universal bioreceptor template that can coat the surface of transducers. As a proof of concept, TMV and VLP were each conjugated with a cysteine residual to allow for the vertical self-assembly of TMV-*n*1Cys and VLP-*n*1Cys on flat and 3D microstructure surfaces. Furthermore, a second residue conjugation was added to the surface of the nanorods to selectively bind to the targeted analyte. A 12-amino acid long peptide with high affinity to TNT molecules, was expressed on the outer surface TMV-*n*1Cys, resulting in a receptor with a high binding site density and the ability to be immobilized onto the surface of a transducer. Likewise, VLP-*n*1Cys was conjugated with a second residue, FLAG antigen, for the selective recognition of FLAG-antibodies.

The recognition properties of biomolecules are commonly used in nature and leveraged in artificial sensors. However, their integration with microdevices has been hampered by their incompatibility with traditional semiconductor processes. One of the major issues addressed in this dissertation is the integration of the bioreceptor layers

with transducer platforms. Specifically, TMVs and VLPs were assembled and patterned on flat and 3D microstructured surfaces, demonstrating their compatibility with some conventional microfabrication techniques. Conformal coatings of bio-nanostructures were observed on various materials and geometric cavities. Coupled with their high affinity to target analytes, this enabled the realization of two hybrid sensors systems, a TNT vapor sensor and an antibody immunoassay sensor. TMV1Cys-TNT was immobilized on to the surface of a quartz crystal microbalance (QCM) and for the first time demonstrated the high affinity for TNT. This demonstration showed a 300% larger shift in mass compared to QCMs without any TMV coating when TNT vapor was introduced to the system. Alternatively, TMV1Cys-VLP-FLAG were immobilized on the fabricated microdisk resonators. ELISA on-a-chip was conducted and showed a resonant frequency shift of 4.87 nm. Furthermore, label free antibody detection was demonstrated by introducing just antibody FLAG and observing a shift of 0.79 nm. The selective antibody-antigen binding was verified against non-complementary antibodies, proteins, and salts.

This is the first demonstration of utilizing a virus based receptor layer for the selective detection of TNT and FLAG antibody. The importance of this development is the genetically programmable coat protein that can display a multitude of unique binding motifs on transducer surfaces for numerous target molecules.

7.2 Summary of Accomplishments

The main accomplishments of this work are summarized below

- **Development of an optical transducer platform**
 - Microdisk resonators were successfully micofabricated, resolving minimum features down to 100 nm using electron beam lithography and 4:1 aspect ratio etch profile using reactive ion etching
 - Optical resonators were characterization and tested, showing a minimum detectable effective refractive index unit shift of 1.59×10^{-5}
- **Development of virus based receptor layers**
 - *Nicotiana benthamiana* plants were inoculated for the synthesis of TMV1Cys-TNT to display dual conjugations on the outer surface of the TMV
 - *E. Coli* bacteria were cultured for the synthesis of VLP-*n*1Cys and TMV1Cys-VLP-FLAG to display dual conjugations on the outer surface of the VLP
 - Successful assembly and patterning of TMV-*n*1Cys, VLP-*n*1Cys, TMV1Cys-TNT, and TMV1Cys-VLP-FLAG with and without protective metal coating
- **Selectively detection of Trinitrotoluene and FLAG antibody**

- Selective detection of TNT vapor was achieved on QCM's coated with TMV1Cys-TNT showing a 300% increase in resonant frequency compared to non-coated QCM's
- Successful ELISA on-a-chip was conducted using immobilized TMV1Cys-VLP-FLAG on microdisk resonators
- Immobilized TMV1Cys-VLP-FLAG on microdisk resonator were used to perform label-free immunoassays showing a shift in resonant frequency of 0.79 nm
- Negative shifts were observed when non-complementary antibodies and molecules were exposed to the sensor surface demonstrating its selectivity towards antibody FLAG

7.3 Future Outlook

Based on the experience gained during the development of these two hybrid technology platforms, key issues were identified for further improvement and possible segue to upcoming research projects. These aspects of the work range from optimizing the optical loss in the system to the integration of the sensor platform with a microfluidic system. These future focus areas are detailed in the following sub-sections.

7.3.1 Optimization of the Optical Resonator

As detailed in the dissertation, the sensitivity and the dynamic range of the sensor system is directly dependent on the quality of the optical resonator. The fabricated microdisk resonator was sensitive to detect the analyte for the targeted application. However, to further increase its detection limit and potential applications, the optical loss in the system needs to be minimized by decreasing the cavity's sidewall roughness. This can be accomplished by further fabrication optimization with a focus on improving the electron beam lithography. More etch resistant electron beam resist can be investigated to decrease the necessary resist thickness and ultimately increase the lithography resolution.

7.3.2 Sensor Array for Multiple Analyte Detection

The research that should be at the forefront of future activities is to take advantage of the TMV and VLP's ability to be modified and selectively patterned onto surfaces. These attributes allow for the realization of sensor arrays on a chip for paralleled sensing of different analytes. By expressing different functionalities on the surface of TMV-*n*1Cys or VLP-*n*1Cys, receptors with different affinities can be immobilized on different transducer surfaces on a single chip. The transduction mechanisms can still be based on optical resonators, due to their ability to be easily

arrayed and multiplexed. The figure below shows a conceptualization of such a sensor array chip system.

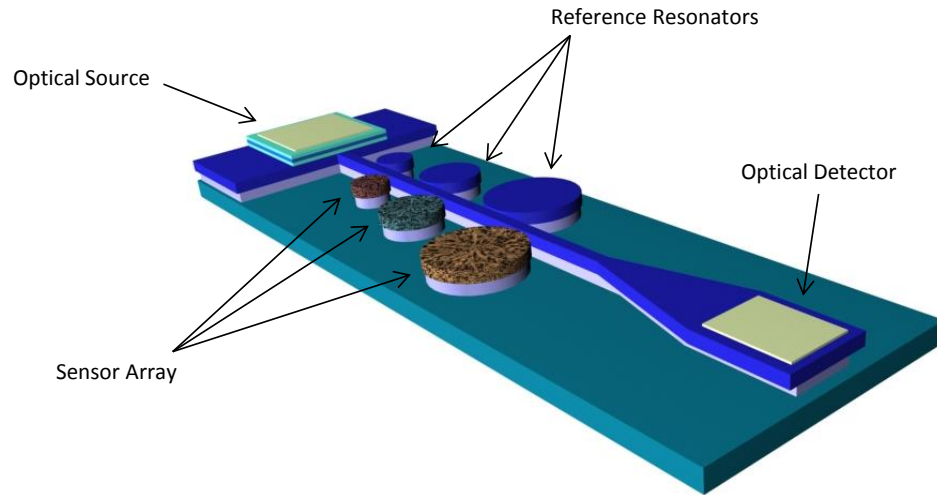


Figure 7-1 A CAD drawing showing an array of three sensors that can be monitored simultaneously for the selective detection of different analytes. Optoelectronics permitting, interrogation instruments can be integrated on-chip for remote sensing applications.

If optoelectronic technology can allow the integration of an optical source and a photodetector on a single chip, a standalone multi-sensor on-a-chip can be realized. Such sensor systems can be used for remote sensing and smart-dust applications.

7.3.3 Lab-on-a-Chip Applications with the Integration of Microfluidics

The limitation of the current system is its requisite to dehydrate the chip before optical interrogation due to the current optical setup. To enable real-time sensing in solution, microfluidics can be integrated on the top surface of the sensor platform. Fluidic micro-cavities or micro-channels would allow the introduction and manipulation of liquid solution to the surface of the resonators without affecting the optical testing schemes, (Figure 7-2).

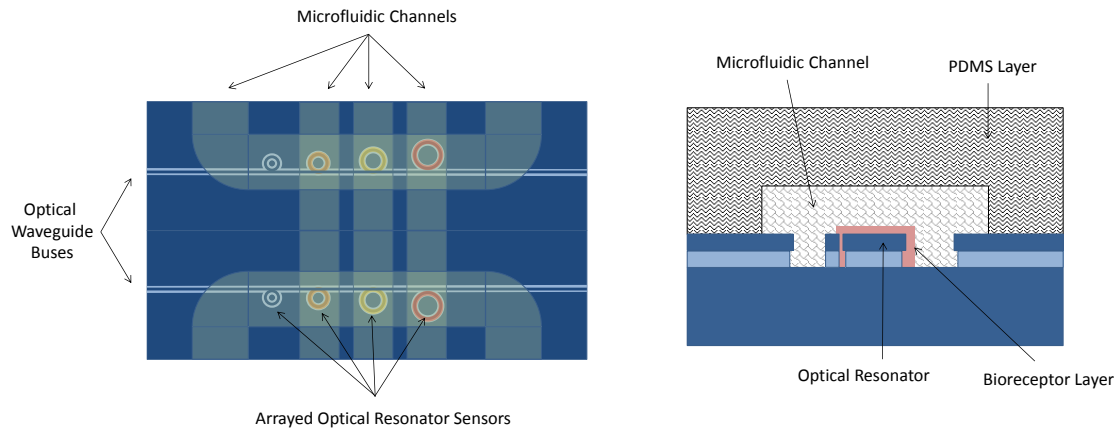


Figure 7-2 Diagrams showing (left) top view and (right) cross-section of an optical resonator array platform integrated with a microfluidic channel system

The integration of microfluidics would allow finer control of the sensing environment. Valved microchannels can be used to control the flow of analyte solutions and directed at a specific sensor module. Temporal modulation can also be controlled

using flow. Combinatorial studies are also a possibility. The greatest attribute of this sensor system is its robustness and compatibilities with different technologies.

Appendix A: Microfabrication Mask Designs

Electron Beam Dose Grid Array

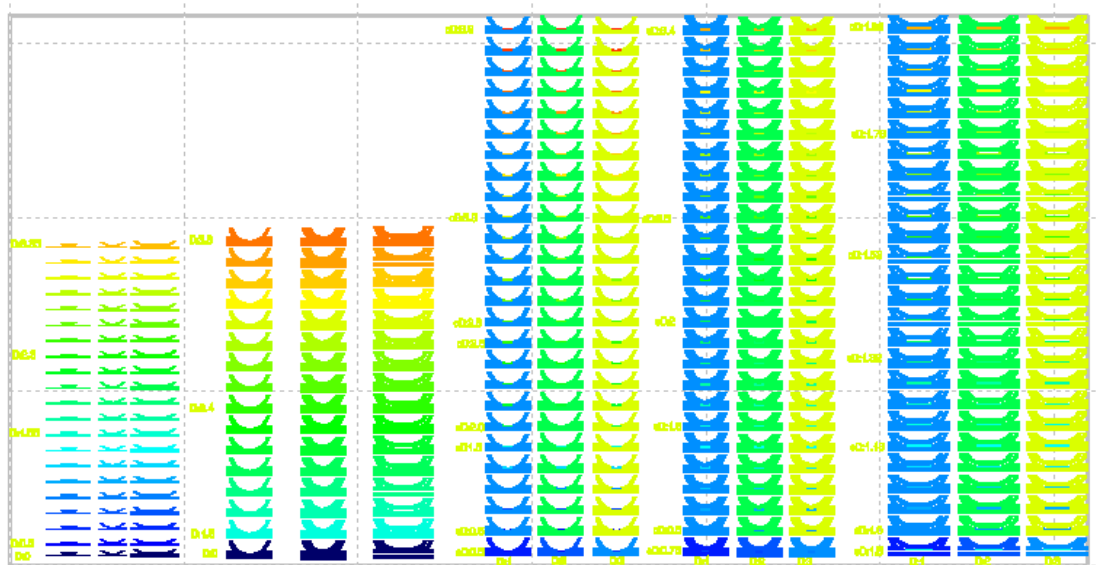


Figure A-3 Dose grid showing arrays of test structures, a portion of resonator designs, with incremental dosage settings as visualized with the color gradient. Test structures on the right show the dosage compensation in the coupling gap regions as evident by the non-homogenous colorings.

Electron Beam Resonator Array Write Pattern

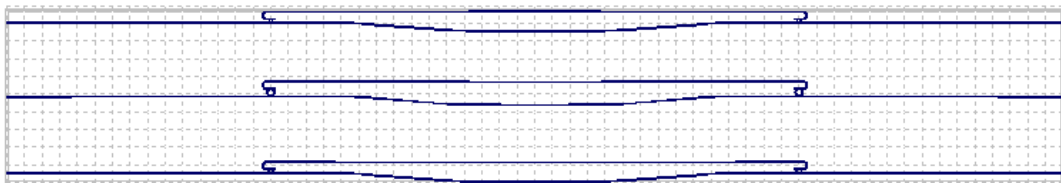


Figure A-4 Electron beam write pattern of six resonators on three parallel waveguides. The write pattern allows the design to be cleaved in half, creating two test chips with input and output ports on the edges of the chip.

Whispering Gallery Mode Resonator Designs

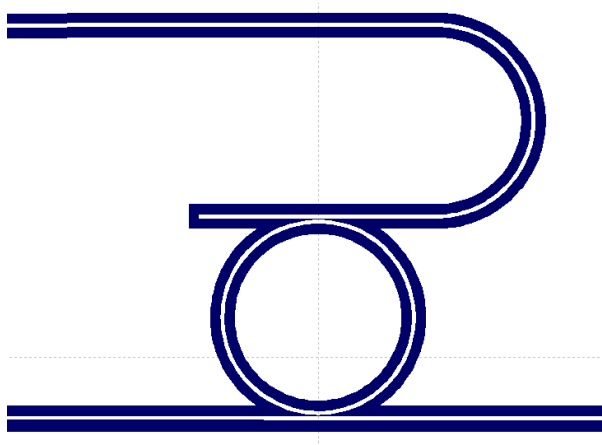


Figure A-5 Pattern of a microring resonator

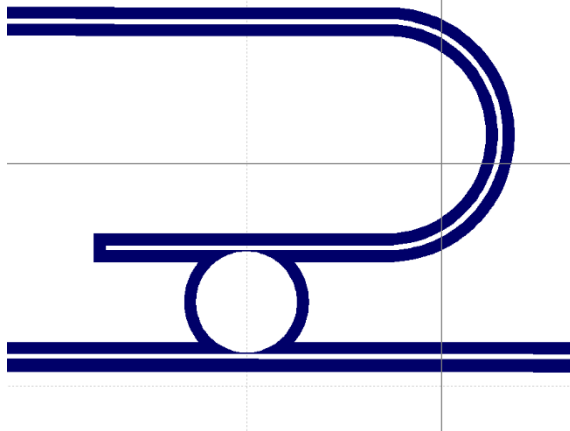


Figure A-6 Pattern of a microdisk resonator

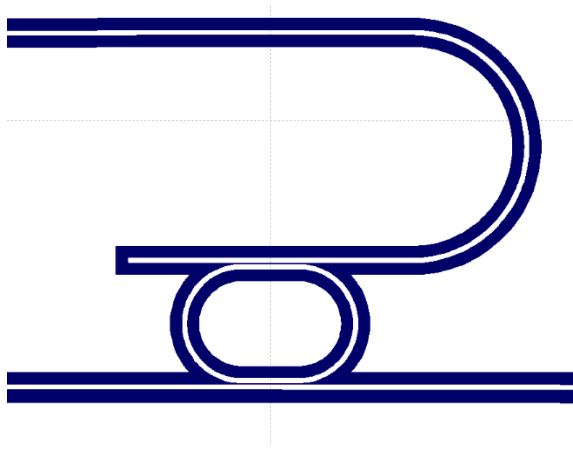


Figure A-7 Pattern of a racetrack resonator

Appendix B: Microfabrication Recipes

Deposition Recipes

Deposition of Silicon Oxide Cladding Layer

Tyster CVD Furnace

<i>Recipe</i>	Wet Ox with TLC-Anneal	
<i>Gases (sccm)</i>	O ₂	1000
	O ₂ /H ₂	185
<i>Temperature (°C)</i>	1050	
<i>Growth Time</i>	1.0 μm in 3 hours	

Deposition of Stoichiometric Nitride Waveguide Layer

Tyster CVD Furnace

<i>Recipe</i>	LPCVD Stoichiometric Silicon Nitride	
<i>Gases (sccm)</i>	NH ₃	75
	SiH ₂ Cl ₂	5
<i>Pressure (mTorr)</i>	300	
<i>Temperature (°C)</i>	770	
<i>Deposition Rate (Å/min)</i>	ca. 60	

Deposition of Silicon Oxide Hardmask Layer

Oxford PECVD (PlasmaSystem100)

<i>Recipe</i>	LPCVD Stoichiometric Silicon Nitride	
<i>Gases (sccm)</i>	SiH ₄	
	N ₂	

	N2O	
<i>Power (W)</i>		
<i>Pressure (mTorr)</i>	300	
<i>Temperature (°C)</i>	300	
<i>Deposition Rate (Å/min)</i>	ca. 400	

Etch Recipes

Chromium Hardmask Etch (I)

Oxford ICP Etcher (PlasmalabSystem 100)

<i>Recipe</i>	ghodssi-Cr etch	
<i>Hardmask</i>	Shipley 1813, PMMA A10	
<i>Carrier Wafer</i>	Chip on Quartz carrier plate (no bonding)	
<i>Gases (sccm)</i>	Cl ₂	25
	Ar	5
<i>Power (W)</i>	RF	30
	ICP	50 - 100
<i>Pressure (mTorr)</i>	5	
<i>Temperature (°C)</i>	20	
<i>Selectivity</i>	> 1:1.6	
<i>Etch Rate (Å/min)</i>	> 140	

Chromium Hardmask Etch (II)

Ion Mill (Oxford 200)

<i>Recipe</i>	N/A
---------------	-----

<i>Hardmask</i>	Shipley 1813, PMMA A10
<i>Current (mA/cm²)</i>	0.27
<i>Voltage (V)</i>	500
<i>Pressure (mTorr)</i>	< 5e-6
<i>Selectivity</i>	ca. 1:1
<i>Etch Rate (Å/min)</i>	110

Silicon Oxide Hardmask Etch

Plasma-therm RIE (Model 790)

<i>Recipe</i>	LPS-SIO2PT	
<i>Hardmask</i>	PMMA A10	
<i>RF Power (W)</i>	175	
<i>DC Bias (V)</i>	430	
<i>Gas (sccm)</i>	CHF ₃	20
	O ₂	20
<i>Pressure (mTorr)</i>	40	
<i>Etch Rate (Å/min)</i>	330	

Silicon Nitride Waveguide Layer Etch

Plasma-therm RIE (Model 790)

<i>Recipe</i>	LPS-DIELCUT
<i>Hardmask</i>	SiO ₂
<i>DC Bias (V)</i>	170

<i>Gas (sccm)</i>	SF6	19.86
<i>Pressure (mTorr)</i>	20	
<i>Etch Rate (Å/min)</i>	1360	

Silicon backside Etch

STS DRIE System

<i>Recipe</i>	UMHIGH			
<i>Hardmask</i>	N/A			
<i>Carrier Wafer</i>	Chip bounded to SiO ₂ coated Si wafer using Crystalbond™ wax			
<i>Gas (sccm)</i>	Etch		Passivation	
	SF ₆	130	C ₄ F ₈	85
	O ₂	13		
<i>ICP Power (W)</i>	600		600	
<i>RF Power (W)</i>	17		0	
<i>Cycle time (sec)</i>	15		2	
<i>Etch Rate (Å/min)</i>	ca. 40000			

Appendix C: Molecular Biology Engineering Protocols

Enzyme-Linked Immunosorbent Assay (ELISA)

- a. Blocking step:
 - 30 minutes at room temperature in 5% non-fat dry milk in Tris Buffer Solution (TBS) buffer (1 g of dry non-fat milk in 20 mL TBS)
- b. Primary antibody attachment
 - Add 1/1000 dilution of primary antibody serum in TBS and 5% nonfat dry milk for 2 hours at room temperature. 3 μ L of Anti-His into 20 mL of TBS and 1 g of dried non-fat milk.
- c. Rinse step:
 - Rinse in TBS 1 time
 - Rinse in TBS with 0.05% Tween 20 1 time
 - Rinse in TBS 2 times
- d. Secondary antibody (with enzyme) attachment
 - Add 1/5000 dilution of secondary antibody with enzyme serum in TBS and 5% nonfat dry milk for 2 hours at room temperature. 2 μ L of goat anti-rabbit alkaline phosphatase into 20 mL of TBS and 1 g of dried non-fat milk.
- e. Rinse step
- f. Enzyme substrate attachment
 - Transfer to 30 mL substrate buffer
 - Add a pinch of Nitro-BT
 - Add 100 μ L of 5-Bromo-4-chloro-3-indolyl phosphate (BCIP)

TMV-n1Cys-cTNT Purification

1. Materials

1.1 Plant Growth and Inoculation Materials

1. Tobacco seed (e.g. *Nicotiana benthamiana*). For TMV-n1Cys, *Nicotiana tabaccum* cv Xanthi are used. Additional tobacco cultivars can be substituted as long as they are listed as susceptible to TMV.
2. LCI Potting mixture and 4 inch pots.
3. Tobacco plants were maintained under growth chamber conditions at 28 °C with a 12-hour light/dark cycle.
4. Infectious TMV-n1Cys-cTNT cDNA clone as described by Royston et al [11].
5. Frog eye soup

1.2 Virus Purification Components

1. Virus extraction buffer [18]: 10 mM Na₂HPO₄, 10 mM EDTA, 1% ascorbic acid, 0.5 M DTT.
 - 970 mL of water in a 1 L flask
 - 10 mL of a 1 M stock solution of Na₂HPO₄
 - 20 mL of a 2 M stock solution of EDTA (pH8)
 - 10 g of ascorbic acid and 0.5 mL of a 1 M dithiothreitol
2. Resuspension buffer, 0.1 M (pH7) phosphate buffer:
 - 57.7 mL of 1 M Na₂HPO₄
 - 42.3 mL of 1M NaH₂PO₄
 - 900 mL H₂O to make 1 L
3. Cheesecloth or other similar loosely woven cotton fabric.
4. Blender
5. Chloroform
6. Polyethylene glycol 8000
7. Potassium chloride
8. Sucrose gradients (10-40%):
 - 50 g sucrose
 - 150 mL 0.1 M phosphate buffer

2. Methods

2.1 Virus production, inoculation, and harvesting

- Plant Production:

- Tobacco seeds are sown directly across the surface of a potting mixture and maintained at 28°C with a 12 h light/dark cycle
- Three to four weeks post germination the tobacco seedlings are transplanted into individual 4-inch pots and maintained for an additional four weeks prior to inoculation.
- Plant Inoculation
- Individual plant leaves are brushed with suspension of RNA construct in frog eye soup
- Plant leaves are covered with moist tissue to help heal overnight
- Post Inoculation
- Inoculated plants should be maintained until systematic infection signs are observed.
- Typically a light-green dark-green mosaic appeared on the newly emerging leaves. This usually occurs 2-4 weeks post-inoculation.
- Post signs of systematic infection, leaves are harvested and weighed
- Harvested leaves are then frozen at -20 °C or used immediately for extraction
- Stored frozen leaves for more than a year can be successfully purified

2.2 Purification of Virus from Plant Tissue

Day 1

1. Blend 100 g to 200 g of freshly harvested or frozen infected leaf tissue with 0.5 L to 1 L of phosphate extraction buffer until smooth. This breaks up the leaf cells and releases the virus into solution.
2. Drape four layers of cheesecloth over the top of a 1 L beaker and strain the blended mixture by pouring it through cheesecloth and allowing it to drain. The cloth and trapped plant pulp can be squeezed firmly within the cheesecloth and blended a second time with phosphate extraction buffer to obtain additional extract.
3. Divide the plant extract into 250 mL polypropylene centrifuge bottles by pouring ~200 mL of the filtered extraction liquid into each bottle.
4. Add 20 mL chloroform per bottle for a final mixture of 10% chloroform by volume. Shake vigorously by hand or machine for 10 min. The chloroform will remove organic soluble plant membranes and pigments. Keep bottle on ice if possible.
5. Centrifuge the samples for 10 min at 17,000 g and at 4 °C.
6. Collect and filter the supernatant into a 1 L graduated cylinder by pouring the upper phase supernatant through two layers of KimWipes placed within a funnel atop

the cylinder. Care should be taken to avoid pouring any of the chloroform layer into the cylinder.

7. Transfer the supernatant to a 1-2 L flask and add 6% (w/v) polyethylene glycol 8000 (PEG) and 1.5% KCl (e.g. for 1 L of fluid, add 60 g PEG and 15 g KCl).
8. Cover the flask and stir at a medium speed at 4 °C for 45-60 min. Addition of PEG results in the virus precipitation.
9. Distribute the suspension into 250 mL polypropylene centrifuge bottles and centrifuge at 17,000 g for 10 min.
10. Pour off the supernatant from each bottle, retaining the virus pellet. To each pellet, add ~3 mL pH7 phosphate buffer and resuspend overnight at 4 °C with gentle agitation.

Day 2

1. Thaw premade frozen sucrose gradients at room temperature.
2. To each gradient, gently layered 2-3 mL of the resuspended PEG virus pellet to the top of the gradient. Use of a wide bore pipette tip will aid in applying the suspension without disturbing the gradient.
3. Centrifuge at 91,000 g at 14°C for 2 hours. The virus will form a translucent band approximately half way down the gradient.
4. Use a syringe remove the virus band from each gradient and transfer it to ultra-centrifuge bottles. Dilute and balance the samples with additional pH 7 phosphate buffer.
5. Centrifuge at 92,000 g at 4 °C for 2 hours to pellet the virus.
6. Pour off supernatant and resuspend the pellet in (.2-1 mL) pH 7 phosphate buffer overnight at 4 °C on a rocker.

TMV1Cys-VLP-FLAG *Purification*

1. Materials

1.1 Bacterial Growth and Induction

1. Coat protein expression constructs in BL21 competent *E. coli* K-12
1. 2.Lysogeny (LB) broth media (25 g of LB powder in 1 L of DI water)
2. Ampicilin 100 µg/mL
3. Chloramphenicol (50 µg/mL)
4. 0.1 mM Isopropyl β-D-1-thiogalactopyranoside (IPTG)

1.2 Virus Purification Components

1. Bugbuster™ (Novagen, Madison WI) (2.5 mL per 50 mL of cell culture)
2. Lysonase™ Bioprocessing reagent (Novagen, Madison WI) (1 µL per 50 mL of cell culture)
3. Dithiothreitol (DTT)
4. Chloroform
5. Polyethylene glycol 8000
6. Potassium chloride
7. Resuspension buffer, 0.1 M (pH7) phosphate buffer:
 - 57.7 mL of 1 M Na₂HPO₄
 - 42.3 mL of 1M NaH₂PO₄
 - 900 mL H₂O to make 1 L
8. Sucrose gradients (10-40%):
 - 50 g sucrose
 - 150 mL 0.1 M phosphate buffer

2. Methods

2.1 VLP production

Bacterial growth:

Day 1

1. A few microliters of BL21 competent *E. Coli* K-12 with VLP constructs are obtained from freezer stocks maintained at -80°C and added to 5 mL of LB media in a glass test tube
2. 100 µg/mL of ampicillin and 50 µg/mL of chloramphenicol were added to the bacterial solution and then incubated on a shaker overnight at 37°C

Day 2

3. 2 mL of the bacterial culture are added to a fresh 50 mL LB media solution in an Erlenmeyer flask, along with 100 µg/mL of ampicillin and 50 µg/mL of chloramphenicol
4. The bacterial culture was incubated at 37°C on a shaker until its optical density reached 0.5 at 600nm
5. 0.1 mM of IPTG is added to the solution to commence induction

6. Induction occurs on a shaker overnight (or at least 5 hours) at room temperature

Day 3

7. Induced cells are collected in plastic tubes by centrifugation for 10 minutes at 17,000 x g at 4°C

2.2 VLP Purification

Day 1

1. 2.5 mL of Bugbuster™ and 1.0 µL of Lysonase™ were added to the cell paste and vortexed and placed in a rotisserie spinner for 30-60 minutes at room temperature
2. 0.5 mM DTT was added to the cell lysates and sonicated for 3-5 minutes at room temperature
3. Transfer sample to Eppendorf tube and centrifuged for 1 minute at 1000 x g at room temperature
4. Transfer supernatant into a 250 mL polypropylene centrifuge bottle fill to the top with 0.1M pH 7 phosphate buffer
5. Centrifuge at 17,000 g for 30 minutes
6. Pour off the supernatant from each bottle, retaining the VLP pellet. To each pellet, add ~1 mL pH7 phosphate buffer and resuspend overnight at 4 °C with gentle agitation

Day 2

7. Thaw premade frozen sucrose gradients at room temperature.
8. To each gradient, gently layered 1 mL of the resuspended VLP pellet to the top of the gradient. Use of a wide bore pipette tip will aid in applying the suspension without disturbing the gradient.
9. Centrifuge at 91,000 g at 14°C for 1 hour. The virus will form a translucent band approximately half way down the gradient.
10. Use a syringe remove the virus band from each gradient and transfer it to ultra-centrifuge bottles. Dilute and balance the samples with additional pH 7 phosphate buffer.
11. Centrifuge at 92,000 g at 4 °C for 1 hour to pellet the virus.
12. Pour off supernatant and resuspend the pellet in (.2-1 mL) pH 7 phosphate buffer or DI overnight at 4 °C on a rocker.

Bibliography

- [1] S. H. Lee, D. D. Stubbs, W. D. Hunt, and P. J. Edmonson, "Vapor Phase Detection of Plastic Explosives Using a SAW Resonator Immunosensor Array," in *IEEE Sensors 2005*, 2005, pp. 468-471.
- [2] W. Lukosz, "Principles and sensitivities of integrated optical and surface plasmon sensors for direct affinity sensing and immunosensing," *Biosensors & bioelectronics*, vol. 6, pp. 215-225.
- [3] B. Liedberg, C. Nylander, and I. Lundstrom, "Biosensing with surface plasmon resonance--how it all started," *Biosensors & bioelectronics*, vol. 10, pp. i-ix, 1995.
- [4] R. J. Green, R. A. Frazier, B. M. Shakesheff, M. C. Davies, C. J. Roberts, and S. J. B. Tendler, "Surface plasmon resonance analysis of dynamic biological interactions with biomaterials," *Biomaterials*, vol. 21, pp. 1823-1835, 2000.
- [5] G. Liu, M. D. Porter, G. J. Bastiaans, and S. Burns, "A Smart H₂ Sensor Array of QCMs coated with PdNi Alloy of Various thicknesses," in *1995 IEEE International Frequency Control Symposium*, 1995, pp. 876-878.
- [6] I. Voiculescu, M. E. Zaghloul, R. A. McGill, E. J. Houser, and G. K. Fedder, "Electrostatically Actuated Resonant Microcantilever Beam in CMOS Technology for the Detection of Chemical Weapons," *IEEE Sensors Journal*, vol. 5, pp. 641-647, August 2005.
- [7] N. Siwak, X. Z. Fan, D. Hines, S. Kanakaraju, N. Godsmann, and R. Ghodssi, "Inidum Phosphide MEMS Cantilever resonator Sensors Utilizing a Pentacene Absorption Layer," *Journal of Microelectromechanical Systems*, vol. 18, pp. 103-110, February 2009 2009.
- [8] F. Lochon, L. Fadel, I. Dufour, D. Rebière, and J. Pistré, "Silicon made resonant microcantilever- Dependence of the chemical sensing performances on the sensitive coating thickness," *Materials Science and Engineering C*, vol. 26, pp. 348-353, 2006.
- [9] N. V. Lavrik, M. J. Sepaniak, and P. G. Datskosa, "Cantilever transducers as a platform for chemical and biological sensors," *Review of Scientific Instruments*, vol. 75, pp. 2229-53, July 2004 2004.

- [10] S. T. Koev, R. Fernandes, W. E. Bentley, and R. Ghodssi, "A Cantilever Sensor With an Integrated Optical Readout for Detection of Enzymatically Produced Homocysteine," *IEEE Transactions on Biomedical Circuits and Systems*, vol. 3, pp. 415-423, 2009.
- [11] R. Berger, C. Gerber, H. P. Lang, and J. K. Gimzewski, "Micromechanics: a toolbox for femtoscale science: "Towards a laboratory on a tip"," *Microelectronic Engineering*, vol. 35, pp. 373-379, Feb. 1997.
- [12] D. R. Baselt, B. Gruhberger, E. Klaassen, S. Cemalovic, C. L. Britton Jr., S. V. Patel, T. E. Mlsna, D. McCorkle, and B. Warmack, "Design and performance of a microcantilever-based hydrogen sensor," *Sensors and Actuators B*, vol. 88, pp. 120-131, September 13, 2002 2003.
- [13] X. Z. Fan, N. Siwak, S. Kanakaraju, C. Richardson, and R. Ghodssi, "A Chemical Sensing Microsystem Utilizing an Adaptive Feedback Circuit," in *The 15th International Conference on Solid-State Sensors, Actuators, and Microsystems (Transducers '09)*, Denver, CO, 2009.
- [14] B. Illic, H. G. Craighead, S. Krylov, W. Senaratne, and C. Ober, "Attogram Detection using Nanoelectromechanical Oscillators," *J. Applied Physics*, vol. 95, pp. 3694-703, 2004.
- [15] X. Fan, I. M. White, H. Zhu, J. D. Suter, and H. Oveys, "Overview of novel integrated optical ring resonator bio/chemical sensors," in *SPIE*, 2007, pp. 64520M 1-20.
- [16] I. M. White and X. Fan, "On the performance quantification of resonant refractive index sensors," *Optics Express*, vol. 16, pp. 1020-1028, January 21, 2008 2008.
- [17] E. R. Goldman, M. P. Pazirandeh, J. M. Mauro, K. D. King, J. C. Frey, and G. P. Anderson, "Phage-displayed peptides as biosensor reagents," *J Mol Recognit*, vol. 13, pp. 382-7, Nov-Dec 2000.
- [18] Z. Han, G. Su, and C. Huang, "Screening and identification of receptor antagonist for shiga toxin from random peptides displayed on filamentous bacteriophages," *Sci China C Life Sci*, vol. 42, pp. 43-9, Feb 1999.
- [19] C. Mao, A. Liu, and B. Cao, "Virus-based chemical and biological sensing," *Angew Chem Int Ed Engl*, vol. 48, pp. 6790-810, 2009.
- [20] M. Paschke, "Phage display systems and their applications," *Appl Microbiol Biotechnol*, vol. 70, pp. 2-11, Mar 2006.

- [21] V. A. Petrenko and V. J. Vodyanoy, "Phage display for detection of biological threat agents," *J Microbiol Methods*, vol. 53, pp. 253-62, May 2003.
- [22] L. Q. Wu and G. F. Payne, "Biofabrication: using biological materials and biocatalysts to construct nanostructured assemblies," *Trends Biotechnol*, vol. 22, pp. 593-9, Nov 2004.
- [23] M. Kitsara, D. Goustouridis, S. Chatzandroulis, M. Chatzichristidi, I. Raptis, T. Ganetsos, R. Igreja, and C. J. Dias, "Single chip interdigitated electrode capacitive chemical sensor arrays," *Sensors and Actuators B*, vol. 127, pp. 186-192, 2007.
- [24] E. S. Snow, F. K. Perkins, E. J. Houser, S. C. Badescu, and T. L. Reinecke, "Chemical detection with a single-walled carbon nanotube capacitor," *Science*, vol. 307, pp. 1942-5, 25 March
- [25] M. C. Horrillo, J. Lozano, M. J. Fernandez, J. L. Fontecha, M. Aleixandre, J. P. Santos, I. Sayago, T. Arroyo, J. M. Cabellos, and F. J. Gutierrez, "Wine classification with a zinc oxide SAW sensor array " *Sensors and Actuators B (Chemical)*, vol. 120, pp. 166-171, Dec 14 2006.
- [26] J. M. Corres, F. J. Arregui, and I. R. Matias, "Design of humidity sensors based on tapered optical fibers," *Journal of Lightwave Technology*, vol. 24, p. 4329, 2006.
- [27] A. Cusano, A. Iadicicco, S. Campopiano, A. Cutolo, and M. Giordano, "Self temperature referenced refractive index sensor by non-uniform thinned fiber Bragg gratings," *Sensors and Actuators B (Chemical)*, vol. 120, p. 231, 2006.
- [28] M. A. Haidekker, W. J. Akers, D. Fischer, and E. A. Theodorakis, "Optical fiber-based fluorescent viscosity sensor," *Optics Letters*, vol. 31, p. 2529, 2006.
- [29] S. Li-Yang, A. P. Zhang, L. Wei-Sheng, F. Hong-Yan, and H. Sailing, "Optical refractive-index sensor based on dual fiber-Bragg gratings interposed with a multimode-fiber taper," *IEEE Photonics Technology Letters*, vol. 19, p. 30, 2007.
- [30] D. Yixiang and C. Wenqing, "Optical fiber-based evanescent ammonia sensor," *Sensors and Actuators B (Chemical)*, vol. 110, p. 252, 2005.
- [31] H. C. Nathanson, W. E. Newell, R. A. Wickstrom, and R. J. J. Davis, "The resonant gate transistor," *IEEE Transactions on Electron Devices*, vol. ED-14, pp. 117-133, March 1967 1967.
- [32] R. T. Howe and R. S. Muller, "Resonant microbridge vapor sensor," *IEEE Transactions on Electron Devices*, vol. ED-33, pp. 499-506, 1986.

- [33] J. A. Covington, J. W. Gardner, D. Briand, and N. F. d. Rooij, "A polymer gate FET sensor array for detecting organic vapours," *Sensors and Actuators B*, vol. 77, pp. 155-162, 2001.
- [34] H. Chang and J. Li, "Electrochemical impedance probing of transcriptional TATA binding protein based on TATA box site-specific binding," *Electrochemistry Communications*, vol. 11, pp. 2101-2104, 2009.
- [35] X. Xu, S. Zhang, H. Chen, and J. Kong, "Integration of electrochemistry in micrototal analysis systems for biochemical assays: Recent developments," *Talanta*, vol. 80, pp. 8-18, 2009.
- [36] Y. Ma, K. Jiao, T. yang, and D. Sun, "Sensitive PAT gene sequence detection by nano-SiO₂/p-aminothiophenol self-assembled films DNA electrochemical biosensor based on impedance measurement," *Sensors and Actuators B*, vol. 131, pp. 565-571, 2008.
- [37] Y. T. Yang, C. Callegari, X. L. Feng, K. L. Ekinici, and M. L. Roukes, "Zeptogram-Scale Nanomechanical Mass Sensing," *Nano Letters*, vol. 6, pp. 583-586, 2006/04/01 2006.
- [38] K. L. Ekinici and M. L. Roukes, "Nanoelectromechanical systems," *Review of Scientific Instruments*, vol. 76, pp. 061101-061101-12, 2005.
- [39] D. L. DeVoe, "Piezoelectric thin film micromechanical beam resonators," *Sensors and Actuators A: Physical*, vol. 88, pp. 263-272, 2001.
- [40] J. S. Bunch, A. M. van der Zande, S. S. Verbridge, I. W. Frank, D. M. Tanenbaum, J. M. Parpia, H. G. Craighead, and P. L. McEuen, "Electromechanical Resonators from Graphene Sheets," *Science*, vol. 315, pp. 490-493, January 26, 2007 2007.
- [41] C. Sang-Yeon, G. Dobbs, N. M. Jokerst, B. Mizaikoff, and T. Cooper, "Optical Microring Resonator Sensors with Selective Membrane Surface Customization," in *Lasers and Electro-Optics, 2007. CLEO 2007. Conference on*, 2007, pp. 1-2.
- [42] B. Cunningham, M. Weinberg, J. Pepper, C. Clapp, R. Bousquet, B. Hugh, R. Kant, C. Daly, and E. Hauser, "Design, fabrication and vapor characterization of a microfabricated flexural plate resonator sensor and application to integrated sensor arrays," *Sensors and Actuators B: Chemical*, vol. 73, pp. 112-123, 2001.
- [43] M. Benetti, D. Cannata, F. Di Pietrantonio, V. Foglietti, and E. Verona, "Microbalance chemical sensor based on thin-film bulk acoustic wave resonators," *Applied Physics Letters*, vol. 87, pp. 173504-173504-3, 2005.

- [44] A. Ksendzov and Y. Lin, "Integrated optics ring-resonator sensors for protein detection," *Optics Letters*, vol. 30, pp. 3344-3346, December 15, 2005 2005.
- [45] A. Ksendzov, M. L. Homer, and A. M. Manfreda, "Integrated optics ring-resonator chemical sensor with polymer transduction layer," *Electronics Letters*, vol. 40, January 8, 2004 2004.
- [46] R. Bashir, "Microresonator mass sensors for detection of Bacillus anthracis Sterne spores in air and water," *Biosensors & bioelectronics*, vol. 22, p. 3028, 2007.
- [47] G. N. D. Brabander, J. T. Boyd, and G. Beheim, "Integrated Optical Ring Resonator With Micromechanical Diaphragm for Pressure Sensing," *IEEE Photonics Technoogy Letters*, vol. 6, pp. 671-673, May 1994 1994.
- [48] F. Pang, X. Han, F. Chu, J. Geng, H. Cai, R. Qu, and Z. Fang, "Sensitivity to alcohols of planar waveguide ring resonator fabricated by a sol-gel method," *Sensors and Actuators B*, vol. 120, pp. 610-614, May 12, 2006 2007.
- [49] N. M. Hanumegowda, I. M. White, and X. Fan, "Aqueous mercuric ion detection with microsphere optical ring resonator sensors," *Sensors and Actuators B*, vol. 120, pp. 207-212, March 15, 2006 2006.
- [50] H. J. Patrick, G. M. Williams, and A. M. Vengsarkar, "Hybrid Bragg Grating/Long Period Fiber Grating Sensor for Strain/Temperature Discrimination," *Photonic Technology Letters*, vol. 8, p. 1223, 1996.
- [51] G. Z. Xiao, P. Zhao, F. G. Sun, Z. G. Lu, Z. Zhang, and C. P. Grover, "Interrogating fiber Bragg grating sensors by thermally scanning a demultiplexer based on arrayed waveguide gratings," *Optics Letters*, vol. 29, pp. 2222-2224, 2004/10/01 2004.
- [52] Y. Sano and T. Yoshino, "Fast optical wavelength interrogator employing arrayed waveguide grating for distributed fiber Bragg grating sensors," *Lightwave Technology, Journal of*, vol. 21, pp. 132-139, 2003.
- [53] A. Kersey, M. A. Davis, H. J. Patrick, M. Leblanc, K. P. Koo, C. G. Askins, M. A. Putnam, and E. J. Friebele, "Fiber grating sensors," *Lightwave Technology, Journal of*, vol. 15, pp. 1442-1463, 1997.
- [54] E. J. A. Pope, "Fiber optic chemical microsensors employing optically active silica microspheres," 1995, pp. 245-256.
- [55] M. Köhl, "Optical Microsensors for Analysis of Microbial Communities," in *Methods in Enzymology*. vol. Volume 397, R. L. Jared, Ed., ed: Academic Press, 2005, pp. 166-199.

- [56] H. Beyenal, C. Yakymyshyn, J. Hyungnak, C. C. Davis, and Z. Lewandowski, "An optical microsensor to measure fluorescent light intensity in biofilms," *Journal of Microbiological Methods*, vol. 58, pp. 367-374, 2004.
- [57] K. J. Albert and D. R. Walt, "High-Speed Fluorescence Detection of Explosives-like Vapors," *Analytical Chemistry*, vol. 72, pp. 1947-1955, 2000/05/01 2000.
- [58] T. J. Harpster, B. Stark, and K. Najafi, "A passive wireless integrated humidity sensor," *Sensors and Actuators A: Physical*, vol. 95, pp. 100-107, 2002.
- [59] T. Someya, J. Small, P. Kim, C. Nuckolls, and J. T. Yardley, "Alcohol Vapor Sensors Based on Single-Walled Carbon nanotube Field Effect Transistors," *Nano Letters*, vol. 3, pp. 877-881, 2003.
- [60] C. Staii and A. T. Johnson, "DNA-Decorated Carbon Nanotubes for Chemical Sensing," *Nano Letters*, vol. 5, pp. 1774-1778, 2005.
- [61] H. Ben-Yoav, P. H. Dykstra, W. E. Bentley, and R. Ghodssi, "A microfluidic-based electrochemical biochip for label-free diffusion-restricted DNA hybridization analysis," *Biosensors and Bioelectronics*, vol. 38, pp. 114-120, 2012.
- [62] Q.-M. Wang and L. E. Cross, "Performance analysis of piezoelectric cantilever bending actuators," *Ferroelectrics*, vol. 215, pp. 187-213, 1998.
- [63] W. P. Eaton and J. H. Smith, "Micromachined pressure sensors: review and recent developments," *Smart Materials and Structures*, vol. 6, pp. 530-539, 1997.
- [64] E. Benes, M. Groschi, W. Burger, and M. Schmid, "Sensors based on piezoelectric resonators," *Sensors and Actuators A: Physical*, vol. 48, pp. 1-21, 1995.
- [65] J. W. Judy and R. S. Muller, "Magnetic microactuation of torsional polysilicon structures," *Sensors and Actuators A: Physical*, vol. 53, pp. 392-397, 1996.
- [66] I. Glassman, *Combustion*: Academic Press, 1996.
- [67] Y. Sun, S. I. Shopova, G. Frye-Mason, and X. Fan, "Rapid chemical vapor sensing using optofluidic ring resonators," *Optics Letters*, vol. 33, pp. 788-790, April 15, 2008 2008.
- [68] M. Loncar, A. Scherer, and Y. Qiu, "Photonic crystal laser sources for chemical detection," *Applied Physics Letters*, vol. 82, pp. 4648-4650, 2003.

- [69] R. J. Green, R. A. Frazier, K. M. Shakesheff, M. C. Davies, C. J. Roberts, and S. J. B. Tendler, "Surface plasmon resonance analysis of dynamic biological interactions with biomaterials," *Biomaterials*, vol. 21, pp. 1823-1835, 2000.
- [70] L. Rayleigh, "The Problem of the Whispering Gallery," *Scientific Papers*, vol. 5, pp. 617-620, 1912.
- [71] C. F. Carlborg, K. B. Gylfason, A. Kazmierczak, F. Dortu, M. J. Banuls Polo, A. Maquieira Catala, G. M. Kresbach, H. Sohlstrom, T. Moh, L. Vivien, J. Popplewell, G. Ronan, C. A. Barrios, G. Stemme, and W. van der Wijngaart, "A packaged optical slot-waveguide ring resonator sensor array for multiplex label-free assays in labs-on-chips," *Lab on a Chip*, vol. 10, pp. 281-290, 2010.
- [72] H. Zhu, I. M. White, J. D. Suter, M. Zourob, and X. Fan, "Opto-fluidic micro-ring resonator for sensitive label-free viral detection," *The Analyst*, vol. 133, pp. 356-360, January 8, 2008 2007.
- [73] H. Zhu, I. M. White, J. D. Suter, P. S. Dale, and X. Fan, "Analysis of biomolecule detection with optofluidic ring resonator sensors," *Optics Express*, vol. 15, pp. 9139-9146, July 23, 2007 2007.
- [74] I. M. White, H. Oveys, and X. Fan, "Liquid-core optical ring resonator sensors," *Optics Letters*, vol. 31, pp. 1319-1321, May 1, 2006 2006.
- [75] W. Shin, M. Matsumiya, N. Izu, and N. Murayama, "Hydrogen-selective thermoelectric gas sensor," *Sensors and Actuators B*, vol. 93, pp. 304-308, 2003.
- [76] Y.-H. Kim, K. Jang, Y. J. Yoon, and Y.-J. Kim, "A novel relative humidity sensor based on microwave resonators and a customized polymeric film," *Sensors and Actuators B*, vol. 117, pp. 315-322, 2006.
- [77] S. Ashkenazi, C.-Y. Chao, and L. J. Guo, "Ultrasound detection using polymer microring optical resonator," *Applied Physics Letters*, vol. 85, pp. 5418-5420, November 29, 2004 2004.
- [78] C. Y. Chao and L. J. Guo, "Biochemical sensors based on polymer microrings with sharp asymmetrical resonance," *Applied Physics Letters*, vol. 83, pp. 1527-1529, August 25, 2003 2003.
- [79] K. D. Vos, I. Bartolozzi, E. Schacht, P. Bienstman, and R. Baets, "Silicon-on-Insulator microring resonator for sensitive and label-free biosensing," *Optics Express*, vol. 15, pp. 7610-7615, June 11, 2007 2007.
- [80] A. Yalcin, K. C. Popat, J. C. Aldridge, T. A. Desai, J. Hryniewicz, N. Chbouki, B. E. Little, O. King, V. Van, S. Chu, D. Gill, M. Anthes-Washburn, M. S. unlu,

- and B. B. Goldberg, "Optical Sensing of Biomolecules Using Microring Resonators," *IEEE Journal of Selected Topics in Quantum Electronics*, vol. 12, pp. 148-155, January/February 2006 2006.
- [81] V. M. N. Passaro, F. Dell'Olio, and F. D. Lenardis, "Ammonia Optical Sensing by Microring Resonators," *Sensors*, vol. 7, pp. 2741-2749, November 15, 2007 2007.
 - [82] J. Hryniewicz, N. Chbouki, B. Little, O. King, V. Van, S. Chu, and D. Gill, "Micro-Ring Resonators: The Promise of a Powerful Biochemical Sensor Platform," in *LEOS Summer Topical Meetings 2004*, 2004.
 - [83] L. Durrer, T. Helbling, C. Zenger, A. Jungen, C. Stampfer, and C. Hierold, "SWNT growth by CVD on Ferritin-based iron catalyst nanoparticles towards CNT sensors," *Sensors and Actuators B*, vol. 132, pp. 485-490, 2008.
 - [84] K. Kordas, A. E. Pap, J. Vahakangas, A. Uusimaki, and S. Leppavuori, "Carbon nanotube synthesis on oxidized porous silicon," *Applied Surface Science*, vol. 252, pp. 1471-1475, 2005.
 - [85] S. Sun, D. Yang, G. Zhang, E. Sacher, and J.-P. Dodelet, "Synthesis and Characterization of Platinum Nanowire-Carbon Nanotube Heterostructures," *Chem. Mater.*, vol. 19, pp. 6376-6378, Nov 27 2007.
 - [86] J. H. Wang, P. Y. Su, M. Y. Lu, L. J. Chen, C. H. Chen, and C. J. Chu, "Synthesis of Cu Nanotubes with Silicon Oxide Nanowire Templates by MOCVD," *Electrochemical and Solid-State Letters*, vol. 8, pp. C9-C11, Nov 22 2005.
 - [87] B. Xiang, P. Wang, X. Zhang, S. A. Dayeh, D. P. R. Aplin, C. Soci, D. Yu, and D. Wang, "Rational Synthesis of p-type Zinc Oxide Nanowire Arrays Using Simple Chemical Vapor Deposition " *Nano Letters*, vol. 7, pp. 323-328, 2007.
 - [88] X. Feng, K. Shankar, O. K. Varghese, M. Paulose, T. J. Latempa, and C. A. Grimes, "Vertically Aligned Single Crystal TiO Nanowire Arrays Grown Directly on Transparent Conducting Oxide Coated Glass: Synthesis Details and Applications," *Nano Letters*, vol. 8, pp. 3781-3786, 2008.
 - [89] Y. Zhao, J. Jin, and X. Yang, "Hydrothermal synthesis of titanate nanowire arrays," *Materials Letters*, vol. 61, pp. 384-388, Apr 9 2007.
 - [90] T. Ghoshal, S. Biswas, S. Kar, A. Dev, S. CHakrabarti, and S. Chaudhuri, "Direct synthesis of ZnO nanowire arrays on Zn foil by a simple thermal evaporation process," *Nanotechnology*, Nov 22 2007.

- [91] S. O'Brien, L. Brus, and C. B. Murray, "Synthesis of Monodisperse Nanoparticles of Barium Titanate: Toward a Generalized Strategy of Oxide Nanoparticle Synthesis," *J. Am. Chem. Soc.*, vol. 123, pp. 12085-12086, Nov 7 2001.
- [92] X. Wang, X. Wang, W. Huang, P. J. Sebastian, and S. Gamboa, "Sol-gel template synthesis of highly ordered MnO₂ nanowire arrays," *Journal of Power Sources*, vol. 140, pp. 211-215, Jul 28 2005.
- [93] M. C. Kum, B. Y. Yoo, Y. W. Rheem, K. N. Bozhilov, W. Chen, A. Mulchandani, and N. V. Myung, "Synthesis and characterization of cadmium telluride nanowire," *Nanotechnology*, vol. 19, June 6 2008.
- [94] G. H. Yue, P. X. Yan, X. Y. Fan, M. X. Wang, D. M. Qu, D. Yan, and J. Z. Liu, "Characterization of the single crystalline iron sulfide nanowire array synthesis by pulsed electrodeposition," *Journal of Applied Physics*, Dec 27 2006.
- [95] L. Zhixun, F. Yan, Z. Xiaofang, and Y. Jiannian, "Synthesis of highly ordered Iron/Cobalt nanowire arrays in AAO templates and their structural properties," *Materials of Chemistry and Physics*, vol. 107, pp. 91-95, Jun 20 2008.
- [96] N. Ma, E. H. Sargent, and S. O. Kelley, "Biotemplated nanostructures: directed assembly of electronic and optical materials using nanoscale complementarity" *Journal of Materials Chemistry*, vol. 18, pp. 954-964, 2007.
- [97] S. Sotiropoulou, Y. Sierra-Sastre, S. S. Mark, and C. A. Batt, "Biotemplated Nanostructured Materials," *Chem. Mater.*, vol. 20, pp. 821-834, Jan 17 2008.
- [98] Q. Gu, C. Cheng, T. Gonela, S. Suryanarayanan, S. Anabathula, K. Dai, and D. T. Haynie, "DNA nanowire fabrication," *Nanotechnology*, vol. 17, pp. R14-R25, 2006.
- [99] Z. Deng and C. Mao, "DNA- Templated Fabrication of 1D Parallel and 2D Crossed Metallic Nanowire Arrays," *NANO Letters*, vol. 3, pp. 1545-1548, Sept 30 2003.
- [100] Y. Hashimoto, Y. Matsuo, and K. Ijio, "Fabrication of Silver Nanowires by Selective Electroless Plating of DNA Stretched Using the LB Method," *Chemistry Letters*, vol. 34, 2005.
- [101] J. M. Kinsella and A. Ivanisevic, "DNA-Templated Magnetic Nanowires with Different Compositions: Fabrication and Analysis," *Langmuir*, vol. 23, pp. 3886-3890, 2007.

- [102] H. Kudo and M. Fujihira, "DNA-Templated Copper Nanowire Fabrication by a Two-Step Process Involving Electroless Metallization," *IEEE Transactions on Nanotechnology*, vol. 5, pp. 90-92, March 2006.
- [103] Y. Ma, J. Zhang, G. Zhang, and H. He, "Polyaniline Nanowires on Si Surfaces Fabricated with DNA Templates," *J. Am. Chem. Soc.*, vol. 126, pp. 7097-7101, 2004.
- [104] K. Keren, M. Krueger, R. Gilad, G. Ben-Yospeh, U. Sivan, and E. Braun, "Sequence-Specific Molecular Lithography on Single DNA Molecules," *Science Magazine*, vol. 297, Jul 5 2002.
- [105] X. Liang, J. Liu, S. Li, Y. Mei, and W. Yanqing, "Magnetic and mechanical properties of micro/nano particles prepared by metallizing rod-shaped bacteria," *Materials Letters*, vol. 62, pp. 2999-3002, 2008.
- [106] R. Mogul, J. J. G. Kelly, M. L. Cable, and A. F. Hebard, "Synthesis and magnetic characterization of microstructures prepared from microbial templates of differing morphology," *Materials Letters*, vol. 60, pp. 19-22, 2005.
- [107] B. Zhang, S. A. Davis, N. H. Mendelson, and S. Mann, "Bacterial templating of zeolite fibres with hierarchial structure," *Chem. Commun.*, pp. 781-782, 2000.
- [108] M. T. Kumara, B. C. Tripp, and S. Muralidharan, "Exciton Energy Transfer in Self-Assembled Quantum Dots on Bioengineered Bacterial Flagella Nanotubes," *J. Phys. Chem.*, vol. 111, pp. 5276-5280, 2007.
- [109] M. Lunder, T. Bratkovič, S. Kreft, and B. Štrukelj, "Peptide inhibitor of pancreatic lipase selected by phage display using different elution strategies," *Journal of Lipid Research*, vol. 46, pp. 1512-1516, July 1, 2005 2005.
- [110] M. Lunder, T. Bratkovič, B. Doljak, S. Kreft, U. Urleb, B. Štrukelj, and N. Plazar, "Comparison of bacterial and phage display peptide libraries in search of target-binding motif," *Applied Biochemistry and Biotechnology*, vol. 127, pp. 125-131, 2005/11/01 2005.
- [111] T. Bratkovič, M. Lunder, T. Popovič, S. Kreft, B. Turk, B. Štrukelj, and U. Urleb, "Affinity selection to papain yields potent peptide inhibitors of cathepsins L, B, H, and K," *Biochemical and Biophysical Research Communications*, vol. 332, pp. 897-903, 2005.
- [112] W. M. Gommans, H. J. Haisma, and M. G. Rots, "Engineering Zinc Finger Protein Transcription Factors: The Therapeutic Relevance of Switching

Endogenous Gene Expression On or Off at Command," *Journal of Molecular Biology*, vol. 354, pp. 507-519, 2005.

- [113] D. R. Burton, C. F. Barbas, M. A. Persson, S. Koenig, R. M. Chanock, and R. A. Lerner, "A large array of human monoclonal antibodies to type 1 human immunodeficiency virus from combinatorial libraries of asymptomatic seropositive individuals," *Proceedings of the National Academy of Sciences*, vol. 88, pp. 10134-10137, November 15, 1991 1991.
- [114] D. Burton, J. Pyati, R. Koduri, S. Sharp, G. Thornton, P. Parren, L. Sawyer, R. Hendry, N. Dunlop, P. Nara, and a. et, "Efficient neutralization of primary isolates of HIV-1 by a recombinant human monoclonal antibody," *Science*, vol. 266, pp. 1024-1027, November 11, 1994 1994.
- [115] C. F. Barbas, E. Björling, F. Chiodi, N. Dunlop, D. Cababa, T. M. Jones, S. L. Zebedee, M. A. Persson, P. L. Nara, and E. Norrby, "Recombinant human Fab fragments neutralize human type 1 immunodeficiency virus in vitro," *Proceedings of the National Academy of Sciences*, vol. 89, pp. 9339-9343, October 1, 1992 1992.
- [116] S.-W. Lee, C. Mao, C. E. Flynn, and A. M. Belcher, "Ordering of Quantum Dots Using Genetically Engineered Viruses," *Science*, vol. 296, pp. 892-895, May 3, 2002 2002.
- [117] S. R. Whaley, D. S. English, E. L. Hu, P. F. Barbara, and A. M. Belcher, "Selection of peptides with semiconductor binding specificity for directed nanocrystal assembly," *Nature*, vol. 405, pp. 665-668, 2000.
- [118] R. R. Naik, S. J. Stringer, G. Agarwal, S. E. Jones, and M. O. Stone, "Biomimetic synthesis and patterning of silver nanoparticles," *Nat Mater*, vol. 1, pp. 169-172, 2002.
- [119] K.-I. Sano and K. Shiba, "A Hexapeptide Motif that Electrostatically Binds to the Surface of Titanium," *Journal of the American Chemical Society*, vol. 125, pp. 14234-14235, 2003/11/01 2003.
- [120] M. Sarikaya, C. Tamerler, A. K. Y. Jen, K. Schulten, and F. Baneyx, "Molecular biomimetics: nanotechnology through biology," *Nat Mater*, vol. 2, pp. 577-585, 2003.
- [121] J. W. Jaworski, D. Raorane, J. H. Huh, A. Majundar, and S. W. Lee, "Evolutionary Screening of Biomimetic Coatings for Selective Detection of Explosives," *Langmuir*, vol. 24, pp. 4938-4943, January 11, 2008 2008.

- [122] D. J. Evans, "The bionanoscience of plant viruses: templates and synthons for new materials," *Journal of Materials Chemistry*, vol. 18, pp. 3746-3754, 2008.
- [123] Y. Huang, C.-Y. Chiang, S. J. Lee, Y. Gao, E. L. Hu, J. D. Yoreo, and A. M. Belcher, "Programmable Assembly of Nanoarchitectures Using Genetically Engineered Viruses," *NANO Letters*, vol. 5, pp. 1429-1434, 2005.
- [124] S.-W. Lee, C. Mao, C. E. Flynn, and A. M. Belcher, "Ordering of Quantum Dots Using Genetically Engineered Viruses," *Science Magazine*, vol. 296, May 3 2002.
- [125] C. Mao, D. J. Solis, B. D. Reiss, S. T. Kottmann, R. Y. Sweeney, A. Hayhurst, G. Georgiou, B. Iverson, and A. M. Belcher, "Virus-based Toolkit for the Direct Synthesis of Magnetic and Semiconducting Nanowires " *Science*, vol. 303, p. 213, 2004.
- [126] M. T. Klem, D. Willits, M. Young, and T. Douglas, "2-D Array Formation of Genetically Engineered Viral Cages on Au Surfaces and Imaging by Atomic Force Microscopy," *J. Am. Chem. Soc.*, vol. 125, pp. 10806-10807, 2003.
- [127] J. C. Smith, K.-B. Lee, Q. Wang, M. G. Finn, J. E. Johnson, M. Mrksich, and C. A. Mirkin, "Nanopatterning the Chemospecific Immobilization of Cowpea Mosaic Virus Capsid," *NANO Letters*, vol. 3, pp. 883-886, 2003.
- [128] B. D. Gates, Q. Xu, M. Stewart, D. Ryan, C. G. Wilson, and G. Whitesides, "New approaches to nanofabrication: molding, printing, and other techniques," *Chemical Reviews*, vol. 105, pp. 1171-1196, 2005.
- [129] C. L. Cheung, J. A. Camarero, B. W. Woods, T. Lin, J. E. Johnson, and J. J. D. Yoreo, "Fabrication of Assembled Virus Nanostructures on Templates of Chemoselective Linkers Formed by Scanning Probe Nanolithography," *Journal of the American Chemical Society*, vol. 125, pp. 6848-6849, 2003.
- [130] R. D. Piner, J. Zhu, F. Xu, S. Hong, and C. A. Mirkin, "'Dip-Pen" Nanolithography," *Science Magazine*, vol. 283, pp. 661-663, 1999.
- [131] K. Kobayashi, N. Tonegawa, S. Fujii, J. Hikida, H. Nozoye, K. Tsutsui, Y. Wada, M. Chikira, and M.-a. Haga, "Fabrication of DNA Nanowires by Orthogonal Self-Assembly and DNA Intercalation on a Au Patterned Si/SiO₂ Surface," *Langmuir*, vol. 24, pp. 13203-13211, 2008.
- [132] P. W. K. Rothemund, "Folding DNA to create nanoscale shapes and patterns," *Nature*, vol. 440, pp. 297-302, 2006.

- [133] S. Balci, D. M. Leinberger, M. Knez, A. M. Bittner, F. Boes, A. Kadri, C. Wege, H. Jeske, and K. Kern, "Printing and Aligning Mesoscale Patterns of Tobacco Mosaic Virus on Surfaces," *Advanced Materials*, vol. 20, pp. 2195-2200, 2008.
- [134] A. Bernard, J. P. Renault, B. Michel, H. R. Bosshard, and E. Delamarche, "Microcontact Printing of Proteins," *Advanced Materials*, vol. 12, pp. 1067-1070, 2000.
- [135] Y. Cui, M. T. Bjirk, J. A. Liddle, C. Snnichsen, B. Boussert, and A. P. Alivisatos, "Integration of Colloidal Nanocrystals into Lithographically Patterned Devices," *NANO Letters*, vol. 4, pp. 1093-1098, 2004.
- [136] G. Sharma, V. Kripesh, M. C. Kim, and C. H. Sow, "Synthesis and characterization of patterned and nonpatterned copper and nickel nanowire arrays on silicon substrate," *Sensors and Actuators A*, vol. A139, pp. 272-280, 2007.
- [137] J.-H. Cho, S.-M. Han, E.-H. Paek, I.-H. Cho, and S.-H. Paek, "Plastic ELISA-on-a-Chip Based on Sequential Cross-Flow Chromatography," *Analytical Chemistry*, vol. 78, pp. 793-800, 2006/02/01 2006.
- [138] J.-W. Jeon, S.-M. Seo, H.-S. Kim, J.-S. Oh, Y.-K. Oh, G.-W. Ha, S.-Y. Hwang, and S.-H. Paek, "ELISA-on-a-chip for on-site, rapid determination of anti-rabies virus antibodies in canine serum," *Sensors and Actuators B: Chemical*, vol. 171-172, pp. 278-286, 2012.
- [139] A. Rasooly, H. Bruck, and Y. Kostov, "An ELISA Lab-on-a-Chip (ELISA-LOC)," in *Microfluidic Diagnostics*. vol. 949, G. Jenkins and C. D. Mansfield, Eds., ed: Humana Press, 2013, pp. 451-471.
- [140] R. Grover, "Indium Phosphide Based Optical Micro-Ring Resonator," PhD, Electrical and Computer Engineering, University of Maryland, College Park.
- [141] M. W. Pruessner, M. Datta, K. Amarnath, S. Kanakaraju, and R. Ghodssi, "Indium Phosphide Based MEMS End-Coupled Optical Waveguide Switches," in *17th International Indium Phosphide and Related Materials Conference*, Glasgow, Scotland, 2005.
- [142] P. K. Tien, "Light Waves in Thin Films and Integrated Optics," *Applied Optics*, vol. 10, pp. 2395-2413, 1971.
- [143] C. C. Davis, *Lasers and Electro-Optics Fundamentals and Engineering*. Cambridge: Cambridge University Press, 1996.
- [144] T. H. P. Chang, "Proximity effect in electron beam lithography," *Journal of Vacuum Science and Technology*, vol. 12, pp. 1271-1275, 1975.

- [145] C. Constancias, S. Landis, S. Manakli, L. Martin, L. Pain, and D. Rio, "Electron Beam Lithography," in *Lithography*, ed: John Wiley & Sons, Inc., 2013, pp. 101-182.
- [146] C. Vieu, F. Carcenac, A. Pépin, Y. Chen, M. Mejias, A. Lebib, L. Manin-Ferlazzo, L. Couraud, and H. Launois, "Electron beam lithography: resolution limits and applications," *Applied Surface Science*, vol. 164, pp. 111-117, 2000.
- [147] Shu-Fen Hu, Kuo-Dong Huang, Yue-Min Wan, and C.-L. Sung, "Proximity effect of electron beam lithography on single-electron transistors," *indian Academy of Sciences*, vol. 67, pp. 57-65, 2006
- 2006.
- [148] K. W. Thomas, K. F. David, N. K. Michael, K. Enoch, K. Amit, W. James, and M. W. George, "Pattern transfer to silicon by microcontact printing and RIE," *Nanotechnology*, vol. 7, p. 447, 1996.
- [149] Y. C. Zhu, J. Karouta, E. J. Geluk, T. d. Vries, J. J. G. M. v. d. Tol, J. J. M. Binsma, and M. K. Smit, "ICP Etching of InP and its Applications in Photonic Circuits," in *Symposium IEEE/LEOS*, Enschede, 2003, pp. 81-84.
- [150] B. Docter, E. J. Geluk, M. J. H. Sander-Jochem, F. Karouta, and M. K. Smit, "Deep etching of DBR gratings in InP using Cl₂ based ICP processes," in *Symposium IEEE/LEOS*, Eindhoven, 2006, pp. 97-100.
- [151] M. Serry, A. Rubin, M. Ibrahim, and S. Sedky, "Silicon Germanium as a Novel Mask for Silicon Deep Reactive Ion Etching," *Microelectromechanical Systems, Journal of*, vol. 22, pp. 1081-1088, 2013.
- [152] K. Namba, R. K. Pattanayek, and G. R. Stubbs, "Visualization of protein-nucleic acid interactions in a virus: refinement of intact tobacco mosaic virus at 2.9 Å resolution by X-ray fiber diffraction.," *Journal of Molecular Biology*, pp. 307-325, 1989.
- [153] R. K. Pattanayek and G. R. Stubbs, "Structure of the U2 strain of tobacco mosaic virus refined at 3.5 Å resolution using X-ray fiber diffraction," *Journal of Molecular Biology*, pp. 516-528, 1992.
- [154] H. Wang, J. N. Culver, and G. R. Stubbs, "Structure of ribgrass mosaic virus at 2.9 Å resolution. Evolution and taxonomy of tobamoviruses," *Journal of Molecular Biology*, pp. 269-279, 1997.
- [155] H. Wang and G. R. Stubbs, "The structure of cucumber green mottle mosaic virus at 3.4 Å resolution by x-ray fiber diffraction: significance for the evolution of tobamoviruses," *Journal of Molecular Biology*, pp. 371-384, 1994.

- [156] A. Durham, J. Finch, and A. Klug, "States of aggregation of Tobacco mosaic virus," *Nature*, vol. 229, pp. 37-42, 1971.
- [157] J. N. Culver, W. O. Dawson, K. Plonk, and G. STubbs, "Site-directed mutagenesis confirms the involvement of carboxylate groups in the disassembly of tobacco mosaic virus " *Virology*, vol. 206, pp. 724-730, 1995.
- [158] W. O. Dawson, D. L. Beck, D. A. Knorr, and G. L. Grantham, "cDNA cloning of the complete genome of tobacco mosaic virus and production of infectious transcripts " *Proceedings of the National Academy of Science (PNAS)*, vol. 83, pp. 1832-1836, 1986.
- [159] J. N. Culver, "Tobacco mosaic virus assembly and disassembly: determinants in pathogenicity and resistance," *Ann. Rev. Phytopathol.*, vol. 40, pp. 287-308, 2002.
- [160] M. Knes, A. Kadri, C. Wege, U. Gosele, H. Jeske, and K. Nielsch, "Atomic layer deposition on biological macromolecules: metal oxide coating of tobacco mosaic virus and ferritin," *NANO Letters*, vol. 61, pp. 1172-1177, 2006.
- [161] M. Knez, A. M. Bittner, F. Boes, C. Wege, H. Jeske, E. Maib, and K. Kern, "Biotemplated synthesis of 3-nm nickel and cobalt nanowires," *NANO Letters*, vol. 3, pp. 1079-1082, 2003.
- [162] M. Knez, M. Sumser, A. M. Bittner, C. Wege, H. Jeske, S. Kooi, M. Burghard, and K. Kern, "Electrochemical modification of individual nano-objects," *Journal of Electroanalytical Chemistry*, vol. 522, pp. 70-74, 2002.
- [163] M. Knez, M. Sumser, A. M. Bittner, C. Wege, H. Weske, T. P. Martin, and K. Kern, "Spatially Selective Nucleation of Metal Clusters on the Tobacco Mosaic Virus," *Advanced Functional Materials*, vol. 14, p. 116, 2004.
- [164] W. L. Liou, A. A. Balandin, D. M. Mathews, and J. A. Dodds, "Assembly and characterization of hybrid virus-inorganic nanotubes," *Applied Physics Letters*, vol. 86, p. 253108, 2005.
- [165] T. H. Turpen, S. J. Reinl, Y. Charoenvit, S. L. Hoffman, V. Fallarme, and L. K. Grill, "Malarial epitopes expressed on the surface of recombinant tobacco mosaic virus," *Biotechnology (N Y)*, vol. 13, pp. 53-7, Jan 1995.
- [166] X. Z. Fan, E. Pomerantseva, M. Gnerlich, A. Brown, K. Gerasopoulos, M. McCarthy, J. Culver, and R. Ghodssi, "Tobacco mosaic virus: A biological building block for micro/nano/bio systems," *Journal of Vacuum Science & Technology A*, vol. 31, pp. -, 2013.

- [167] M. Knez, M. Sumser, A. M. Bittner, C. Wege, H. Jeske, T. P. Martin, and K. Kern, "Spatially Selective Nucleation of Metal Clusters on the Tobacco Mosaic Virus," *Advanced Functional Materials*, vol. 14, pp. 116-124, 2004.
- [168] M. Zaitlin and H. W. Israel, "Tobacco mosaic virus " *C.M.I./A.A.B.*, vol. 151, 1975 1975.
- [169] K. Gerasopoulos, M. McCarthy, P. Banerjee, X. Fan, J. N. Culver, and R. Ghodssi, "Biofabrication methods for the patterned assembly and synthesis of viral nanotemplates," *Nanotechnology*, vol. 21, p. 055304, 2010.
- [170] X. Chen, K. Gerasopoulos, J. Guo, A. Brown, C. Wang, R. Ghodssi, and J. N. Culver, "A Patterned 3D Silicon Anode Fabricated by Electrodeposition on a Virus-Structured Current Collector," *Advanced Functional Materials*, vol. 21, pp. 380-387, 2011.
- [171] K. Gerasopoulos, E. Pomerantseva, M. McCarthy, A. Brown, C. Wang, J. N. Culver, and R. Ghodssi, "Hierarchical Three-Dimensional Microbattery Electrodes Combining Bottom-Up Self-Assembly and Top-Down Micromachining," *ACS Nano*, vol. 6, pp. 6422-6432, 2012.
- [172] Z. Lin and m. D. Ward, "The role of longitudinal waves in quartz crystal microbalance applications in liquids," *Analytical Chemistry*, vol. 67, pp. 685-693, 1995.